THE UNIVERSITY OF WARWICK

Molecular Organisation and Assembly in Cells
(MOAC)

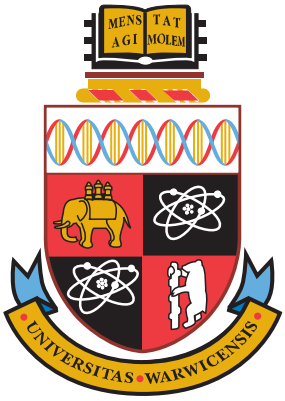

Quantification of the Plant Endoplasmic Reticulum

PhD. Thesis

Abdnacer Bouchekhima

September 7, 2009

THE UNIVERSITY OF WARWICK

Molecular Organisation and Assembly in Cells
(MOAC)

Centre for Scientific Computing(CSC)
Mathematics Institute
Department of Biological Sciences

Quantification of the Plant Endoplasmic Reticulum

by

Abdnacer Bouchekhima

Supervisors

Dr. Lorenzo Frigerio	Department of Biology
Dr. Markus Kirkilionis	Mathematics Institute

This thesis is submitted in partial fulfilment of the requirements for the degree of
Doctor of Philosophy in Scientific Computing

September 7, 2009

To Linda, Adam and Hana.

Abstract

One of the challenges of quantitative approaches to biological sciences is the lack of understanding of the interplay between form and function. Each cell is full of complex-shaped objects, which moreover change their form over time. To address this issue, we exploit recent advances in confocal microscopy, by using data collected from a series of optical sections taken at short regular intervals along the optical axis to reconstruct the Endoplasmic Reticulum (ER) in 3D, obtain its skeleton, then associate to each of its edges key geometric and dynamic characteristics obtained from the original filled in ER specimen. These properties include the total length, surface area, and volume of the ER specimen, as well as the length surface area, and volume of each of its branches. In a view to benefit from the well established graph theory algorithms, we abstract the obtained skeleton by a mathematical entity that is a graph. We achieve this by replacing the inner points in each edge in the skeleton by the line segment connecting its end points. We then attach to this graph the ER geometric properties as weights, allowing therefore a more precise quantitative characterisation, by thinning the filled in ER to its essential features. The graph plays a major role in this study and is the final and most abstract quantification of the ER. One of its advantages is that it serves as a geometric invariant, both in static and dynamic samples. Moreover, graph theoretic features, such as the number of vertices and their degrees, and the number of edges and their lengths are robust against different kinds of small perturbations. We propose a methodology to associate parameters such as surface areas and volumes to its individual edges and monitor their variations with time. One of the main contributions of this thesis is the use of the skeleton of the ER to analyse the trajectories of moving junctions using confocal digital videos. We report that the ER could be modeled by a network of connected cylinders ($0.87\mu m \pm 0.36$ in diameter) with a majority of 3-way junctions. The average length, surface area and volume of an ER branch are found to be $2.78 \pm 2.04\mu m$, $7.53 \pm 5.59\mu m^2$ and $1.81 \pm 1.86\mu m^3$ respectively. Using the analysis of variance technique we found that there are no significant differences in four different locations across the cell at 0.05 significance level. The apparent movement of the junctions in the plant ER consists of different types, namely: (a) the extension and shrinkage of tubules, and (b) the closing and opening of loops. The average velocity of a junction is found to be $0.25\mu m/sec \pm 0.23$ and lies in the range 0 to $1.7\mu m/sec$ which matches the reported actin filament range.

Acknowledgments

I would like to thank the EPSRC, MOAC and Prof. Alison Rodger for providing me with the necessary financial support, without which this work could not have been achieved. Many thanks to my parents who brought me to life and have always encouraged me to aim higher. Lots of thanks to my beloved wife Linda who gave the necessary moral support to finish this work. Special thanks to Dr. Erwin George who proof read the text and made very constructive suggestions during my writing up. Many thanks to my supervisors.

Contents

List of Figures

List of Tables

List of Algorithms

Nomenclature

α The aperture angle of a microscope objective; the angle under which light enters into the front lens of the objective, page 36

PH Pinhole; diaphragm of variable size arranged in the beam path to achieve optical sections, page 41

Ti Tumor inducing, page 22

4SED FOUR-point Sequential Euclidean Distance mapping, page 74

8SED EIGHT-point Sequential Euclidean Distance mapping, page 74

Airy disc The Airy disc refers to the inner, light circle (surrounded by alternating dark and light diffraction rings) of the diffraction pattern of a point light source. The diffraction discs of two adjacent object points overlap some or completely, thus limiting the spatial resolution capacity., page 38

Biosynthetic The biosynthetic route in the secretory pathway starts from the ER and ends at the plasma membrane, page 16

CER cortical ER, page 10

CLSM Confocal laser scanning microscopy, page 32

CM Confocal microscopy, page 31

Endocytosis The Endocytosis route in the secretory pathway starts from the plasma membrane to the trans-Golgi network (early endosome) followed by the Golgi or the pre-vacuolar compartment (late endosome) and lytic vacuole, page 16

ER The endoplasmic reticulum, page 7

FWHM Full width at half maximum of an intensity distribution, page 40

GFP Green fluorescent protein, page 8

G A graph: a set pair of a finite set of vertices and a finite set of edges, page 104

NA Numerical aperture of a microscope objective, page 36

NER The Nuclear ER, page 9

n refractive index of an immersion liquid, page 36

PER The peripheral ER, page 10

PMT Photomultiplier tube (detector used in CLSM): a light detector that multiplies the signal, produced by the incident light, by large factors (as much as 100 million times) to enable weak signal, generated by limited flux of light, to be detected., page 34

PM The plasma membrane, page 15

PSF The intensity point spread function: a function which maps the intensity distribution of a point light source into the image space, page 39

PVC The pre-vacuolar compartment, page 16

QC Quality control, page 18

resel resolved element, page 46

SED Sequential Euclidean Distance mapping, page 74

SP The secretory pathway, page 15

Voxel a volume element, page 46

V The set of vertices in a graph, page 104

SNR Signal to Noise Ratio: the ratio of signals detected in the specimen and the unwanted signals that are caused randomly by various optic and electronic components, which are also recorded by the detector., page 31

Part I

Background

1

Thesis road map

This thesis presents a collection of computational tools to help scientists study the form and movement of the endoplasmic reticulum, and other network-like structures, whose data were acquired and digitised by imaging equipment, such as a widefield or confocal microscope, and stored as digital images. The methods proposed are based on the representation of the network by its medial axis, or skeleton, which is then abstracted by a graph, that is a simple mathematical object, to simplify the analysis by exploiting well established graph theory algorithms.

The general workflow involves five main steps: (a) sample preparation and data acquisition (b) data pre-processing and noise removal (c) skeleton extraction (d)

motion analysis, and (e) data abstraction.

The overall text is organised into three major sections (see Table 1.1): Preliminaries, Main tasks, and Supplementary material. The Preliminaries section includes the title page, the abstract, the lists of figures, tables, programs, and algorithms, followed by the Nomenclature, and the Contents page.

The main tasks section consists of four parts: Background (Part I), Methodology (Part II), Results (Part III), and Conclusion (Part IV).

In addition to this introductory guide, Part I includes Chapter 2 Motivations: which reviews the ER characteristics and highlights its main features, as well as the role it plays in the cell in general and in the secretory pathway in particular, with a focus on its geometric and dynamic characteristics, as reported in the literature, together with a brief description of the contemporary techniques utilised in its study.

Part II is a walk through of the steps followed to achieve the overall aim of this study. It thoroughly explains the procedure for collecting data (Chapter 3); the techniques used to remove noise and extract the skeletons and assign geometric parameters to their edges and vertices (Chapter 4); the approach adopted to analyse the movement of the ER (Chapter 5); and finally a brief review about Graph theory (Chapter 6). Each of these chapters includes a *state-of-the-art* section which reviews the corresponding existing techniques.

Part III is dedicated to Results and Discussion. It summarises the most important findings of this study and consists of two chapters: Chapter 7: The Static ER, and Chapter 8: The Dynamic ER. Chapter 7 deals with the geometry of immobilised ER samples marked with a fluorescent protein and acquired by a confocal microscope. This chapter examines four geometric properties: the average length, the average surface area, and the average volume of a branch; as well as the average degree per junction. Chapter 8 extends the investigation further to include more realistic

ER samples by excluding immobilising agents from the above sample preparation protocol. This chapter adds to the four parameters introduced in the previous chapter, the average speed of a junction, the average moments of displacements of orders *zero* and *two* as well as the average maximum displacement per junction.

Part IV is the final part of this section. It concludes the work, highlights the main lessons learnt, and includes a view for future directions.

The last section consists of an appendix, a bibliography, and an index. The appendix includes all the codes developed throughout this study and consists of: Appendix A.1: C++ codes, Appendix A.3: Matlab files, Appendix A.4: TcL scripts, and Appendix A.5: Bash scripts.

Table 1.1: An overview of the thesis

Section	Parts	Chapters
Preliminaries	Title page, abstract, lists of figures, tables, programs and algorithms, nomenclature, and contents	
Main tasks	Part I: **Background**	Chapter 1: Thesis map Chapter 2: Motivations
	Part II: **Methodology**	Chapter 3: Data Acquisition Chapter 4: Skeleton Extraction Chapter 5: Motion Analysis Chapter 6: Data Abstraction
	Part III: **Results**	Chapter 7: The Static ER Chapter 8: The Dynamic ER
	Part IV: **Conclusion**	Chapter 9: Conclusion and Suggestions for Future work
End matter	Part V: **Appendix**	Appendix A.1: C++ codes Appendix A.3: Matlab files Appendix A.4: TcL scripts Appendix A.5: Bash scripts

2

Motivations

Eukaryotic cells contain sophisticated membrane-bound compartments that vary in shape and size. While the nucleus, lysosomes, and peroxisomes have almost spherical shapes; the endoplasmic reticulum (ER), Golgi apparatus, and mitochondria take the form of complex networks of sheets and tubules. Many of these organelles can be encountered in cells of different species in the same forms (see Staehelin & Kang (2008)). Among the largest and most complex of these organelles is the ER, which not only looks similar in different cell types; but, interestingly and intriguingly, also contains tubules and sheets with almost identical dimensions across cell types. Shape and size are therefore believed to play a major role in the function of the

ER (see Voeltz & Prinz (2007)). This chapter exposes the most prominent features of the ER, focussing on its shape and size. It summarises the ER's well known characteristics, and briefly describes the contemporary techniques commonly used in its study.

2.1 Introduction

The ER was initially described by Emilio Veratti (1902) in limb muscle of the water beetle *Hidrophilus liceus* and muscle fibre from the fish *Cyprinus carpio*. Porter *et al.* (1945) later found the same *lace-like* structure in tissue culture cells by means of electron microscopy and consequently gave it the name of endoplasmic reticulum because of its network-like structure. A few years later, when comparing a variety of cells in different species including avian fibroblasts, and macrophages; rabbit mesothelia, endothelia, and nephron epithelia; and rat glandular epithelia (parotid) Palade & Porter (1954) found that **the ER exists in all of these cell types**. Ever since, the ER has become the focus of intense biochemical investigations to determine its role in living organisms.

The discovery of the green fluorescent protein (GFP), from the jellyfish Aequorea victoria, **with which almost any protein can be tagged while retaining its function and dynamic properties** (see Tsien (1998)), has revolutionised cell research. Both the ER's lumen and membrane have been visualised using GFP. The former has been successfully visualised using soluble GFP fused to an N-terminal signal peptide and an ER retention signal (HDEL[1]) (see Boevink *et al.* (1999, 1996) and Boevink *et al.* (1998)); while the latter has been highlighted with a fusion between Calnexin, a 67 kD type-I membrane protein, and GFP (see Irons *et al.* (2003); Kurup *et al.* (2005) and Runions *et al.* (2006)).

Combining GFP, and modern computer graphics algorithms, applied to data ac-

[1]HDEL refers to: Histidine, Aspartic Acid, Alutamic Acid, Leucine

quired by high resolution microscopes, has empowered cell research through improved cell visualisation. Not only has it become possible to obtain detailed micro scale 3D reconstructions of the ER; but it has also become possible to visualise the ER, and other compartments, from almost any arbitrary angle.

Depending on the resolution of the imaging equipment used, different subdomains of the ER can be differentiated.

2.2 The ER visualised by confocal microscopy

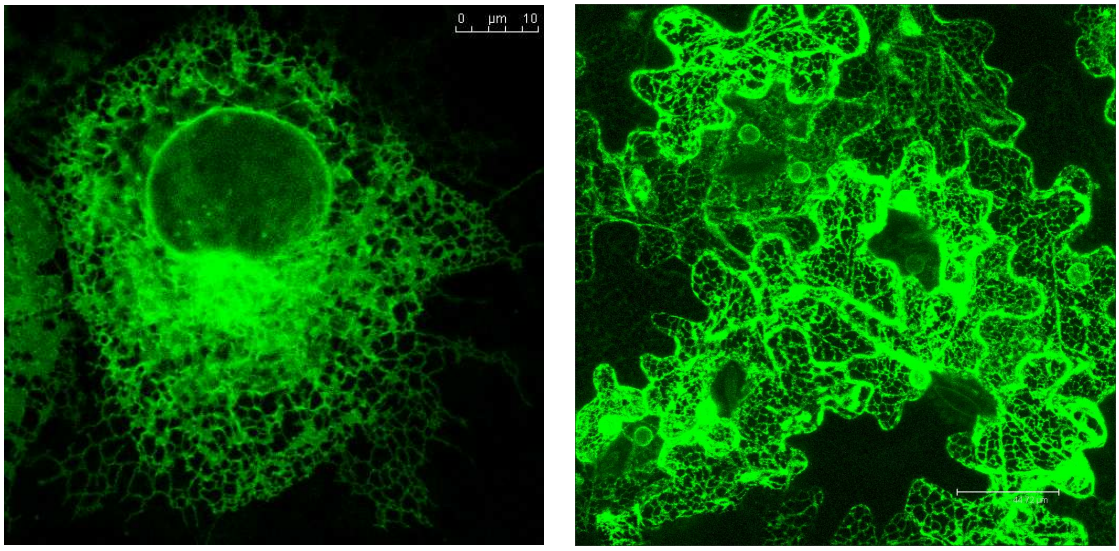

(a) Mammalian ER visualised by confocal microscopy. Cytosolic ER takes a tubular connected network structure. Dimmer parts lie in out-of focus planes. Scale bar 10.00 μm

(b) Plant ER visualised by confocal microscopy. The ER occupies a thin cortical region in plant cells. Regions that are in the focus plane are clearer than other regions. Scale bar 44.72 μm

Figure 2.1: The ER visualised by confocal microscopy.

When visualised by confocal microscopy the ER looks like a 3D interconnected network of endomembranes that is organised in a complex system of tubules and cisternae. At this level of magnification, i.e. up to 200 nm lateral resolution, the ER is usually classified into either nuclear or peripheral according to whether it is in contact with the nucleus (see Voeltz *et al.* (2002)). The nuclear ER (NER) is the

part of the ER that extends from the nucleus and contains a lumen surrounded by two sheets of membranes which are joined via the nuclear pores. The peripheral ER (PER), sometimes called cortical ER (CER), is the rest of the organelle and takes the form of a complex network that spreads out to the plasma membrane (Voeltz *et al.*, 2002), to distribute proteins to different compartments in the cell, and enable communication with neighbouring cells via the plasmodesmata (Staehelin, 1997).

A region of interest (ROI) of the lower epidermis of an agroinfiltrated tobacco leaf is shown in Figure 2.1(b) on page 9. GFP fused to an N-terminal signal peptide for entry into the ER and to a C-terminal ER retention signal that mediates retrieval from the Golgi apparatus to the ER (Anelli & Sitia, 2007), when the protein escapes in the transport vesicles via bulk flow. The recombinant protein accumulates and highlights the ER which looks like a network that fills most of the cell volume.

It is important to recognise that in confocal microscopy only the regions that are in the plane of focus will show the signal; so in order to obtain a 2D clear image of the ER it is sometimes necessary to scroll through the sample to find regions that completely lie in the plane of focus. This is what explains the presence of brighter regions compared to other regions in Figure 2.1(a) on page 9.

A confocal microscope is equipped with a detector (photomultiplier tube) or camera, which allows the recording of time series, that is indispensable for the study of the movement of the ER. The ER contains regions that appear to be fixed and relatively immobile as well as highly mobile regions that constantly remodel and appear to contain a dynamic flux of material. Fluorescence originates from soluble protein present in the lumen of the ER; so any apparent movement occurs through bulk ER remodeling.

Finally it is important to note that structures under the confocal microscope appear larger, because of the wavelength of visible light. The next section explains how the ER appears under an electron microscope.

2.3 The ER visualised by electron microscopy

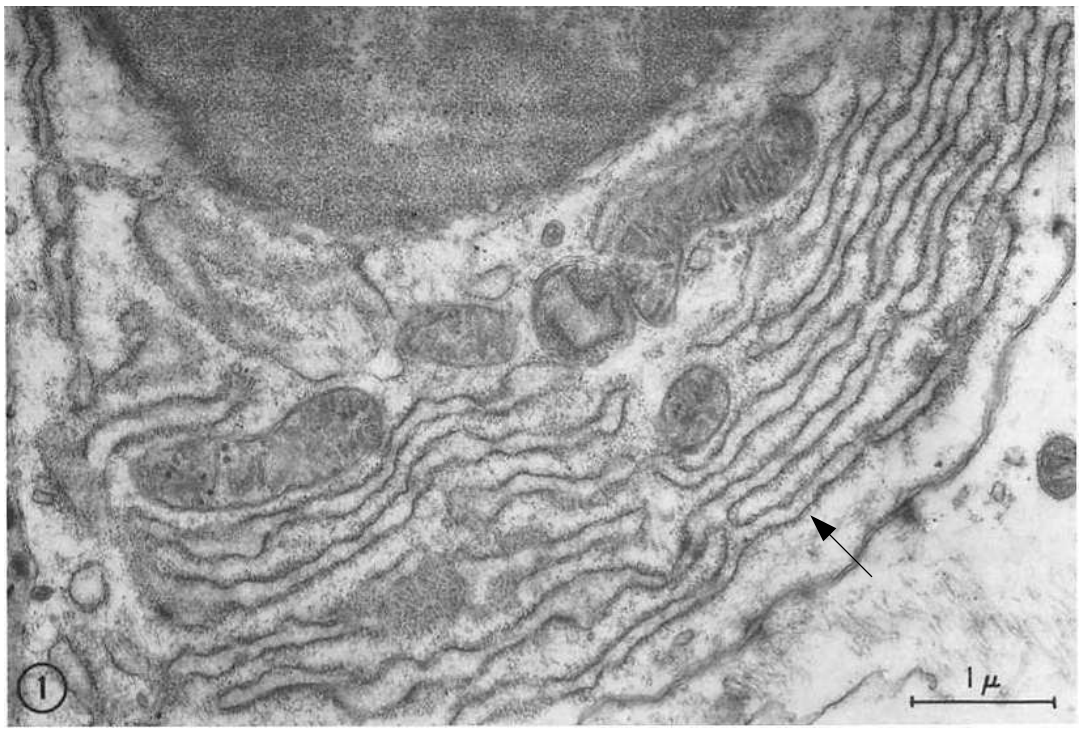

Figure 2.2: The ER of notochord cells of *Triturus alpestris*. The ER extends in nearly parallel sheets. X 18,500, picture taken from Selman & Jurand (1964). It is hard to see the tubular structure in the image. Scale bar 1 μm.

When observed by transmission microscopy, i.e. up to $5nm$ resolution, the ER reveals two distinct types: a rough type that is studded with ribosomes and known as Rough ER (RER); and a smooth type that is ribosomes free and known as smooth ER (SER). In mammals **RER corresponds to the sheets and the SER to tubules** (see Shibata *et al.* (2006)). In plants, SER is usually found in quantity in specialised cells.

The tubular network, observed using confocal microscopy, is virtually invisible under an electron microscope. It is difficult to see the network because it is not planar, and for EM very thin sections that might only include a few tubules in their entirety are imaged.

Figure 2.2 on page 11 illustrates what we can see using the EM and how difficult it is to see proteins in the lumen of the ER. It is possible to see a few regular arrays

of ribosomes which indicate the presence of the RER. The lumen is not as electron opaque as the cytosol; so we cannot really see a specific membrane. What we see in EM is actually a section through a sheet which represents rough ER studded with ribosomes. Tubular ER which appears to be more abundant in the cell and which fills most of the field of vision is harder to capture using EM. Finally, EM is much more time consuming and reveals much less than a confocal microscope but has the advantage of allowing smaller structures to be visualised.

Based on "ultrarapid freezing techniques", Staehelin (1997), controversially, reports that **the ER may be composed of more than sixteen discrete functional domains**, each of which always contains the same family of proteins. However, it is important to note the connectivity of the ER; Voeltz *et al.* (2002) and Puhka *et al.* (2007), report that when injected into the cell in an oil droplet, fluorescent dyes that cannot exchange between discontinuous membranes, diffuse throughout the ER; and the repeated bleaching of a region of the ER, whose lumen (or membrane) was targeted by a GFP-tagged protein, results in complete loss of fluorescence. These observations serve as evidence that **the ER is a single connected compartment**.

In mammals, the ER occupies **more than** 70% **of the total area of the cell** (Fawcett, 1981) and **over** 10% **of its total volume** (Voeltz *et al.*, 2002) and so is regarded as **the largest single interconnected intracellular membrane system containing a common luminal space. In plants, cortical ER occupies a very thin, almost two dimensional, layer of cytoplasm beneath the plasma membrane, refer to Section 2.9 on page 20.**

On the grounds of its dynamics, and for the purposes of this thesis, the ER is subdivided into three essential parts, cytosolic, cortical, and nuclear ER. Cortical and nuclear ER are relatively immobile, whereas cytosolic ER is highly dynamic, which rapidly remodels itself in the form of tubular movements, where tubular structures appear or disappear in fractions of a second.

The exceptional morphologic and dynamic heterogeneities of the ER are believed to be linked to its functional diversity (Verkhratsky, 2007). The next section highlights the current understanding of how the ER gets its form.

2.4 How the ER gets its form

It is often easier to study the form of an object and relate it to its function rather than try to directly understand its function. Furthermore, not only do form, size, and other morphological properties differentiate and characterise living organisms, but they also reflect their optimal functions (Staehelin & Kang, 2008). How and why the ER gets its form has attracted the attention of many research groups.

To identify the proteins responsible for shaping the ER, Voeltz *et al.* (2006), started by showing that vesicles purified from *Xenopus laevis oocytes*, coalesce to form tubular networks. In the presence of GTP, they found that these networks could be stained with antibodies directed specifically against an ER marker.

They also found, using *maleimide biotin*, that sulphydryl reagents inhibited the formation of the network, and successfully identified *Rtn4a/NogoA*, a member of the reticulon family, as one of its targets. They then showed that the modification of *Rtn4a/NogoA*, by *maleimide biotin*, was correlated with the inhibition of the formation of the network; and that antibodies against *Rtn4a/NogoA* suppressed network formation *in vitro*. More importantly, when over-expressing *Rtn4a/NogoA*, they found that it enhanced tubule formation.

Voeltz *et al.* discovered that *DP1*, an integral membrane protein specific to the tubular ER, interacts with *Rtn4a/NogoA*, while its homologue, *YOP1*, interacts with *Rtn1* and *Rtn2*, which are *Saccharomyces cerevisiae* reticulons. Furthermore, when deleting either *YOP1*, *Rtn1* and *Rtn2*, or *YOP1* and *Rtn1* they obtained a abnormal tubular ER structure; which indicate that *YOP1* and *Rtn1* are what maintains the ER tubular structure.

Finally, when studying the topology of Rtn4 and *YOP1*, Voeltz *et al.* (2006) found that they both have larger hydrophobic regions (i.e transmembrane domains) than the average protein; between 30 and 35 residues instead of around 20 residues. This led to the conclusion that because of their conical topology, with their bases in the outer membrane surface, they maintain the ER tubular structure.

Rtn4a/NogoA belongs to the Reticulon family of ER resident proteins, which are restricted to the tubular ER. They collectively share a 200 amino acid region at their C-Terminal called "reticulon domain", and are commonly attached to the ER by their hydrophobic C-terminal (Oertle *et al.*, 2003). They occupy a larger area in the outer leaflet of a membrane than in the inner leaflet (see Voeltz & Prinz (2007); Voeltz *et al.* (2002) and Voeltz *et al.* (2006)).

In a later study, Voeltz & Prinz (2007) report four types of proteins responsible for the morphology of the ER: (a) the first type of protein stabilises the curvature of the ER membrane (b) the second type tethers the ER membrane to other cell compartments (c) the third type regulates fission and fusion of the ER membrane (d) and the fourth type shapes the ER by stabilising certain morphologies.

The first type of proteins might use three possible mechanisms to generate a high curvature in the ER membrane, according to Voeltz & Prinz (2007); either (a) a protein scaffold bends the membrane, the reticulon family discussed above, or (b) the two leaflets of the bi-layer tend to stay together forcing certain morphologies or (c) the distribution of the lipids in the bi-layer is non-symmetric.

The second type of protein works by attaching the membrane of the ER to the cytoskeleton, another membrane, or to both (Voeltz & Prinz, 2007). For example, the attachment of the ER to actin filaments, in plants, causes it to take a tubular network structure and when depolymerised, the ER loses this structure.

The third type of proteins includes proteins $p97$ and $VCIP135$ which are thought to help the ER regain its shape after mitosis. They are believed to be regulated by phosphorylation or a post-translational modification during the cell cycle.

Finally, maintaining different domains, with the same shapes, in the ER is thought to be governed by three mechanisms: (a) selective diffusion (b) membrane tethering and (c) the segregation of membrane-shaping proteins into certain parts of the organelle, see Voeltz & Prinz (2007, and references therein).

The ER touches almost all other cell compartments (Staehelin, 1997); because most of them require proteins that are initially translocated into the ER (Voeltz *et al.*, 2002); which explains the ER tubular network structure as an efficient means of distributing proteins to these compartments.

The size of the ER is important because the production of secretory proteins requires a large surface, hence the use of the ER membrane, which provides a larger surface than the plasma membrane (Vitale & Denecke, 1999). Understanding the form of the ER, therefore, provides valuable insight into its function. The next section summarises the importance of the ER in the secretory pathway.

2.5 The ER and the Secretory Pathway

An important point to raise here is that the ER is the entry point to the secretory pathway. It is the primary site of protein synthesis, maturation, and sorting, and plays a crucial role in protein folding, assembly and delivery of biologically active proteins to the proper target sites in the cell, its membranes and the extracellular space (see Nicchitta (2007); Schröder & Kaufman (2005b) and Sitia (2007)). These and other characteristics indicate the importance of understanding the function of this organelle.

To be transported from within the cell to the extracellular space, or backwards, biologically active proteins follow a well defined route known as the secretory pathway (SP). The forward route, known as biosynthesis route, starts with the ER, followed by the Golgi complex and the trans-Golgi network, before proteins reach the plasma membrane (PM) which surrounds the cell, and subsequently the extra

cellular space (Anelli & Sitia, 2007). The reverse route, known as endocytosis, starts from the plasma membrane to the trans-Golgi network (early endosome) followed by the Golgi or the pre-vacuolar compartment (late endosome) and lytic vacuole. Although it is known that secretion occurs from the Golgi apparatus to the plasma membrane through carriers (Hawes & Satiat-Jeunemaitre, 2005), it is not currently clear which of these carriers is responsible for this task (see Hanton *et al.* (2005) and Denecke (2007)). The Golgi, the trans-Golgi, and the pre-vacuolar compartment (PVC), form cross junctions in both the Endocytosis and the biosynthetic routes.

2.6 The role of the ER in protein folding

The ER plays a crucial role in protein folding. Proteins are composed of both hydrophobic and hydrophilic domains. The exposure of the former is undesirable since it causes the formation of toxic aggregates that may be harmful to the cell. To prevent this from happening, proteins shelter the hydrophobic regions from the aqueous environment. The process of **protein folding is usually accomplished by ER resident helper proteins called chaperones, which recognise, bind and thus mask the hydrophobic regions.**

In Eukaryotes, DNA is transcribed in the nucleus and mRNA transported through nuclear pores to the cytosol where it is translated by the ribosomes on the surface of the ER. This gives rise to a protein precursor which can then be targeted to other compartments in the cell (see Denecke (2007) and Cooper (2000)).

Targeting mRNA to the ER is understood to be achieved in different steps. It starts with the synthesis of mRNA in the nucleus; which is then transported to the cytosol; where it is translated by ribosomes. Ribosomes on the surface of the rough ER start synthesising the nascent polypeptide chain. Secretory proteins synthesised on the RER usually have a signal recognised by the Signal Recognition Particle

(SRP), which recognises signal peptides as they emerge on the ribosome surface before they are fully synthesised. This is assisted by the SRP-receptor [2], which guides the ribosome to the translocation pore, where translocation resumes. Proteins synthesised on the rough ER fold up with the help of a particular chaperone called the binding protein (BiP)[3]. BiP is also believed to close the translocation pores if not occupied by ribosomes.

In addition to soluble proteins, the ER is also the site of synthesis of both types of membrane spanning proteins, part of which lies in the lumen and the other lies in the cytosol. In the case of Type I membrane spanning proteins, whose N-terminal lies in the luminal side of the ER membrane, translocation occurs as follows. First a signal peptide (SiP) is recognised and bound to the SRP. The complex is then transported to a translocation pore and translation continues. The protein is pulled through, possibly with the help of a chaperone. The portion of the protein lying in the transmembrane domain has yet to be translated. Translation carries on, but the transmembrane portion does not translocate further but remains inserted in the membrane. The ribosome will finish translating the mRNA and the remainder of the protein is exposed in the cytosol. Once the ribosome is disengaged from the mRNA, Type I membrane spanning protein remains associated with the translocation pore and the nascent chain as a portion exposed in the lumen and a portion exposed in the cytosol. The transmembrane domain will diffuse laterally out of the translocation pore into the membrane and will act as a membrane anchor (Denecke, 2007).

Type II membrane spanning proteins, in which the C-terminal lies in the luminal side of the ER membrane, carry a transmembrane domain which acts as a signal for the entry into the ER. A large portion of the protein is synthesised in the cytosol before it is translocated into the ER. In some cases the transmembrane domain can be at the very C-terminus of the protein which means that the protein is fully

[2]SRP-receptor recognises the SRP

[3]BiP is a specialised protein which belongs to the heat shock 70 family, which has representatives in all compartments of the cell, where protein folding occurs, such as chloroplast, mitochondria, cytosol

synthesised before it can be translocated (Hanton *et al.*, 2005), as in prokaryotes. This process is most likely assisted by chaperones on either side of the membrane (see Cooper (2000); Denecke (2007); Fawcett (1981); Vitale & Denecke (1999) and daSilva *et al.* (2004)).

Once properly folded, proteins exit the ER to the next destination in the SP, the Golgi apparatus, for further processing. Properly folded and synthesised soluble proteins reach the Golgi apparatus, from the ER, via transport vesicles. These proteins first enter the transport vesicles. The transport vesicles then travel, in turn, to the Golgi apparatus, where they fuse with its membrane and release the proteins in its lumen for further processing. This transport of vesicles occurs in both directions, ie from the ER to the Golgi (anterograde) and from the Golgi apparatus to the ER (retrograde by vesicle in plant cells, see Hawes & Satiat-Jeunemaitre (2005) and Cooper (2000)).

These vesicles are recycled to avoid continuous growth of the end locations of the secretory pathway, which can be detrimental (Denecke, 2007). The fate of misfolded proteins is discussed in the next section.

2.7 The ER and quality control

It is not always guaranteed for proteins to fold up properly and reach their final, low energy, native conformation. This can be due to mutations or lack of partner proteins or cofactors. Their fate, in this case, is fundamentally different. Immature or misfolded proteins are retained inside the ER; they are unfolded for a second chance to properly fold; and if they fail to achieve this target, these aberrant proteins are targeted for final destruction or degradation. In addition to retaining immature or misfolded proteins, unfolding them or degrading them, the ER de-aggregates aggregated proteins. Protein folding is therefore closely related to the ER's quality control (QC), a tight system, which ensures that the tasks of protein folding, modification

and assembly are properly performed (Anelli & Sitia, 2007).

Combined with ER-associated folding (ERAF) and transport vesicles, ER-associated degradation (ERAD) plays a major role in the export efficiency of certain cargo proteins Anelli & Sitia (2007); Wiseman *et al.* (200). ERAD involves many steps, according to Anelli & Sitia (2007): (a) first, misfolded proteins and terminally misfolded proteins are discriminated by manose-trimming (b) They then, possibly, undergo partial unfolding and reduction, with the help of BiP and PDI, before retrotranslocation. (c) This is followed by dislocation, where Sec61, yeast Der1p and mammalian Derlin1, 2 and 3 are found to be involved (Anelli & Sitia, 2007), and (d) once they reach the cytosol they are ubiquitinated by E2-E3 complexes, then an N-glycanase removes the oligosaccharide moieties from glycoproteins, see Anelli & Sitia (2007).

2.8 The ER and Golgi bodies

An interesting characteristic of the plant ER is the movement of Golgi bodies on the ER network (Hanton *et al.*, 2005). The ER export sites and Golgi bodies move together as single secretory units (Hawes & Satiat-Jeunemaitre, 2005). ER export sites are specialised regions of the ER responsible for the formation of anterograde transport vesicles, which can be visualised using fluorescent protein fusions of GTPases or coat proteins that are responsible for COPII transport vesicles. It is important to note that transport by vesicle in plants might not occur because of the possibility that Golgi bodies are associated with the ER. Little is known about the sites where the ER accepts retrograde transport vesicles. The so called ER import sites have yet to be visualised using specific markers (Denecke, 2007).

2.9 The plant ER

Plant cells offer a very attractive model for the study of the ER due to its pleiomorphic nature (Staehelin, 1997), because in vegetative cells, whose volume is in large part occupied by the central vegetative vacuole, the ER is forced by turgour pressure against the plasma membrane and the cell wall. Therefore cortical ER occupies a very thin, almost two dimensional, layer of cytoplasm beneath the plasma membrane. This is ideal for the study of the ER architecture and dynamics using light microscopy. Once the realm of electron microscopy alone (Lichtscheidl & Hepler, 1996), the study of the plant ER has been recently revitalised by the use of fluorescent protein reporters, which allow the study of ER dynamics *in vivo*. The plant ER lumen has been successfully visualised using soluble GFP fused to an N-terminal signal peptide and an ER retention signal (HDEL) (see Boevink *et al.* (1999, 1996) and Boevink *et al.* (1998)). Likewise, a fusion between calnexin and GFP (see Irons *et al.* (2003); Kurup *et al.* (2005) and Runions *et al.* (2006)), has been used to highlight the plant ER membrane. The ER is highly dynamic and its constant remodelling depends on its attachment to underlying cytoskeletal structures. However, unlike the mammalian ER, the plant ER is not attached to microtubules but to actin filaments (Boevink *et al.*, 1998). It is therefore predicted that specific myosin isoforms mediate this interaction. Interestingly, when cells are treated with drugs like latrunculin that disrupt the cytoskeleton, ER movement is inhibited but its architecture remains intact (see Boevink *et al.* (1998); Dreier & Rapoport (2000) and Shibata *et al.* (2006)).

Drug inhibition studies have shown that whilst the streaming ER is dependent on actin, cortical network ER remodelling is dependent on the microtubules during the early stages of cell elongation. It has also been reported that oryzalin has an effect on ER dynamics in tobacco leaf epidermal cells, Arabidopsis roots and BY-2 cells but the effects were specific to the drug rather than microtubule depolymerisation

per se.(see Langhans *et al.* (2009)).

A shift to cisternal over tubular ER was proposed to occur due to an increased secretory load in differentiating maize root cap cells and during mobilisation of seed storage protein in germinating mung bean cotyledons (see Stephenson & Hawes (2005)).

2.10 Common Techniques to study the ER

As is the case for other organelles; studying the ER can be achieved through the delivery of exogenous gene or protein material into the cell. A foreign protein, such as GFP-tagged protein, has to be expressed by the host cell for subsequent observation and analysis. Different methods, involving transient expression/stable transformation, have been used to study the ER. These methods vary according to their speed and complexity. Among the most common of these are: electroporation, particle bombardment, and *Agrobacterium*-mediated transformation (see Hansen & Wright (1999); Taylor & Fauquet (2002) and Balbás (2004)).

2.10.1 *Agrobacterium*-mediated transformation

Leaf infiltration with *Agrobacterium* (see Figure 2.3 on page 22) is a relatively easy technique that stably integrates DNA into the cell. Epidermal cells from infiltrated leaves can be analysed a few days after infiltration. *Agrobacterium* mediates the transfer of DNA to the genome of the plant. Transfection of it is quite efficient and the majority of the cells in the infiltrated area will start expressing recombinant proteins after two days. Small areas from infiltrated leaves can be taken as samples for analysis under the microscope (Sparkes *et al.*, 2006).

Agrobacterium tumefaciens is an etiological agent for the plant crown gall disease, in which the gall comes from the transfer, integration, and expression of a set of

(a) Infiltration with a suspension of *Agrobacterium* tumefaciens containing expression vector pVKH18En6-GFP-HDEL

(b) After 72 h, sections from the infiltrated leaves were incubated in 1.0 μM latrunculin B for 30 min

Figure 2.3: Leaf infiltration with *Agrobacterium*.

genes called *T-DNA*. The genes in *T-DNA* can be replaced by any DNA sequence, which makes *Agrobacterium* tumefaciens ideal for gene transfer (Balbás, 2004). The genetic transformation starts by the transformation of *T-DNA*[4] from *Agrobacterium* tumefaciens to the host cell. *T-DNA* will then be integrated into the host cell's genome. The introduced genes will finally be expressed in the transformed host cells.

After the induction of the *Agrobacterium Vir* protein machinery by phenolic compounds, the *VirD1* and *VirD2* proteins nick both borders at the bottom strand of the *T-DNA*. This gives a single-stranded *T-DNA*, which, together with several *Vir* proteins, is exported into the host cell's cytoplasm through a channel formed by *Agrobacterium VirD4* and *virB* proteins. The T-strand with one *VirD2* molecule covalently attached to its 5'-end, which is the end of the T-strand which has the fifth carbon in the sugar-ring of the (deoxy)ribose at its terminus (Lodish *et al.*,

[4]A discrete set of genes from *Agrobacterium* tumefaciens located on the tumor inducing (Ti) and delimited by a pair of 25-bp repeats; named left and right borders (Balbás, 2004)

2004), and coated with many *VirE2* molecules forms a *T-DNA* transport complex. The *T-DNA* complex is imported into the host cell's nucleus with the help of *VirD2* and *VirE2*. Integration of the T-strand into the host cell's genome is believed to be facilitated by *VirD2* and *VirE2* (Balbás, 2004).

2.11 Chapter Summary

In conclusion the ER is an ordered **connected** membranous network that can be found in all eukaryotic cells; it is the port of entry into the secretory pathway; and is responsible for the synthesis, modification, assembly, proper folding or degradation, and the delivery of biologically active proteins to the proper target sites in the cell, its membranes, and the extra-cellular space (see Schröder & Kaufman (2005a) and Schröder & Kaufman (2005b)).

The form of the ER is conserved across eukaryotic cells, which stresses the importance of its role in the secretory pathway in particular and the cell in general (Voeltz & Prinz, 2007). This thesis considers three essential ER subdomains: nuclear, nytosolic, and cortical ER, focussing on the cytosolic subdomain.

The form of the ER is believed to be controlled by four types of proteins: (a) the first type stabilises the curvature of the ER membrane (b) the second type tethers the membrane to other cell compartments (c) the third regulates fission and fusion of the ER membrane (d) and the fourth type shapes the ER by stabilising certain morphologies (see Voeltz *et al.* (2002) and Voeltz & Prinz (2007)). Altogether, although considerable research has been devoted to understanding the role and functions of the ER, rather less effort has been paid to its geometric quantification despite the major role geometry plays in defining many of its functional attributes. The purpose of the remainder of this thesis is to develop a set of computational tools to help fill this gap.

Does the ER form change from one position of the cell to another? What are the

dynamic properties of the ER? Do they vary with location? Are they the same across different cell types? Do they change with different physical conditions? Is confocal microscopy appropriate to answer these questions and what are its limitations? The answer to these questions will lead to a more fundamental question; that is the relationship between the form and optimal function of the ER. GFP serves as an appropriate means of studying the ER, *in vitro* as well as *in vivo*; and taking advantage of the recent developments in computer graphics and confocal imaging, this thesis addresses the above questions by bringing together computer science, mathematics and biology, focussing on plant ER. As already stated in Chapter 1, this thesis presents a collection of computational tools to help scientists study the form and movement of the endoplasmic reticulum, and similar network-like structures, whose data were acquired, digitised, and stored using a confocal microscope. The methods proposed are based on the representation of the reticulum by its skeleton, which is abstracted by a graph, to simplify the analysis and exploit the well established graph theory algorithms. The following chapter highlights the protocol followed to prepare the samples, and the equipment used to acquire the data.

Part II

Methodology

3

Data Acquisition

After the overview of the ER in Chapter 2, this chapter takes a closer look at the origin of the data, and how it was obtained. It consists of two principal sections: (a) sample preparation -the leaf infiltration with *Agrobacterium* method; and (b) data acquisition to describe the equipment used in collecting the data, i.e. confocal laser scanning microscopy, reviewing the fundamental aspects of confocal microscopy, that are relevant to the overall aim of the thesis. Attention is paid to the resolution power of the equipment, as well as the main sources of noise and how it may affect the final results.

3.1 Introduction

As is the case for other organelles in the cell, it is essential to find an appropriate, easy to handle model to study the form and movement of the ER using confocal microscopy. Vegetative cells offer a suitable model because of their pleiomorphic nature (Staehelin, 1997). In this type of cell, the central vacuole occupies more than 90% of the overall volume of the cell (Marty, 1999; Reisen *et al.*, 2005). Consequently, turgour pressure[1] forces the ER against the plasma membrane and the cell wall, which results in the flattening of the ER into a thin, almost two dimensional layer, making the plant ER a convenient candidate model with reduced geometric complexity; so instead of dealing with a 3D network, which can be considerably more complex to handle, the problem reduces to the analysis of a 2D network.

It is already stated in Chapter 2, that studying the ER generally involves genetic transformation (DNA) and can be achieved in several ways. This thesis chooses the leaf infiltration with Agrobacterium method (see Figure 2.3 on page 22), because it is relatively fast, and highly efficient (Chen & Dubnau, 2004). Epidermal cells from infiltrated leaves can be analysed between two and five days after infiltration; in contrast to the three-month timescale of generating stable transgenic lines (see Section 2.10 on page 21).

In our chosen method, Agrobacterium mediates the transfer of DNA into the genome of only a small region of the leaf. Furthermore, transfection is relatively efficient and most of the cells within the infiltrated area start expressing recombinant proteins within two to three days (Balbás, 2004).

[1] An outward force exerted by the plant cell's content on its wall

3.2 Sample preparation

Unless otherwise indicated, all calculations in the remainder of this study are related to *Nicotiana tabacum* cv Petit Havana, from which healthy, five to eight week old leaves grown in greenhouse conditions, were selected for agroinfiltration. Using a syringe without a needle, these leaves were infiltrated with a suspension of *Agrobacterium* tumefaciens (see Figure 2.3(a) on page 22 for clarification), which is a trans-kingdom DNA transfer capable plant pathogen, containing expression vector pVKH18En6-GFP-HDEL as described in Batoko *et al.* (2000).

The genetic transformation starts with the transformation of T-DNA from *Agrobacterium* tumefaciens to the selected *Nicotiana tabacum* cv Petit Havana SR1 cells (Agrobacteria were at an OD_{600}[2] of 0.05). T-DNA was integrated into the host cells' genome; and the introduced genes were expressed in the transformed host cells (see Section 2.10.1 on page 21 for details).

The following step in sample preparation depends on whether the aim is to study the static or dynamic ER. In the case of the latter (see Chapter 8 on page 135), and after around $72h$, the next step is to cut a small piece from an infiltrated leaf, mount it in water then observe it under the a confocal microscope (Leica TCS SP2 or Leica TCS SP5 in the case of this thesis, see Figure 3.1(a) on page 30 and Figure 3.1(b) on page 30).

In the static ER case, and since we are dealing with optical z-sectioning, explained in section 3.3.1 page 31, it is altogether impossible, with the available microscopes, to obtain consistent z stacks without stopping the ER movement, due to its dynamic nature (see Section 2.1 on page 9).

For this reason, small pieces, about $1.0cm^2$, from the infiltrated leaves were cut, then incubated in 1.0 μM Latrunculin B (Calbiochem, Nottingham, UK), for 30 min, to decelerate the movement of the ER (see Chapter 7), before they were mounted in

[2] OD_{600} refers to the optical density at $600nm$, the measure of the amount of light absorbed by the suspension of Agrobacteria.

water and imaged using a Leica TCS SP5 confocal microscope (see Figure 3.1(a) on page 30).

(a) (b)

Figure 3.1: Two Leica microscopes were used in this study: (a) Leica TCS SP2: is used in the static ER analysis, (Leica, 2000) (b) Leica TCS SP5 (Leica, 2005) is used in the dynamic ER analysis. It can resolve structures as little as $200nm$ apart in the confocal plane and up to 400 nm in the optical plane, and it is equipped with a galvo stage that provides fast z stacking with a stack as thick as 1.5 mm (while Leica TCS SP2 can only image stacks up to 166 μm (Leica, 2005)).

3.3 Confocal microscopy

It is already known from Chapter 2 that an ER tubule is less than a micron in diameter, and is conserved across cell types (Voeltz *et al.*, 2006). An appropriate high resolution microscope is therefore indispensable to study the form and movement of the ER. Despite being able to resolve structures in the region of $1nm$, and thus surpassing other microscopy techniques; trans. electron microscopy TEM is inappropriate to study the geometry of the ER, because the latter is spread in three dimensional space; while EM requires thin, almost 2D sections (see Section 2.2 on page 9). Furthermore, conventional widefield fluorescence microscopy images, whose

z-dimensions are larger than the wave-optical depth, are commonly contaminated with light coming from out-of focus planes (Wilhelm *et al.*, 2003), and thus require extra effort to obtain reliable results.

An alternative to both techniques is confocal microscopy (CM); because it has the advantage over both techniques not only by allowing one to image tubular ER; but also by enabling the microscopist to obtain improved resolutions, with high contrast optical sections, by restricting image information to thin, 0.5 to 1.5 μm, optical layers, through the specimen to obtain reduced out-of-focus artefacts, and improved signal-to-noise (SNR) ratios (Claxton *et al.*, 2008).

Combined with an appropriate visualisation software such as *Amira* (Zuse, 2006), *Volocity* (Improvision, Waltham, MA), *Imaris* (BitPlane, Inc.), or similar software packages, the optical sectioning capability of CM has been exploited to derive 3D representations of different organelles, which can optically be sectioned through arbitrary angles.

This thesis uses the 3D representation of the ER to obtain its approximate geometric, and dynamic properties, including: lengths of individual branches, their outer surface areas, their local diameters, and volumes; as well the average junction displacement, speed, acceleration, and moments of displacements (see Chapters 7 and 8 for details). The next section is a summary of the aspects of CM, that are relevant to the thesis.

3.3.1 An overview

CM, depicted in Figure 3.2 on page 32, was invented by Marvin Minsky in 1957 who, in order to visualise neurons in vivo, conceptually improved conventional light microscopy by introducing two novel ideas: (a) he placed **a pinhole, at a position confocal with the point in the sample**, to reject any light that has not originated from the focal plane; and (b) rather than illuminating the entire plane of focus

all at once, as in the case of conventional microscopy, Minsky **sequentially illuminated each point in turn**; to avoid contamination with unwanted light spread as a result of illuminating the entire plane of focus (Paddock, 2001; Prasad *et al.*, 2007; Semwogerere & Weeks, 2005).

To sum up Minsky's design **confocal microscopy is based on point illumination and point detection**; and its main advantage over conventional microscopy is the reduction of the out-of-focus glare originating from the scattered light coming from the planes above and below the plane of focus.

Arguably considered among the most notable advances in microscopy according to Claxton *et al.* (2008), Minsky's invention still forms the basis of modern confocal laser scanning microscopy. Enhanced with modern optoelectronics, the discovery of the green fluorescent protein GFP, and the recent advances in computer graphics, it has a considerable impact on biological imaging. It is this combination that allows the derivation of 3D reconstructions of specimens, and permits one to obtain

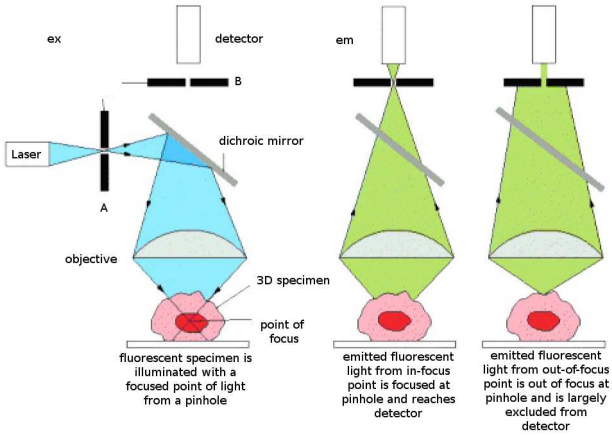

Figure 3.2: The principle of CM. To produce an image element(pixel), the high intensity light of an appropriate wavelength reaches the specimen after hitting the dichroic mirror (left image). The excited specimen emits light of a different wavelength that passes through the dichroic mirror and the pinhole. The pinhole allows only light that has originated in the focal plane to reach the final destination, that is the PMT (middle image); light from other planes is rejected (left image). The PMT detects, and converts the signal (light) from analogue to digital via an AD converter. A computer stores the pixel information into a local memory. The system carries out the same procedure for all points in the current focal plane point-by-point, before it moves to the next plane; and repeats the same task. Once it scans the whole specimen the computer, with an appropriate software, can generate a 3D representation of the specimen. Figure taken from (Leica, 2000)

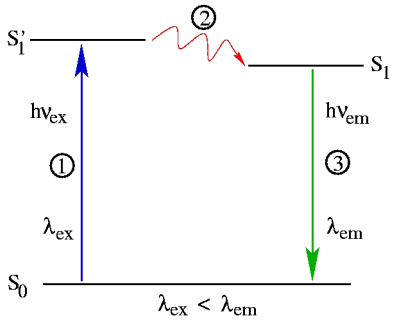

Figure 3.3: The principle of fluorescence: (1) the fluorophores are raised from their ground state, S_0, to a higher unstable energy state S_1', (2) fluorophores lose part of the energy, in the form of heat, chemical reactions or through collisions with neighbour molecules, and consequently drop to an intermediate energy state, S_1, (3) finally fluorophores drop to their initial, stable, ground state while emitting light of a larger wavelength, i.e. lower energy. Figure taken from (Leica, 2005).

their arbitrary projections by producing stacks of sharp sections, restricted to thin focus planes, taken at different positions along the optical axis **without physically damaging the specimen** (Semwogerere & Weeks, 2005). CM may therefore be used to image both static (fixed) and dynamic (live) ER.

There are two CLSM imaging modes: (a) a **reflection mode** where light is reflected off the sample to produce an image, as in the case of the *brain micro-vascular network* (Fouard *et al.*, 2006); and (b) a **fluorescence mode**: where fluorescence is stimulated from fluorophores[3] applied to the sample. The former is usually used to study the topography of the surface of tissues, while the latter mode is used in studying one, or more organelles by attaching multiple fluorophores to each one of them. What is common about the two modes is that they both rely on fluorescence to produce an image.

Figure 3.3 on page 33 summarises the principles of the fluorescence mode, which are relevant to this thesis: (1) the applied high intensity light, or laser, of an appropriate wavelength λ_{ill} (with the corresponding excitation energy $E_{ill} = h\nu_{ill} = hc/\lambda_{ill}$, where "ill" refers to illumination)[4], raises the fluorophores (GFP), in the specimen from their ground, stable, energy state, denoted S_0, to an unstable higher

[3] A fluorophore is a fluorescent molecule

[4] $h = 6.62606896(33) \times 10^{-34} Js$ is Planck's constant; $c = 299,792,458 m/s$ is the speed of light; and ν_{ill} is the frequency

energy state S_1'; part of the excitation energy dissipates, in the form of heat, chemical reactions, or collisions with other molecules; causing (2) the fluorophores to pass to an intermediate state S_1; finally (3) the fluorophores return to their initial stable state, after re-emitting light of a different colour having a lower energy $E_{em} = h\nu_{em} = hc/\lambda_{em}$. The final image is formed from the emitted light as explained in the next paragraph.

The formation of an image element (pixel) in CLSM can be summarised in the following steps (see Figure 3.2 on page 32):

(i) the **focused spot of light** (laser with $\lambda_{ill} = 488nm$ in the current experimental settings) passes through the confocal pinhole (A), before it reaches the dichroic mirror, which reflects it towards the objective.

(ii) once it reaches the specimen, the laser illuminates a **single point** in the focal plane for a short time (dwell time), just enough to stimulate fluorescence from the GFP applied to the specimen (between 5 to 50 μs (Stelzer, 2001)).

(iii) The stimulated GFP, fluoresces, as explained above, emitting light with a larger wavelength ($\lambda_{em} = 507nm$, i.e. lower energy, in the current experimental setting),

(iv) the emitted light passes through the objective, and is allowed to pass through the dichroic mirror, and finally pinhole (B) to reach its final destination that is the Photomultiplier (PMT) tubes, which detects it and passes it to an analogue-to-digital converter which transforms it into a pixel that is recorded by a computer,

(v) an *XY scan controller* (see Figure 3.4 on page 35) directs the laser spot to scan the entire focal plane and build the corresponding 2D image. An appropriate *galvo stage* moves the specimen sequentially to the next focal plane to form the next image,

(vi) the entire 3D specimen is scanned in this fashion, and the series of images of the different focal planes (optical sections) is used to reconstruct the 3D specimen.

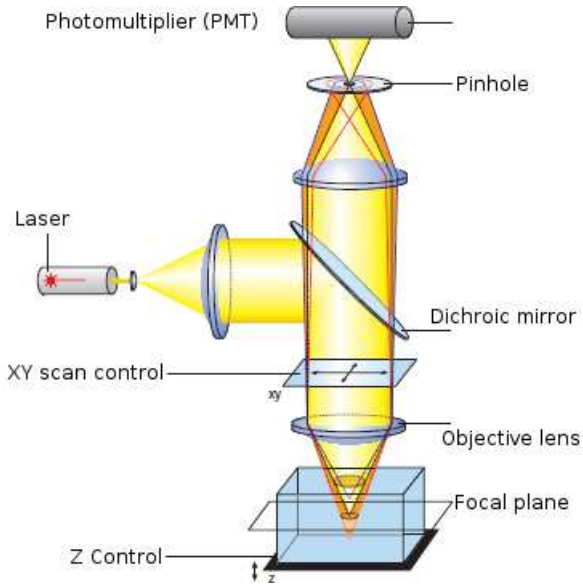

Figure 3.4: The main elements in CLSM. The main players in modern CLSM are: (a) the pinhole, which improves the resolution and the contrast of the final image (b) the PMT, which detects light passing across the pinhole (c) the excitation laser, or precisely its wavelength to cause the specimen to fluoresce (d) the *XY scan controler* to illuminate the focal plane point-by-point, (e) the z-control which controls the thickness of the focal sections and allows stacks of images to be obtained (f) the dichroic mirror that allows only the light reflected from the sample to reach the pinhole. Figure taken from (Wilhelm *et al.*, 2003).

In conclusion, the main optical elements that characterise a CLSM, that are relevant to this study, are: (a) **the pinhole**, featured by its diameter (D_{ph}), and (b) **the objective** characterised by its numerical aperture (NA), and magnification. Both of these elements are explained in the following sections.

3.3.2 The objective

The objective is a set of rotational symmetric optical lenses, which allow one to localise, focus, and magnify the specimen. Both light gathering and resolution

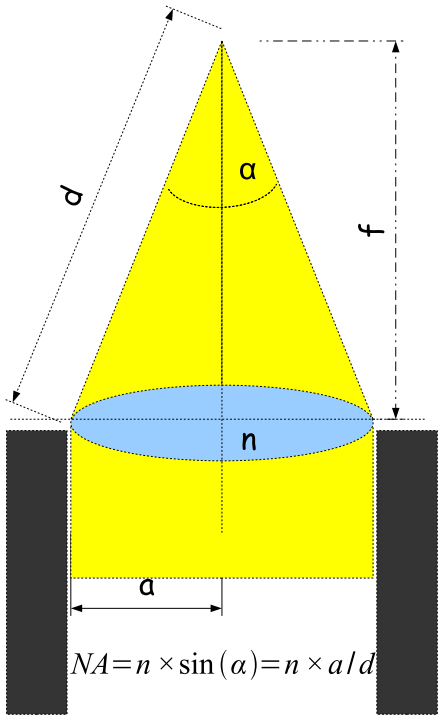

Figure 3.5: The numerical aperture (NA) of a confocal microscope characterises its objective and it depends on the index of refraction of the working medium (n) and the angle under which light enters the front lens of the microscope.

capacities of an objective depend on its numerical aperture (NA), which is a function of two parameters: the aperture angle (α), the angle under which light enters into the front lens of the objective, and the index of refraction n of the working medium (see Figure 3.5 on page 36); $NA = n \cdot sin\alpha$ (Leica, 2000). NA together with the wavelength of the excitation laser λ_{ill} play a critical role in both lateral and axial resolutions that can be attained with CLSM as discussed in the following sections (Semwogerere & Weeks, 2005, and references therein).

The magnification of an objective, denoted by M_o, is defined as the ratio between an object's size and the image's size; i.e. the factor by which the original size of the specimen is multiplied, to produce the final image; $M_o = S_i/S_s$, where S_i and S_s are the image size and specimen size respectively.

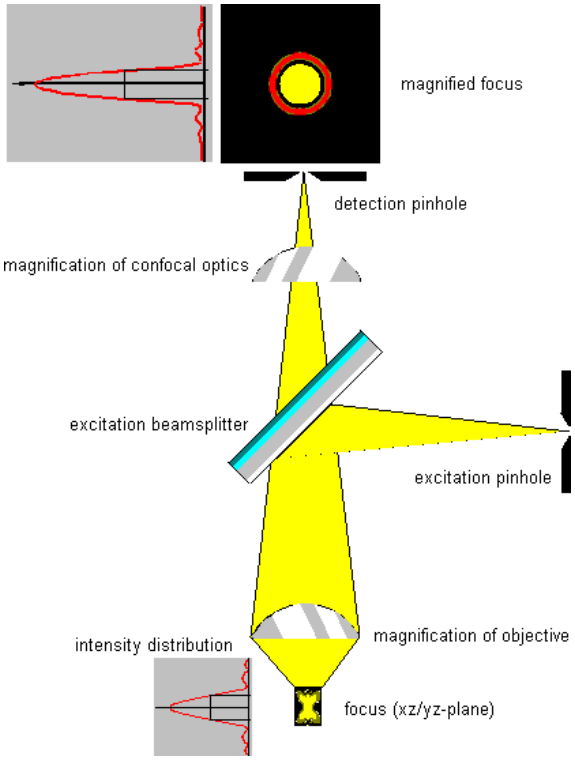

Figure 3.6: The pinhole and the formation of a PSF: the pinhole is a spatial filter which prevents out-of-focus light reaching the PMT. It causes a point light source to appear as an Airy disc (top right), whose size depends on the numerical aperture of the front lens, the wavelength of the excitation light, the magnification of the objective, and the magnification factor of the optical system (Leica, 2000). The numerical aperture (NA) is a function of the index of refraction (n) of the working medium, and the angle under which light enters into the front lens of the microscope. The z-intensity vs distance from the optical axis profile takes the form of a bell (bottom left and top left), and the thickness of the optical section is defined by the full width half maximum (FWHM) of this profile.

3.3.3 The pinhole

The pinhole is a spatial filter whose main role is to reduce the amount of out-of-focus light, originating from the planes other than the focal plane, from reaching the PMT; and so to improve the contrast and resolution of the final image (Figure 3.6 on page 37).

Small pinhole diameters produce thin optical sections, better z-resolutions, but weak image signals; while large pinhole diameters degrade the confocal effect by producing thicker optical sections, lower z-resolutions and stronger image signals (Pawley, 1995). Therefore, in addition to influencing the resolution, and the thickness of the

optical slices; **the pinhole size also influences the amount of noise produced in the final image**. An optimal pinhole size has, therefore, to be carefully adjusted to obtain the optimal compromise between efficiency and resolution.

According to Pawley (1995), for most fluorescent applications, a pinhole diameter of about 1 AU is the best compromise, where AU refers to the diameter of the *Airy disc*, that is the inner, light circle of the diffraction pattern of a point light source (Leica, 2000). The diameter of the Airy disc depends on the wavelength of the excitation light, the numerical aperture of the lens, and the optical system of the microscope. In the case of Leica TCS SP2, it is given by: $d_{Airy} = (1.22 \times \lambda/NA) \times M_o \times 3.6$; where M_o is the magnifying factor of the objective; and 3.6 is specific to Leica TCS SP2 confocal microscope, and refers to the magnification of other optical components in the system. The unit of measurement of the pinhole is the Airy unit.

3.3.4 Optical resolution power

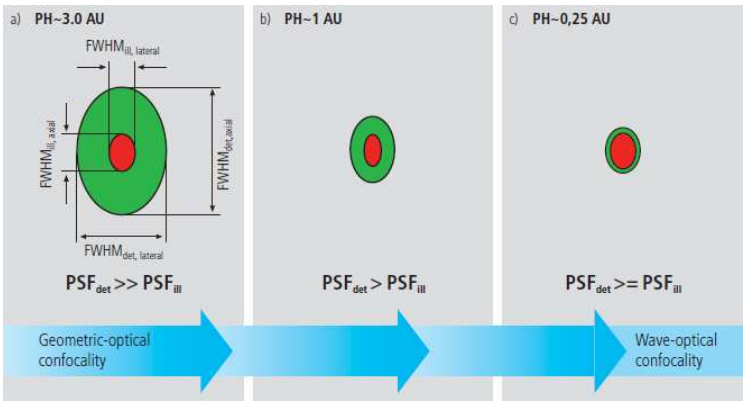

Figure 3.7: Confocality: The pinhole diameter decreases from the geometric-optical confocality shown in (a) to the wave-optical confocality shown in (c). In the case of very large pinhole diameters (a) PSF_{det} is very large compared to PSF_{ill} and the laws of the geometric-optical confocality dominate, whereas in the case of small pinhole diameters PSF_{det} becomes closer to PSF_{ill} and the laws of wave-optical confocality apply. Accordingly, PSF_{det} shrinks until it approaches the order of magnitude of PSF_{ill} (c). A diameter of 1 AU is a typical setting (b). Figure taken from (Wilhelm *et al.*, 2003).

In general terms, resolution may be defined as the minimum distance at which the image of two point light sources, acquired by an optical system, can be distinguished

by the human eye. When acquired by a CLSM, the image of a single point light source has the profile of an ellipsoid of rotation and is commonly described by the intensity point spread function (PSF), a function which maps the intensity distribution of the object point into the image space, and is expressed in terms of the distance from the centre of the ellipsoid; $I = I(d)$.

When projected into the focal plane, the intensity PSF has the profile of a rotational symmetric Airy disc, with equivalent X and Y components due to the cylindrical symmetry of the objective lens.

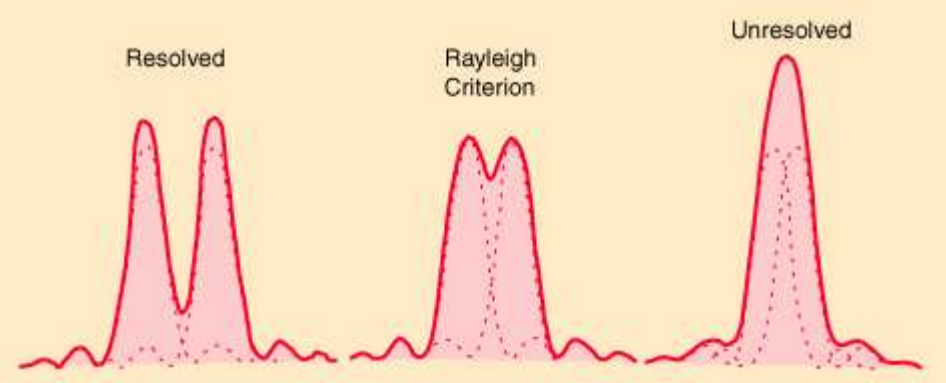

Figure 3.8: An illustration of the Rayleigh criterion: two points can be resolved if the maximum intensity of the Airy disc of one of them and the first minimum of the Airy disk of the second are aligned. Left (resolved points): the distance separating the maximum intensity of the Airy disc of one point and the first minimum intensity of the Airy disc of the other is larger than the distance between the maximum and the first minimum intensities of the point's Airy disc. Middle (Rayleigh Criterion): the distance separating the maximum intensity of the Airy disc of one point coincides with the first minimum intensity of the Airy disc of the other. Right (unresolved points): the distance separating the maximum intensity of the Airy disc of one point and the first minimum intensity of the Airy disc of the other is smaller than the distance between the maximum and the first minimum intensities of the point's Airy disc (Figure taken from phy-astr.gsu.edu).

Resolution, in CLSM, can be quantified using contrast which, given two point light sources of equal intensity distributions I, is defined as the normalised difference between their maximum intensity and the minimum intensity in the space separating them: $C = (I_{max} - I_{min})/I_{max}$ (Claxton *et al.*, 2008). This means that contrast varies in the interval $[0, 1]$ and reaches its maximum value (one) when the two PSFs

are completely separated, and as soon as they start to overlap the contrast starts to diminish until it reaches its minimum (zero), i.e. when the two PSF are no longer perceptible.

Quantitatively, resolution is defined as the separation distance which corresponds to a certain contrast value; the **Rayleigh criterion**, which states that *two points can be resolved if the maximum intensity of the Airy disc of one of them and the first minimum of the Airy disk of the second are aligned* (see Figure 3.8 on page 39), is commonly used to determine the contrast value which determines the resolution in fluorescence microscopy. The Rayleigh criterion corresponds to a contrast value of 26.4% (Claxton *et al.*, 2008).

Taking into consideration that a CLSM is based on the illumination and detection of a single point; the total 3D PSF, denoted PSF_{tot}, of a point light source, assuming uniform pupil illumination with no optical aberration, can be split into two independent terms: an illumination term PSF_{ill}, which is a mapping of the laser spot into the object space; and a detection term PSF_{det}, a further mapping of the emitted light into the image space;

$$PSF_{tot}(x, y, z) = PSF_{ill}(x, y, z) \cdot PSF_{det}(x, y, z). \tag{3.1}$$

Both $PSF_{ill}(x, y, z)$ and $PSF_{det}(x, y, z)$ depend on the excitation wavelength λ_{ill}, the numerical aperture NA of the objective lens, the diffraction at the objective, the aberration of the microscope's optical components, the mismatch in diffraction between the immersion liquid and the mounting medium, as well as the extent of the laser depth below the specimen surface. $PSF_{det}(x, y, z)$ depends also on the pinhole diameter (Wilhelm *et al.*, 2003).

The optical lateral (δ_{XY}) and axial (δ_Z) resolutions of a CLSM, in the case of biological fluorescent specimens, which is the case of this thesis, can be approximated by the full width at half maximum of the intensity distribution (FWHM) of PSF_{ill}

(see Figure 3.7 on page 38).

Different empirical formulae to approximate the lateral and axial resolutions as well as the optical thickness have been developed and can be found in the literature. For the axial resolution, Piller (1977) suggested

$$\delta_Z \simeq \frac{1000}{7 \times NA \times M_t} + \frac{\lambda_{ill}}{2 \times NA^2},$$

where M_t is the total magnification of the microscope and λ_{ill} the illumination wavelength. By discarding the first term in the above expression, Born & Wolf (1980) used

$$\delta_Z \simeq \frac{\lambda_{ill}}{2 \times NA^2}$$

instead.

Young (1996) found that neither of these formulae work in practical situations, and based on standard diffraction wave theory, showed that δ_Z can be approximated by

$$\delta_Z = \frac{\lambda_{ill}}{4 \times n(1 - \cos\alpha)}.$$

Ho & Shao (1991) suggested a more accurate formula that has become widely acceptable among microscopists. Ho & Shao based their formula on a point light source imaged in the reflection mode assuming a perfect plane mirror and obtained

$$\delta_Z = \frac{0.4\lambda_{ill}}{n(1 - \cos\alpha)}$$

Given that the diameter of the detection pinhole is PH Wilhelm *et al.* (2003) use the following:

- **Case 1:** $PH > 1.0AU$ Both lateral and axial resolutions can be approximated using the FWHM of PSF_{ill} and they are given by:

– **Lateral**

$$\delta_{XY} = FWHM_{ill,lateral} = \frac{0.51 \times \lambda_{ill}}{NA}$$

– **Axial**

$$\delta_Z = FWHM_{ill,axial} = \frac{0.88 \times \lambda_{ill}}{n - \sqrt{n^2 - NA^2}}$$

which can also be written as

$$\delta_Z = \frac{0.88 \times \lambda_{ill}}{n\left(1 - \sqrt{1 - \left(\frac{NA}{n}\right)^2}\right)}$$

and in the case of $NA < 0.5$, $(NA = n \sin\alpha)$, $FWHM_{ill,axial}$ can be approximated by a first order Taylor approximation as follows:

$$\delta_Z \simeq \frac{0.88 \times \lambda_{ill}}{n\left(1 - \left(1 - \frac{1}{2} \cdot \left(\frac{NA}{n}\right)^2\right)\right)}$$

And after rearrangement gives

$$\delta_Z \simeq \frac{1.76 \times n \times \lambda_{ill}}{NA^2}$$

- **Case 2:** $PH < 0.25AU$ In this case the PSF_{ill} and PSF_{det} are almost identical, so $PSF_{tot}(x, y, z) = (PSF_{ill}(x, y, z))^2$, and the above expressions are replaced by the following

  – **Lateral**

$$\delta_{XY} = FWHM_{ill,lateral} = \frac{0.37 \times \bar{\lambda}}{NA}$$

where $\bar{\lambda}$ is the mean wavelength given by:

$$\bar{\lambda} = \sqrt{2}\frac{\lambda_{ill} \cdot \lambda_{em}}{\sqrt{\lambda_{ill}^2 + \lambda_{em}^2}}$$

– **Axial**

$$\delta_Z = FWHM_{ill,axial} = \frac{0.64 \times \bar{\lambda}}{n - \sqrt{n^2 - NA^2}}$$

Following the same logic as above this can also be written as

$$\delta_Z = \frac{0.64 \times \bar{\lambda}}{n\left(1 - \sqrt{1 - \left(\frac{NA}{n}\right)^2}\right)}$$

and in the case of $NA < 0.5$, $(NA = n \sin\alpha)$, $FWHM_{ill,axial}$ can be approximated by Taylor first order approximation as follows:

$$\delta_Z \simeq \frac{0.64 \times \bar{\lambda}}{n\left(1 - \left(1 - \frac{1}{2} \cdot \left(\frac{NA}{n}\right)^2\right)\right)}$$

and after rearrangement gives

$$\delta_Z \simeq \frac{1.28 \times n \cdot \bar{\lambda}}{NA^2}$$

- **Case 3:** $0.25AU < PH < 1.0AU$ in this case the lateral and axial resolutions can be obtained by linear interpolation

In general the lateral and axial resolutions can be approximated (Taylor first order approximation), in terms of NA, λ_{ill}, and λ_{det}, by the following formulae:

$$\delta_{XY} \simeq \frac{const_l \cdot \lambda}{NA} \tag{3.2}$$

$$\delta_Z \simeq \frac{const_a \cdot \lambda}{NA^2} \tag{3.3}$$

where $const_l$, and $const_a$ are constant real numbers.

The optical slice thickness, according to Wilhelm *et al.* (2003), is given by

$$FWHM_{axial,det} = \sqrt{\left(\frac{0.88\lambda_{ill}}{n - \sqrt{n^2 - NA^2}}\right)^2 + \left(\frac{\sqrt{2} \cdot n \cdot PH}{NA}\right)^2}$$

The first term under the root is the contribution of the wave-optical confocality, while the second term is the contribution of the geometric-optical confocality; and we distinguish two cases:

- In the case of very small pinhole diameters, i.e. when $PH < 0.5AU$, PSF_{det} approaches the order of magnitude of PSF_{ill} (ideal case), and the image obeys the laws of optical confocality. i.e. the optical slice thickness can be approximated by:
$$FWHM_{axial,det} \simeq \frac{0.88\lambda_{ill}}{n - \sqrt{n^2 - NA^2}}$$

- In the case of large pinhole diameters, i.e. when $PH > 1.0AU$, PSF_{det} is much larger than PSF_{ill} (conventional microscopy case), the image is formed according to the geometric optical confocality laws, and so can be approximated by:
$$FWHM_{axial,det} \simeq \frac{\sqrt{2} \cdot n \cdot PH}{NA}$$

The case of Leica Leica provides $const_l = 0.4$ for the lateral resolution, i.e.

$$\delta_{XY} \simeq 0.4 \times \frac{\lambda_{ill}}{NA} \tag{3.4}$$

and adopts Ho & Shao (1991), which predicts the FWHM of a point in the reflected mode for a perfect plane mirror, in terms of α, λ_{ill}, and n by

$$\delta_Z \simeq 0.45 \times \frac{\lambda_{ill}}{n(1 - \cos\alpha)} \tag{3.5}$$

or in terms of NA, λ_{ill}, and n, using $NA = n \cdot \sin\alpha$

$$\delta_Z \simeq 0.45 \times \frac{\lambda_{ill}}{n - \sqrt{n^2 - NA^2}} \tag{3.6}$$

The remaining sections will use Equations 3.4 and 3.6 to approximate the best lateral and axial optical resolutions that can be obtained using Leica TCS SP2.

In the current experimental settings $\lambda_{ill} = 0.488\mu m$, $n = 1.5$(oil emission), and $NA = 1.3$; which means that the theoretical lateral and axial optical resolutions are respectively

$$\begin{aligned} \delta_{XY} &\simeq 0.4 \times \frac{0.488}{1.3} \\ &\simeq 0.150\mu m \end{aligned}$$

and

$$\begin{aligned} \delta_Z &\simeq 0.45 \times \frac{0.488}{1.5 - \sqrt{1.5^2 - 1.3^2}} \\ &\simeq 0.292\mu m \end{aligned}$$

the smallest resolvable structure (in μm), in the current experimental settings, is therefore

$$\mathbf{resel}(\delta_{\mathbf{XY}}, \delta_{\mathbf{XY}}, \delta_{\mathbf{Z}}) = (\mathbf{0.150}, \mathbf{0.150}, \mathbf{0.292})$$

Since the diameter of an ER tubule is around $200nm$ (Voeltz *et al.*, 2002), CLSM can resolve the ER tubules and hence allows one to estimate key geometric properties of tubules such as the average diameter, surface area and volume. Furthermore, the calculated theoretical optical lateral and axial resolutions show that the former is less than the reported ER tubule diameter, while the latter is slightly greater, and consequently, assuming that the ER is cylindrical as reported by (Voeltz *et al.*,

2002), a 2D lateral analysis might be more accurate than a 3D one because of this limitation (see Chapter 8).

3.3.5 Optimal voxel size

The previous sections have reviewed the theoretical resolutions and the optical thickness imposed by the CLSM optical system to obtain the minimum resolvable element resel(δ_{XY}, δ_{XY}, δ_Z); but have not taken into account the analogue-to-digital conversion of data to allow its storage in a digital format, which can be processed and analysed. A certain number of pixels(voxels) is necessary to map the object into the computer screen without loss of information; therefore the next issue to consider is the sampling frequency.

Nyquist theorem states:

Theorem 3.3.1. ***(Nyquist theorem)***

the smallest optically resolvable distance can be digitised without loss of information if it is scanned with at least 2 pixels, see (Nyquist, 2002),

implying that the above optical resolutions have to be divided at least by 2 to obtain the size of a pixel, which retains the information of the optically resolvable structures; and so in the case of Leica the size of a voxel (a volume element) can be obtained using:

$$d_{XY} < 0.2 \times \frac{\lambda_{ill}}{NA} \tag{3.7}$$

and

$$d_Z < 0.23 \times \frac{\lambda_{ill}}{n(1-\cos\alpha)} \tag{3.8}$$

or in terms of NA, λ_{ill}, and n

$$d_Z < 0.23 \times \frac{\lambda_{ill}}{n - \sqrt{n^2 - NA^2}} \tag{3.9}$$

Both lateral and axial resolutions depend on the numerical aperture of the objective and the wavelength. Given that $\lambda_{ill} = 0.488\mu m$, $n = 1.5$(oil emission), and $NA = 1.3$; it follows that the theoretical optimal pixel size is:

$$\begin{aligned} d_{XY} &< 0.2 \times \frac{0.488}{1.3} \\ &< 0.075\mu m \end{aligned}$$

$$\begin{aligned} d_Z &< 0.23 \times \frac{0.488}{1.5 - \sqrt{1.5^2 - 1.3^2}} \\ &< 0.146\mu m \end{aligned}$$

The maximum size of a voxel (in μm), which retains the information of an optically resolved structure, according to the current experimental settings, is therefore:

$$\mathbf{Voxel(d_{XY}, d_{XY}, d_Z) = (0.075, 0.075, 0.146)}$$

3.4 Noise in confocal images

As in the case of any other electronic device, noise originates throughout the signal generation chain and may degrade the final image. This is true even in the case of properly optically resolved points that are sampled according to Nyquist theorem. Points that are theoretically resolved may appear unresolved, and points which are normally unresolved may appear resolved because of noise.

Young (1996) identifies many types of noise, namely: laser noise, shot noise, read out noise, amplifier noise, dark current noise, and quantisation noise. These types of noise can be grouped into two principal categories: they can either be (a) periodic such as amplifier noise and read out noise, or (b) non-periodic such as shot noise and dark current noise. While modern CLSM are usually optimised against periodic noise, see (Leica, 2000, 2005; Wilhelm *et al.*, 2003), they do not take into account non-periodic noise because of its stochastic nature.

Wilhelm *et al.* (2003) highlights three main types of non-periodic noise: detector noise ($\epsilon_{detector}$), laser noise (ϵ_{laser}), and shot noise (ϵ_{shot}). Detector noise, according to (Wilhelm *et al.*, 2003), can be neglected in most practical situations; furthermore laser noise is dominant when $N_e > 10,000$, where N_e is the number of photons that reach the PMT (see Figure 3.2 on page 32). This type of noise occurs mainly in the reflected mode. When $N_e < 1000$ shot noise is more dominant and laser noise can be neglected.

Based on the above discussion, an image $\mathcal{I}$ can be expressed in terms of the signal S and the total noise ϵ_t

$$\begin{aligned} \mathcal{I} &= S + \epsilon_t \\ \epsilon_t &= \epsilon_{periodic} + \epsilon_{non-periodic} \\ &\simeq \epsilon_{detector} + \epsilon_{laser} + \epsilon_{shot} \\ &\simeq \epsilon_{shot} \\ \therefore \quad \mathcal{I} &\simeq S + \epsilon_{shot} \end{aligned}$$

Shot noise follows a Poisson distribution, and usually occurs in the fluorescence mode. It is generated from the discreteness of the current flow, whose spectral density is proportional to the average current. Beenakker (1999) describes shot noise by: *"a white noise spectrum up to a certain cut-off frequency, which is related to the time taken for an electron to travel through the conductor. In contrast to*

thermal noise, shot noise cannot be eliminated by lowering the temperature $\cdots$ *"*. This is the most prominent type of noise according to Pawley (1995), because it limits the image Signal-to-noise ratio (SNR).

The number of photons contained in the incident beam, with light of power P, is given by:

$$n_p = \frac{P \cdot t \cdot \lambda}{h \cdot c}$$

where c is the speed of light, and h is Planck's constant.

SNR is calculated by dividing the mean by the square root of the variance

$$SNR = \frac{\mu}{\sqrt{var}}$$

In a Poisson distribution the mean is equal to the variance $\mu = var = n_p$, and noise is proportional to the number of photons

$$SNR = \frac{n_p}{\sqrt{n_p}} \tag{3.10}$$

$$\therefore \quad SNR = \frac{Q_E \cdot n_p}{\sqrt{Q_E \cdot n_p + n_n^2}} \tag{3.11}$$

where Q_E is the fraction of detected photons and n_n is an additional sensor noise (Pawley, 1995).

Equation 3.11 suggests two interesting cases:

- $n_p >> 1$

$$SNR \simeq \sqrt{Q_E \cdot n_p}$$

  SNR is proportional to the square root of the number of photons n_p

- $n_p << 1$

$$SNR \simeq Q_E \cdot \frac{n_p}{n_n}$$

SNR is proportional to the ratio of the number of photons n_p to the sensor noise n_n

the information content, in bits, is give by

$$b = \log_2 (1 + SNR)$$

or in terms of discernible grey levels:

$$b = \log_2 (g)$$

it follows that

$$\begin{aligned} g &= 1 + SNR \\ &= 1 + \frac{Q_E \cdot n_p}{\sqrt{Q_E \cdot n_p + n_n^2}} \end{aligned}$$

In the case of $n_n \simeq 0$

$$g \simeq 1 + \sqrt{Q_E \cdot n_p} \tag{3.12}$$

Equation 3.12 implies that

(i) the decisive parameter that influences the quality of the image is the number of photons n_p that reach the PMT; and

(ii) noise in a confocal image is related to the number of photons that reach the PMT.

The uncertainty in the intensity distribution for a point of light varies with the square root of the number of photons detected, and so samples with weaker signal will always appear noisier than samples with stronger signals. To overcome this problem one has to allow more photons to reach the PMT. This can be achieved

either by increasing the dwell time (see Section 3.3.1 on page 31), or by repeating the experiment on several samples and taking their average (see Wilhelm *et al.* (2003)).

3.5 Chapter Summary

After summarising the sample preparation methodology, and the concept of confocal microscopy, this chapter concluded that the theoretical optical lateral and axial resolutions that can be reached, using leica TCS SP2, are limited, by diffraction, to around 200 nm and 300 nm respectively, meaning that structures smaller than these limiting values in size cannot be resolved; consequently ER tubules that are closer to each other than these limiting values will appear as single thicker tubules, which has to be taken in to consideration in the calculation step (see Chapter 7 and Chapter 8). Furthermore, it is known from Chapter 2 that cortical ER tubules are cylindrical with an average diameter of varying between 100 nm (Voeltz *et al.*, 2006), and 300 nm (Pierson *et al.*, 1990)); which means that the ER tubules can be better analysed laterally than axially(see Chapter 8).

The other concern this chapter has raised is the correct sampling frequency; meaning that the microscope analogue-to-digital converter has to generate enough pixels (voxels) per resolvable object to be able to represent the optically resolved image without any loss of information, and according to Nyquist theorem (at least two pixels per resolvable structure) the required size of a voxel, in this thesis experimental settings is **voxel(100nm, 100nm, 150nm)**.

This chapter has also discussed the formation of a 3D image of a GFP tagged ER sample, in CLSM, and has shown that it is formed in the following steps: (a) the ER is scanned, by a laser beam, with an appropriate wavelength, point-by-point, line-by-line, and focal plane by focal plane, (b) with the presence of a pinhole, the PMT detects the emitted light point by point, (c) an incorporated analogue-to-digital converter transforms each detected point into a pixel format, (d) a computer

stores the digital data for processing and analysis.

Lateral resolution controlling factors in CLSM reported by Leica (2000) are: the emission wavelength, numerical aperture of the objective, immersion medium, stability of the system, brightness/contrast-settings, and pixel size. The axial resolution depends on the pinhole size, the coverglass thickness, the immersion medium scanning speed and the bit resolution.

Finally, this chapter has concluded that even in the case of optically resolved structures, which have been optimally sampled, it is not possible to obtain noise free images. The most dominant noise, in CLSM, in the fluorescence mode is shot noise, a random noise generated in the PMT, which depends on the number of photons detected. The next Chapter addresses data processing.

4

Skeleton Extraction

As stated in Chapter 1, the methods presented in this thesis rely on the representation of the reticulum by its medial axis or skeleton, and use it as an anchor to which it associates key ER geometric and dynamic properties, and then relate them back to the original ER specimen. Skeletonisation plays, therefore, an essential role in the validity of the calculations in this thesis. Since most skeletonisation techniques are sensitive to noise, this chapter starts by describing different noise reduction techniques, then it reviews the main skeletonisation algorithms currently available in the literature, and finally it explains in details the methodology of the chosen skeleton extraction algorithm used to get the skeleton of the ER.

4.1 Introduction

We distinguish between (a) the ER as a surface separating the lumen from the cytosol and (b) the solid ER which includes also the lumen. Throughout the remainder of this thesis we use the term the skeleton to refer to the skeleton of the solid ER.

A curve-skeleton, also known as skeleton, is a 1D representation of a 2D (or a 3D) object. Typical skeleton applications include: virtual endoscopy (He *et al.*, 2001), computer animation (Wu *et al.*, 2006), collision detection (Li *et al.*, 2001), shape matching (Sundar *et al.*, 2003), shape registration, and shape retrieval (Au *et al.*, 2008), and surface reconstruction (Fol-Leymarie, 2003). Most of these applications involve the analysis of shape and/or movement of objects.

Most skeletons in the above applications share several properties, which according to Cornea & Min (2007) include: homotopy type (the homotopy type of the solid ER is the same as the homotopy type of the ER skeleton), thinness (the skeleton is one pixel/voxel wide), medialness (the skeleton occupies the medial axis of the image foreground), reversibility (the possibility of reconstructing the original 2D or 3D object from the skeleton), robustness (sensitivity to noise), computational efficiency (speed and accuracy), invariance under isometric transformations (the independence of which dimension is processed first), reliability, smoothness, component-wise differentiation, and hierarchy.

The properties mentioned above depend on the aim of the application, and may sometimes conflict each other; for example, it is not always feasible to obtain a skeleton that is thin and reversible at the same time. Therefore, it is necessary to choose the right algorithm, which meets the requirements specified by the application.

In order to exploit the skeleton of the solid ER in this thesis, it is essential to

select an algorithm which yields skeletons that are thin, medial and have the same homotopy type as the original solid ER. Thinness simplifies the entire analysis into a 1D problem rather than 3D. Medialness allows direct measurement of the solid ER tubules diameters using distance maps. Finally, the conservation of the homotopy type has the advantage of allowing the geometric and dynamic properties of the skeleton to be mapped to the corresponding solid ER.

4.2 Terminology

We follow the notation proposed by Kong & Rosenfeld (1989) and Pudney (1998), so we denote the *field* of real numbers, the *semiring* of natural numbers, and the *ring* of integers by $\mathbb{R}$, $\mathbb{N}$, and $\mathbb{Z}$ respectively.

In 2D, the neighbourhood of a point located at (x, y) is denoted by N_8 and consists of the set of points located at: $(x-1, y-1)$, $(x-1, y)$, $(x-1, y+1)$, $(x, y-1)$, $(x+1, y-1)$, $(x+1, y)$, $(x+1, y+1)$, and $(x, y+1)$

p_3	p_4	p_5
p_2	p	p_6
p_1	p_8	p_7

The neighbourhood

	p_4	
p_2	p	p_6
	p_8	

The 4-neighbours

The 4-neighbours of p, denoted $N_4(p)$, are the points located at: $(x-1, y)$, $(x+1, y)$, $(x, y-1)$, and $(x, y+1)$.

In 3D the neighbourhood of a point is denoted $N(p)$ and consists of 26 points located in three planes as illustrated bellow:

p_3	p_4	p_5
p_2	p_9	p_6
p_1	p_8	p_7

top plane

p_{12}	p_{13}	p_{14}
p_{11}	p	p_{15}
p_{10}	p_{17}	p_{16}

middle plane

p_{20}	p_{21}	p_{22}
p_{19}	p_{26}	p_{23}
p_{18}	p_{25}	p_{24}

bottom plane

Points are said to be 6-adjacent if they share a face, 18-adjacent if they share a face or an edge, and 26-adjacent if they share a face, an edge, or a vertex.
The 26-adjacent neighbours of a point p are denoted by: $N_{26}^* = \{p_i | i = 1, \ldots, 26\}$.
The 6-adjacent neighbours of p are defined as follows: $N_6^* = \{p_9, p_{11}, p_{13}, p_{15}, p_{17}, p_{26}\}$.
The 18-adjacent neighbours of p are:
$N_{18}^* = N_6^* \cup \{p_2, p_4, p_6, p_8, p_{10}, p_{12}, p_{14}, p_{16}, p_{19}, p_{21}, p_{23}, p_{25}\}$.

Let $m = 6$ or 18 or 26 if we are working in 3D and let $m = 4$ or 8 if we are working in 2D. By an m-path we mean a sequence of pixels so that each pixel is m-adjacent to the next pixel. Let $\mathcal{I}$ be a binary image; a subset S, $S \subseteq \mathcal{I}$, is said to be m-connected if any two points in S can be connected by an m-path (see Gonzalez & Woods (2008)). A point p is said to belong to the foreground if its intensity is 1, and it belongs to the background if its intensity is zero.

We express a 3D binary image $\mathcal{I}$ by the quadruple $(Z^3, m, n, \mathcal{F})$, where Z^3 is the 3D cubic lattice, in which the image elements (voxels) are arranged. Letter $\mathcal{F}$ refers to the foreground of image $\mathcal{I}$, and $\overline{\mathcal{F}}$ refers its background. The integers m and n denote the foreground and background connectivities respectively, $(m, n) = (26, 6)$. Analogously, for a 2D image, we use a quadruple $(Z^2, m, n, \mathcal{F})$ with $(m, n) = (8, 4)$.

We use the term point to denote an image element, and the coordinates (x, y) or (x, y, z) to its position in a 2D or 3D images respectively. We assume that $x, y, z \in \mathbb{N}$. We assume that exterior points are *6-adjacent* and interior points are *18-adjacent*. Figure 4.1 shows N_6, N_{18}, and N_{26} 3D neighbourhoods. The medial axis of an object, in 2D, is the locus of points that have at least two closest points on the boundary

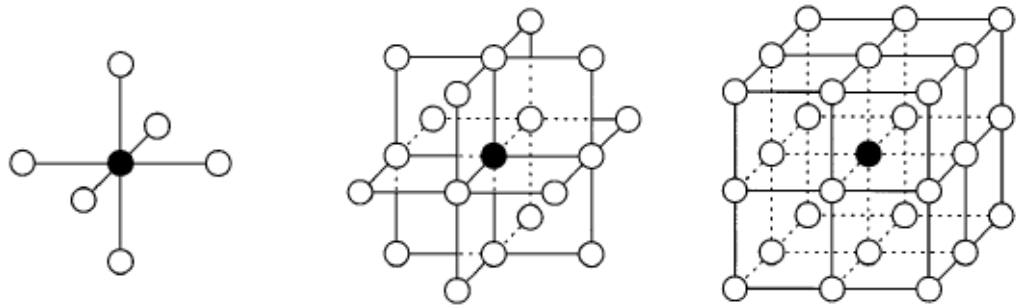

(a) (b) (c)

Figure 4.1: The neighbourhoods (white circles) (a) $N_6(p)$, (b) $N_{18}(p)$, and (c) $N_{26}(p)$ centred on a point p (black circle), figure adapted from Pudney (1998).

of the shape. The points in a medial axis which have one neighbour are called end points. In the 3D case, the corresponding object is called the medial surface because in addition to curves, it can also contain surface patches, see Cornea & Min (2007). We define the points which lie on the edges of a medial surface as edge points. To comply with the specifications dictated in Section 4.1 on page 54, this chapter formally defines the skeleton of the solid ER as follows:

Definition 4.2.1. The skeleton $\mathcal{S}$ of a solid ER specimen, with foreground $\mathcal{F}$, is a subset of $\mathcal{F}$, $\mathcal{S} \subset \mathcal{F}$, which satisfies the following three requirements:

(1) **Thinness** $\mathcal{S}$ is a 1D structure, i.e. 1 point wide.

(2) **Medialness** $\mathcal{S}$ occupies the centre of the foreground, i.e. its medial axis of $\mathcal{F}$.

(3) **Homotopy** $\mathcal{S}$ has the same homotopy type as the solid ER defined in Section 4.1 on page 54. If none of the branches of the solid ER in a ROI are very short and all junctions are 3-way junctions, the solid ER and the corresponding skele ton will have the same number of holes.

We define city block, Euclidean, and chess board metrics, as follows:

$$
\begin{aligned}
d_{Cityblock}(v,w) &= \sum_{i=1}^{n}|v_i - w_i| && \textit{City block metric, also known as } d_1 \\
d_{Euclid}(v,w) &= \sqrt{\sum_{i=1}^{n}(v_i - w_i)^2} && \textit{Euclidean metric, also known as } d_2 \\
d_{Chessboard} &= \max_{i=1\ldots n}\{|v_i - w_i|\} && \textit{Chess board metric, also known as } d_\infty
\end{aligned}
$$

see Gonzalez & Woods (2008);

4.3 Data pre-processing

Most skeleton extraction methods are sensitive to noise, and it is particularly important to take into account such an observation in the case of skeletons which are meant to preserve the homotopy type of the original objects. So it is often necessary to precede the skeletonisation process by a de-noising step.

Technically, noise is an unwanted false signal which accumulates throughout the optical chain of the confocal microscope during data acquisition. One of its misleading effects is that it may cause unresolved structures to appear as if they were resolved, and those resolved to appear as if they were unresolved. Modern confocal microscopes are normally optimised against most types of noise (especially periodic noise), see Section 3.4 on page 47. However, due to the stochastic nature of shot noise, it is not currently possible to build a confocal microscope that is optimised against such noise.

To reduce the impact of shot noise on the final results, it is therefore important to filter the data using an order statistics filter (OSF). Examples of OSF filters include: the linear average, the trimmed mean, and the median filters.

This thesis uses the median (because it preserves edges), and Sauvola filters (in

the case of adaptive thresholding) (see Chapter 7 and Chapter 8), and in order to obtain smooth skeletons this thesis uses the Gaussian filter. Finally, it is sometimes necessary to enhance the image by making hidden regions more visible (especially in situations where the signal appears to be non-uniform across the image).

4.3.1 Z-Drop correction

Despite the ability of confocal laser scanning microscopy to produce thin optical slices, that are less than $500nm$ thin, it is limited by the thickness of the specimen (it can only image specimens which are less than $100\mu m$ thick according to Wilhelm *et al.* (2003)). Furthermore, the intensity of the beam of laser travelling through the specimen weakens as the depth increases (due to light absorption), see Forero *et al.* (2006). Weak signals imply fewer photons have reached the confocal Photomultiplier tubes (see Section 3.3.1 on page 31), which means larger shot noise, and smaller Signal-to-Noise (SNR) values, see Section 3.4 on page 47 and Equation 3.11. This phenomenon is known as z-drop or intensity attenuation.

This thesis corrects for such weakness in the signal by fitting the following exponential curve, which is proposed in Zuse (2006),

$$f(u) = a \cdot e^{b \cdot s},$$

where $s \in [0, 1]$ refers to a confocal optical slice ($s = 0$ corresponds to the first slice, $s = 1$ to the last slice, $0 < s < 1$ to the slices in between, depending on the average intensities in each slice in a confocal stack), and $a, b \in \mathbb{R}$.

4.3.2 The median filter

This thesis applies the median filter prior to segmentation (or binarisation) to minimise the amount of shot noise present in an image for two reasons: (a) the median filter reduces noise while preserving edges (b) it considerably filters out noise with much less blurring than smoothing filters of the same kernel size.

In the case of 2D images, the median filter works by making points with distinct intensity values look like their neighbours. Dark or light (with respect to their neighbours) isolated clusters of pixels, whose area is less than $N^2/2$, are therefore forced to the median intensity of the neighbours (in other words all structures in the image that involve fewer than $N^2/2$ pixels will vanish, and that is why it is especially effective in removing salt-and-pepper noise).

Mathematically the median filter proceeds by ordering the pixels within a given part of an image, known as a kernel, of size $N \times N$ according to their grey values; then assigns the value of the median of the values of these pixels according to

$$\hat{f}(x, y) = median_{(s,t)\in S_{xy}} \{g(s, t)\}$$

to the centre pixel, see Gonzalez & Woods, 2008, chap. 3. Following the same logic it is possible to construct a 3D median filter by replacing the area $N^2/2$ by a volume $N^3/2$.

Implementation Note: The 3D median filter with a kernel of size $k_x \times k_y \times k_z$ in the case of an image $\mathcal{I}$, whose size is $w \times h \times d$, where $w, h, d \in \mathbb{N}$, is an $O(k_x \times k_y \times k_z)$ algorithm. So it is not practical (too computationally expensive) to consider kernels that are larger than 3 (in the isotropic case). Limiting median filters to kernel size 3 can be justified because using kernels with larger sizes removes larger structures which increases the possibility of removing genuine structures (structures that are not noise)

4.3.3 The Gaussian filter

To obtain smooth skeletons, this thesis usually follows the above median filtering by a smoothing operation by applying the Gaussian filter. This filter blurs an image by performing a convolution operation with a "bell-shaped" kernel, whose point spread function(PSF) takes the form of a Gaussian distribution:

$$\begin{aligned} G(x,y,z) &= G(x)\cdot G(y)\cdot G(z) \\ &= \frac{1}{\sqrt{2\pi\sigma_x^2}}e^{-\frac{x^2}{2\sigma_x^2}}\cdot\frac{1}{\sqrt{2\pi\sigma_y^2}}e^{-\frac{y^2}{2\sigma_y^2}}\cdot\frac{1}{\sqrt{2\pi\sigma_z^2}}e^{-\frac{(z-\mu_z)^2}{2\sigma_z^2}} \end{aligned}$$

Note that $G(x,y,z)$ is separable into three independent components $G(x)$, $G(y)$, and $G(z)$ which correspond to the PSF components in the x-, y-, and z- directions respectively. All of the three components depend on the mean and the standard deviation.

In the isotropic case where $\mu_x = \mu_y = \mu_z = \mu = 0$ and $\sigma_x = \sigma_y = \sigma_z = \sigma$ the expression reduces to

$$G(x,y,z) = \frac{1}{\sigma\times(2\pi)^{3/2}}e^{-\frac{x^2+y^2+z^2}{2\sigma^2}}$$

Now the images are ready for the next step, which is skeletonisation. The following section reviews the common techniques used to obtain object skeletons.

4.4 Binarisation

This thesis uses a skeletonisation method, which takes a binary image, and its corresponding distance map and outputs a skeleton in the form of a binary image, see Section 4.5.2 on page 70. So it is important to explain how this thesis obtains

a binary image. To obtain a binary image, assuming the image has already been denoised, the thesis follows two approaches: (a) a global approach where it sets the same threshold value to all points in the image, and (b) a local approach where it sets different thresholds values to different parts in the same image (this section uses the term adaptive thresholding to refer to local thresholding).

It follows from the above discussion that binarisation plays a crucial role in the validity of the results. This thesis defines the term binarisation, or thresholding, the process which takes a grey level image, assigns value 1 to all points, whose grey level intensity is greater than a certain threshold value, denoted $\mathcal{T}$, and value 0 to the remaining points:

$$\mathcal{I}(p) = \begin{cases} 1 & \text{if} \quad I(p) \geqslant \mathcal{T} \\ 0 & \text{if} \quad I(p) < \mathcal{T} \end{cases} \tag{4.1}$$

4.4.1 Global thresholding

Let us assume that the lowest and highest threshold values that produce an ER-like structure are $\mathcal{T}_l$, and $\mathcal{T}_h$ respectively. Let us also denote by $\mathcal{I}_l$, and $\mathcal{I}_h$ the resulting images obtained after applying these thresholds respectively. This thesis considers a range to be useful if both I_l, and I_h have exactly the same number of parts, the same number of junctions, the same number of branches, as well as the same number of loops, i.e. the same connectivity.

It follows that the correct threshold value must lie in the range $[\mathcal{T}_l, \mathcal{T}_h]$. Although not accurate, an approximate value of the threshold can be estimated in this range.

Very low threshold values produce melted objects, while very high threshold values produce fragmented objects (or skeletons), so to obtain a useable threshold value, which separates the foreground of an image from its background. The global approach varies the threshold value in a certain range and takes the average value.

4.4.2 Adaptive thresholding

This thesis uses the state of the art Sauvola local Adaptive thresholding technique, which treats the image as a set of connected regions (windows of size $w \times w$ centred around pixel p(x,y)), and associate a different threshold value to each one in turn taking into account the local mean $\mu(x, y)$ and local variance $\sigma^2(x, y)$ of the pixel(x,y) intensities (Shafait *et al.*, 2008):

$$T(x, y) = \mu(x, y) \times [1 + k \times (\frac{\sigma^2(x, y)}{R} - 1)], \tag{4.2}$$

where R is the maximum value of the standard deviation (128 in our case) and k is a parameter in the range $[0.2, 0.5]$. We set k = 0.34 according to Shafait *et al.* (2008).

There is a generalised mean local adaptive thresholding method, where only the mean is taken into account. This is a vital step to highlight details (holes), and avoid false edges (very close edges). It is important to note that the smaller the window size the more details one gets.

4.5 Skeleton extraction methods

The different methods to extract skeletons include: the continuous methods and the discrete methods. The former include the Voronoï, the partial differential equations approach, and the least squares method. The latter include: the thinning based methods, the distance map based methods, and the distance ordered homotopic thinning method (DOHT). In this work we choose to use the DOHT method because it yields skeletons that meet the three conditions in Definition 4.2.1 on page 57.

In this section we summarise these techniques and explain the DOHT method.

4.5.1 Continuous methods

Voronoï approach

Attali & Montanvert (1997)'s algorithm obtains the skeleton of an object by first selecting a set of representative contour points. It then constructs the Voronoï diagram of these points, and finally it discards all line segments that completely lie outside the object, see Figure 4.2 on page 65. A skeleton thus obtained is medial (this is an intrinsic property of Voronoï diagrams), thin (the intersection of the Voronoï cells are line segments in 2D and hypersurfaces in 3D), and homotopic (because it is based on the contour points of the object, which conserve its homotopy type), so it meets all three requirements of Definition 4.2.1 on page 57. The drawback of the Voronoï based approach lies in the complexity of its algorithm and the time of its execution (might be very high especially in the case of large 3D data).

Partial differential equations approach

Gomes & Faugeras (2000) uses the hypersurface of an object to extract its skeleton. Let $S(p,t) \in \mathbb{R}$ a hypersurface of an object, which evolves according to the following initial value partial differential equation (PDE) problem,

$$\begin{cases} \dfrac{\partial S(p,t)}{\partial t} &= \beta \cdot N \\ S(0) &= S_0, \end{cases} \tag{4.3}$$

where p parametrises the surface, t refers to the time, N is the inward unit normal vector of S, β is a velocity function, and S_0 is some initial closed surface.
Let S be implicitly defined by a function u as follows

$$\begin{aligned} u: \quad \mathbb{R}^3 \times \mathbb{R} &\rightarrow \mathbb{R} \\ u(S,t) &= 0 \quad \text{if } s \text{ is in the surface } S_t \end{aligned} \tag{4.4}$$

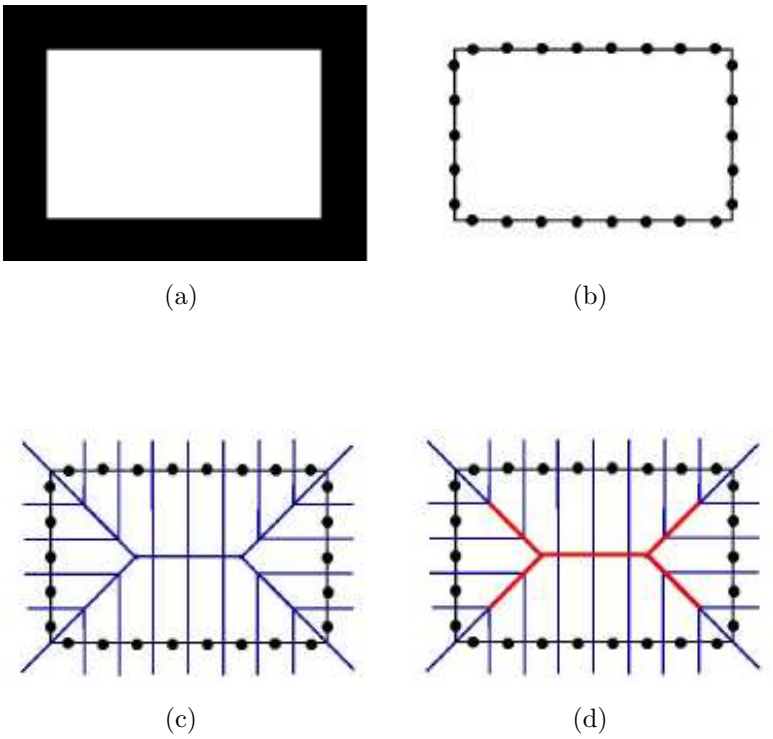

Figure 4.2: An illustration of the Voronoï based approach to calculate the skeleton of an image: (a) Input: a binary image, (b) **step 1:** selection of a set of contour points, (c) **step 2:** construction of the Voronoï diagram of the selected points, (d) **step 3:** the removal of line segments that lie, partially or completely, in the foreground give the skeleton of the input image, figure obtained from Fouard (2005).

Gomes & Faugeras's idea is to assume that, at each time instant, function u is the signed distance function to the solution S of Equation 4.3. To achieve this, the authors look for a function B

$$\begin{array}{rccc} B: & \mathbb{R}\times\mathbb{R}^{+} & \rightarrow & \mathbb{R} \\ & B(x,t) & = & \dfrac{\partial u}{\partial t} \end{array} \tag{4.5}$$

which satisfies two constraints: (a) $x \rightarrow u(x)$ is a distance function, and (b) the zero level set of u evolves according to Equation 4.3; using the characteristics properties they concluded that

$$\begin{cases} \dfrac{\partial u}{\partial t} & = & \beta(x - u\nabla u) \\ u(0,.) & = & u_0. \end{cases} \tag{4.6}$$

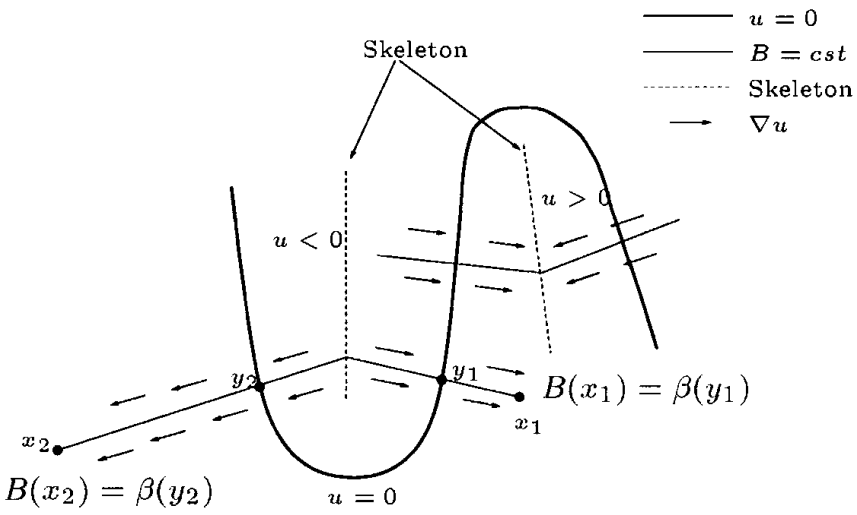

Figure 4.3: PDE based approach to extract a skeleton of a closed hypersurface: "The skeleton of the zero level set is the set of points where ∇u, in Equation 4.6 is not defined" (Gomes & Faugeras, 2000)

This can be used to obtain the corresponding skeleton of the object, by finding the points where ∇u is not defined, see Figure 4.3 on page 66 (Blum & Nagel, 1978). This method yields homotopic, thin, and centred skeletons; so it meets all three requirements of Definition 4.2.1 on page 57. The main problem with this method is that it relies on the initial condition ($S(0) = S_0$), which is not easy to implement.

Linear least squares approach

The method proposed in Au *et al.* (2008) obtains the skeleton by (a) first contracting its geometry into an almost planar skeletal shape using implicit Laplacian smoothing with global positional constraints, (b) second it converts the shape from the first step into a 1D skeleton using "*a connectivity surgery process*", which removes collapsed faces while it preserves the homotopy type of the object, (c) third it refines the medialness of the skeleton using induced skeleton-mesh mapping, details of the algorithm can be found in Au *et al.* (2008). ***This algorithm works directly on a mesh (faces and vertices), so it is not appropriate for the analysis of the data of this thesis.***

4.5.2 Discrete methods

Although the continuous methods discussed in the previous section meet the three requirements of a skeleton that can be used to study the solid ER (see Definition 4.2.1 on page 57), they are more suited to geometric data. Since this thesis uses discrete data (volumetric data), it is more convenient to look for alternative discrete methods.

There are two principal classes in this category of methods: (a) thinning-based methods, and (b) distance map-based methods.

These methods are based on removing points whose removal does not change the homotopy type of the original object. Bertrand & Malandain (1994) and Pudney (1998) use the term simple points to refer to such points. Bertrand & Malandain (1994) defines a simple point as follows:

Definition 4.5.1. Let p be a point in the foreground of a 3D binary image $\mathcal{I} = (Z^3, m, n, \mathcal{F})$, where $(m, n) = (6, 26)$, or $(m, n) = (26, 6)$, and let

$$N^* = \begin{cases} N_{18} & \text{if} \quad (m, n) = (6, 26) \\ N_{26} & \text{if} \quad (m, n) = (26, 6) \end{cases} \tag{4.7}$$

p is a simple point if and only if the following two conditions hold:

(i) p is m-adjacent to just one connected component of $N^* \cap \mathcal{F}$, and

(ii) p is n-adjacent to just one connected component of $N^* - \mathcal{F}$.

Thinning-based methods

This class of algorithms proceeds by removing simple points. The process stops as soon as it is not possible to remove points without affecting the original homotopy

type. Although they produce homotopic skeletons by construction, these methods do not always yield medial skeletons. Furthermore, medialness in such algorithms depends on the order in which simple points are removed, see Pudney (1998). There are two approaches to remove points from the foreground:

(i) an iterative approach, where points are removed one at a time, and the value of a point depends on its value in the previous iteration (see Palágyi *et al.* (2001)), and

(ii) a parallel approach, where a set of points are simultaneously removed in each iteration (see Palágyi & Kuba (1999) and Ma & Wan (2000)), and the value of each point depends on its neighbourhood.

Lohou & Bertrand (2004, 2005) have demonstrated that, despite its speed, ***the parallel point removal approach does not guarantee conservation of the homotopy type of the original object***, Figure 4.4 on page 68, and Figure 4.5 on page 69 are examples of where such cases might appear.

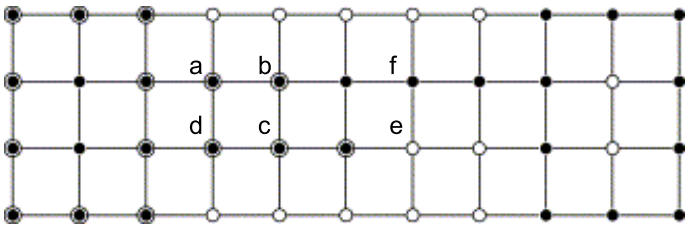

Figure 4.4: A 2D example showing how removing simple points (a, b, c, and d in this case) in parallel disconnects the object and creates a non-homotopic skeleton, all points similar to (e) represent the background and all points similar to (f) represent the foreground, Figure adapted from (Lohou & Bertrand, 2004).

Furthermore, Pudney (1998) reports that regardless of which point removal approach is followed, ***both removal strategies yield nonmedial skeletons***. For example when the width of a structure contains a even number of points it is not possible to obtain a medial skeleton.

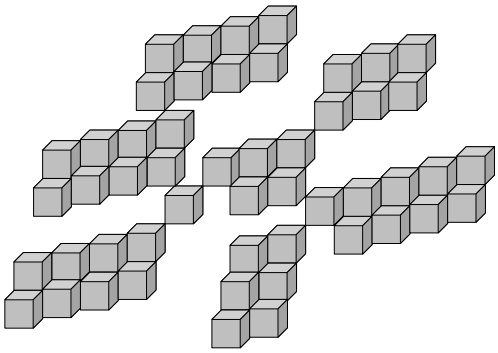

Figure 4.5: (b) A 3D example showing how removing simple points changes radically the homotopy type and shape properties of an object.

To solve the first problem in the previous paragraph, (Rosenfeld, 1975) systematically allows the removal of points in a well defined order: *North*, *South*, then in *East*, *West* directions successively. However, this solution only works in 2D images; so to extend it to 3D Tsao & Fu (1981), Gong & Bertrand (1990) and Palágyi & Kuba (1999) add sub-iteration strategies to guarantee the conservation of the homotopy type; while Lohou & Bertrand (2004) add additional constraints to the definition of simple points. More recently, Jonker (2000) uses mathematical morphology (erosion, opening, and closing in mathematical morphology terms) to obtain the skeleton of an object.

Distance map-based methods

In distance map based skeleton extraction methods, the skeleton of an object is formally defined as the loci of the local maxima of the object's distance map (see Calabi & Harnett (1968) and Malandain & Fernández-Vidal (1998), and they essentially extract the skeleton in two steps: (a) first they obtain the local maxima of the distance map, and because the result is not connected, (b) they connect these local maxima using neighbourhood configurations (Niblack *et al.*, 1992), or paths which connect these points (Zhou *et al.*, 1998). ***The drawback of these methods is that they do not always yield homotopic or thin skeletons.***

Distance Ordered Homotopic Thinning

Algorithm 1: Distance Ordered Homotopic Thinning

Input: A binary Image $\mathcal{I}$, with foreground $\mathcal{F} = \{p : I[p] = 1\}$, and a distance transform $\mathcal{D}$ of $\mathcal{I}$

Output: A skeleton $\mathcal{S}$, that is *a binary image*

```
1  Step 1: Arrangement of points according to their distance.;
2  Q = NewSortedQueue [the number of entries in D] ;
3  foreach image element p in I do
4      if p ∈ F then
5          get the distance of p to the background, D[p];
6          insert D[p] into Q;
7      end
8  end
9  Sort Q entries in ascending order;
10 Step 2: Distance Ordered thinning;
11 for d = 1 to maxDist do
12     while There are still points p ∈ Q[d] to be removed do
13         if (p is a simple point) ∧ (p is not an end point) then
14             I[p] = 0;
15             delete D[p] from Q.
16         end
17     end
18 end
```

The previous two sections have shown that both thinning-based and distance map-based methods do not meet the three requirements of a skeleton that can be used to quantify the geometry of the solid ER and analyse its movement. A third approach, called Distance Ordered Homotopic Thinning (DOHT), combines both approaches

to obtain skeletons that are homotopic, thin, and centred, see Saito & Toriwaki (1994) and Pudney (1998).

The key idea of the DOHT approach is summarised in Algorithm 1 on page 70. Since the order in which simple points are removed from the foreground affects the position of the final skeleton all that is needed is to adopt an ordering strategy which positions the skeleton at the centre of the object.

Pudney (1998); Saito & Toriwaki (1995) and Fouard *et al.* (2006) adopt a strategy which is based on distance maps. By processing the points according to their distance to the background in an ascending order, they sequentially prioritise removing points closer to the background than other points. Pudney (1998) and Fouard *et al.* (2006) add additional constraints to avoid removing medial edges/surfaces, and hence ensure medialness, see Algorithm 1 on page 70, and they exploit the idea of queues introduced earlier by Vincent (1991) to sort the points, and make the algorithm more efficient.

An efficient way of implementing DOHT consists of two loops (a) a preliminary loop, which sorts the foreground points according to their distance to the background, and (b) a main loop which sequentially thins the object while conserving its homotopy type. The details of the algorithm are summarised as follows (Algorithm 1 on page 70):

The first loop in Algorithm 1 on page 70, lines (2) to (8), creates a queue of image points and sorts them in ascending order, i.e. according to their distance to the background (smallest first); line (2) creates an empty queue $\mathcal{Q}$, lines (3) to (7) build the queue by inserting all foreground points in $\mathcal{Q}$, and finally line (8) sorts $\mathcal{Q}$ entries in ascending order.

The second loop, lines (10) to (17), removes simple points from the foreground; line (11) checks if there are still points to be removed, line (12) ensures that the

point p to be removed is simple, not an end point, and lies in the border (between the foreground and background), line (13) turns any point p, which meets the three conditions, into a background point, and line (14) deletes it from queue $\mathcal{Q}$. The next section explains the deletability of points to clarify line (12).

Point deletability

A crucial aspect of the above DOHT algorithm is how to determine whether a point p is deletable or not (line (12)). To achieve this it relies on two rules:

(A) p is deletable if it is simple and neither the end of a medial axis nor the edge of a medial surface.

(B) p is deletable if it is simple and not the centre of a maximum ball with a user defined-threshold.

The reason for keeping medial axis ends, and medial surfaces edges in Rule (A), is because, according to Definition 4.5.1 on page 67, they consist of simple points, and although they preserve the homotopy type of the object, their removal, in the case of open curves or/and open surfaces, may result in losing some of the shape characteristics of the object.

Surface edge points are points where there exists a plane, whose intersection with the surface of the object includes an open curve which ends at the edge point.
To obtain surface edges in a digital image, Pudney (1998) defines nine planes that pass through a point p and eight of its 26-neighbours, and then finds the set of points which have less than two foreground neighbours on any of these planes.

Niblack *et al.* (1992) defines the centre of a maximum ball as follows:

$$d(p) \neq d(q) - D(p,q) \;\forall\; q \in N_{26}, \tag{4.8}$$

where

$$D(p,q) = \begin{cases} n_1 & \text{if} \quad \| p-q \|^2 = 1 \\ n_2 & \text{if} \quad \| p-q \|^2 = 2 \\ n_3 & \text{if} \quad \| p-q \|^2 = 3, \end{cases} \tag{4.9}$$

and

$$d(p) = \begin{cases} \min_{q \in N_{26}} \{d(q) + D(p,q)\} & \text{if} \quad p \in \mathcal{F} \\ 0 & \text{if} \quad p \in \overline{\mathcal{F}}, \end{cases} \tag{4.10}$$

is the chamfer distance transform of image $\mathcal{I}$.

A point satisfying Equation 4.9 is said to be a *nonwitness*. Chamfer distances are used in order to be able to identify nonwitness points, using Niblack's criterion. Equation 4.9 $n_1, n_2, n_3 \in \mathbb{Z}$ are user defined. Borgefors (1984) and Pudney (1998) set $n_1 = 3$, $n_2 = 4$, and $n_3 = 5$, because they minimise the upper bound on the difference between the chamfer distance and the Euclidean distance. This was found to be $0.118 \cdot r$, where r is the maximum radius of the object.

DOHT algorithm proceeds in two stages: first it applies rule (B) in point deletability to preserve nonwitness points with distance values greater than a certain user defined value, and to ensure that the skeleton is thin, the algorithm applies rule (A) to thin the image.

4.6 Distance transforms

In addition to being an input parameter in the DOHT algorithm, distance transforms, sometimes referred to as distance maps, are exploited in this thesis to directly estimate key morphemic properties of the solid ER such as the local tubule diameter at a given point in the skeleton, as well as the surface area and volume of a tubule, see Chapter 7, and Chapter 8.

In principle, distance maps take a binary image as input, and they output a grey

level image, in which the value of each point in the foreground ($\mathcal{F}$) is equal to its distance to the nearest point in the background ($\overline{\mathcal{F}}$). A direct interpretation of this definition involves the calculation of the Euclidean distance between each point in the foreground $\mathcal{F}$ and all points in the background $\overline{\mathcal{F}}$, increasing the computational complexity to the order of the number of points in both sets.

The exorbitant cost of directly computing the Euclidean distance in such transforms led to the development of different approximation strategies, which rely on the local neighbourhood of a point to progressively propagate the distance across the image foreground, see Cuisenaire (1999) for a detailed review. The next section summarises the main methods used and categorises them into either (a) exact, or (b) approximate, depending on their computational complexity.

4.6.1 Exact Euclidean distance transformations

Exact Euclidean distance transform algorithms rely on neighbour point values to propagate distance through the image, and can be classified into either (a) sequential, where each point is processed in turn, and neighbour point values are taken from the previous iteration; or (b) parallel, where all points are processed at once, neighbour point values are taken from the original image, and the process is repeated till convergence.

Danielsson (1980) proposes a sequential algorithm (SED) which estimates the Euclidean distance by propagating $|p_0 - q_0|$, $|p_1 - q_1|$. It scans a 2D image four or eight times using "4-" , or a "8-" SED mappings mask (refer to Danielsson (1980) for more details). Using alternative masks, Ragnemalm (1993) reduces the number of scans to only three scans in a 3D image.

Yamada (1984)'s algorithm is a parallel version of Danielsson's, which combines the 8SED mask with a 3×3 mask and adds the mask values to $|p_0 - q_0|$, $|p_1 - q_1|$ of

each of the nine points covered by the mask, then selects the minimum value and assigns it to p; the process is iterated until convergence.

Shih & Mitchell (1992) uses mathematical morphology to achieve a distance transform approximation. This algorithm erodes the image with a large structuring element (as large as the maximum distance in the image), which it decomposes into smaller 3×3 elements for efficiency, see (Shih & Mitchell, 1992). An inherent problem with this algorithm is that the implementation of $k_{(2n+1)\times(2n+1)}$ elements, for instance, requires $n(n+1)/2$ grey scale erosions, which requires powerful specialised parallel pipelined circuits for efficient implementation (Cuisenaire, 1999). To overcome Shih & Mitchell (1992)'s algorithm problem, Huang & Mitchell (1994) evaluates d_2^2 (instead of d_2), reducing therefore the number of erosions to only n. Eggers (1996) extended Huang & Mitchell (1994)'s algorithm to include anisotropic and higher dimensions data.

The algorithm of Saito & Toriwaki (1994) calculates the squared Euclidean distance across the rows then across the columns and finally in the plane of the image giving the shortest path of a point to the background, and then calculates the Euclidean distance.

Breu *et al.* (1995) suggests the use of discrete Voronoï diagram to achieve the same aim. The idea is essentially based on selecting a set of points in the background; and obtain their discrete Voronoï diagram, which gives for each point in the foreground F the closest point in $\overline{\mathcal{F}}$.

4.6.2 Approximate distance transformations

Although exact Euclidean distance transformation algorithms discussed in the preceding section are fast and efficient, most of them require large computer memory. Because they process the whole image in each scan, parallel algorithms require a

spare memory of at least double the size of the input image (input image plus the results of each scan), which can be problematic especially in the case of very large data sets. Sequential algorithms are not usually well suited for subimage processing.

A simple and efficient alternative to the exact Euclidean distance transformation approach has been developed by Montanari (1968), and improved by Rosenfeld & Pfaltz (1966). This approach relies on chamfer coefficient to approximate the Euclidean distance by means of weighted integer distance propagation.

Definitions

The following definitions are based on Remy & Thiel (2000)'s work

Definition 4.6.1. Let S be a non-empty subset of $\mathbb{R}^\star$, and let F be a subset in $\mathbb{R}$, $F \subseteq \mathbb{R}$. A **distance** on S, with values in F, using metric M, denoted (d_M, S, F) is a mapping

$$\begin{array}{rccc} d_M: & S \times S & \rightarrow & \mathbb{R} \\ & (v, w) & \mapsto & d_M(v, w) \end{array}$$

which satisfies the following conditions:

(1)	$\forall\ v, w \in S$	$d_M(v, w) \geq 0$	*Positivity*
(2)	$\forall\ v, w \in S$	$d_M(v, w) = 0 \Leftrightarrow v = w$	*Identity Element*
(3)	$\forall\ v, w \in S$	$d_M(v, w) = d_M(w, v)$	*Commutativity*
(4)	$\forall\ u, v, w \in S$	$d_M(u, w) \leqslant d_M(u, v) + d_M(v, w)$	*Triangle inequality*

Definition 4.6.1 on page 76 is generic, so it can be applied in n-dimensional space both in continuous and discrete cases. A more specific definition that applies to mainly digital data can be deduced by replacing both sets, S and F, in Definition 4.6.1 by $\mathbb{Z}$, i.e.:

Definition 4.6.2. A distance $(d_{M,disc}, \mathbb{Z}, \mathbb{Z})$ is said to be **discrete** if it maps any

pair of integers $(v, w) \in \mathbb{Z}^2$ into an integer $d_M(v, w) \in \mathbb{N}$

$$\begin{array}{rccl} d_M: & \mathbb{Z} \times \mathbb{Z} & \rightarrow & \mathbb{N} \\ & (v, w) & \mapsto & d_M(v, w) \end{array}$$

While d_1 and d_∞ meet the requirements of a discrete distance in Definition 4.6.2 on page 76; d_2 does not, because $\exists\, v(0,0,0), w(2,2,2) \in \mathbb{Z}$, such that $d_2(v, w) \notin \mathbb{Z}$.
A norm is a concept that is related to distance and is usually defined in a vector space, which requires its scalars to lie in a *field*, $\mathbb{R}$ or $\mathbb{C}$. A module, however, allows the coefficients to lie in any arbitrary *ring* such as $\mathbb{Z}^n$, where $n \in \mathbb{N}$, so is more appropriate to discrete data.

Definition 4.6.3. Let $\mathcal{I}$ be a binary image, $\mathcal{I} = \{p \in Z : \mathcal{I}(v) \in \{0, 1\}\}$, and let $\mathcal{F}$ be its foreground; the distance transform, D_T, of image $\mathcal{I}$ is an mapping which maps each point in F to its distance to the nearest point in $\overline{\mathcal{F}}$

$$\begin{array}{rccl} D_T: & Z & \rightarrow & \mathbb{R} \\ & p & \mapsto & D_T(p) = \min\left\{d_M(p, q) : q \in \overline{\mathcal{F}}\right\} \end{array}$$

Chamfer maps

Chamfer maps are distance transforms which are used in order to be able to identify nonwitness points, using Niblack's criterion (see Section 4.5.2 on page 72). Pudney (1998) recursively obtains the distance map of a 3D binary image, as follows:

$$d(p) = \begin{cases} \min_{q \in N_{26}} \{d(q) + D(p, q)\} & \text{if} \quad p \in \mathcal{F} \\ 0 & \text{if} \quad p \in \overline{\mathcal{F}}, \end{cases} \tag{4.11}$$

Using local displacements (or chamfer masks), Borgefors's algorithm propagates local integer distances in parallel (meaning processing sets of points at the same time in each iteration) as follows: (a) first it initialises the image background points to 0, and foreground points to a very large number (denoted ∞), (b) the algorithm then

displaces a chamfer mask (see Figure 4.6: parallel mask on page 78) across the image, while assigning to each point in the foreground the minimum value between: (i) its value in the previous iteration, and (ii) the values obtained by adding the weights in the chamfer mask to the corresponding points in the image, (c) the algorithm repeats the same process till each point gets its previous value (convergence), see Figure 4.6 on page 78.

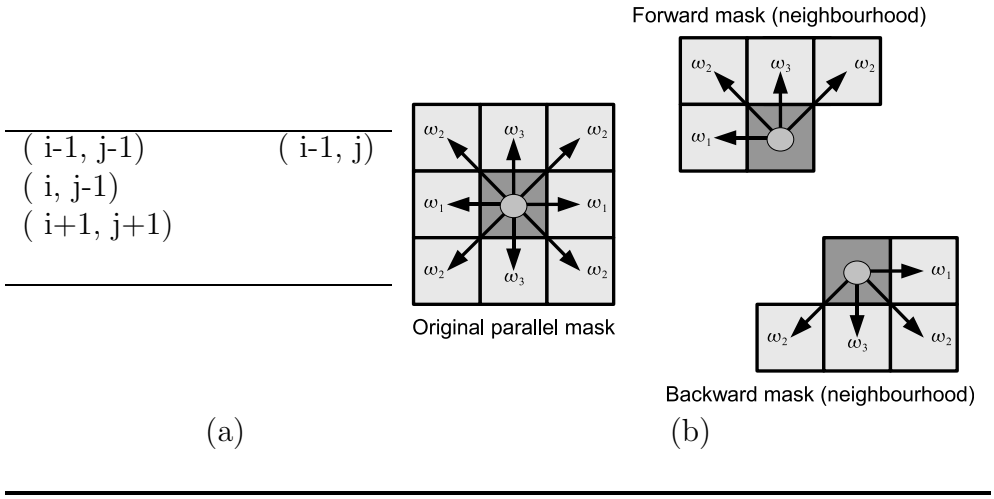

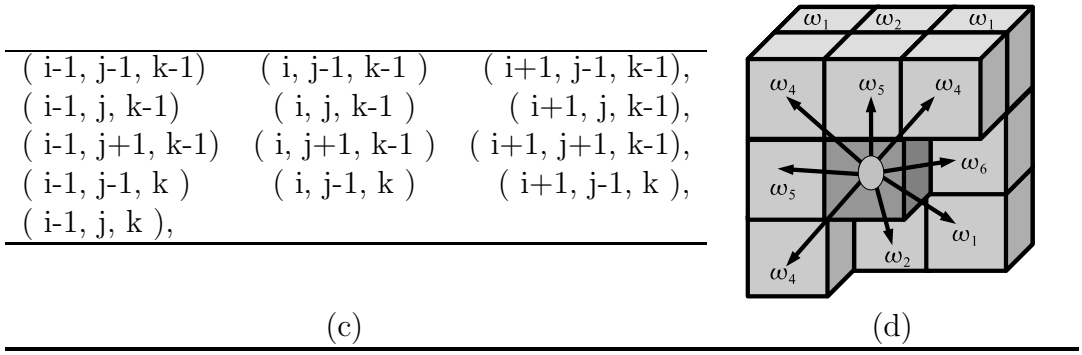

Figure 4.6: Chamfer mask: (a) the positions of the 2D 3×3 forward mask weights (b) the 2D chamfer masks (c) the positions of the 3D $3 \times 3 \times 3$ forward mask weights, (d) the 3D $3 \times 3 \times 3$ forward mask

4.6.3 Chamfer masks

Algorithm 2: Chamfer map

Input: A set of confocal z-stacks of the plant ER

We assume that the size of the data in the x, y and z directions to be I_x, I_y, I_z respectively.

Output: Distance map ER images

Forward scan;
for $z = 0$ *to* $\mathcal{I}_z - 1$ **do**
  for $y = 0$ *to* $\mathcal{I}_y - 1$ **do**
    for $x = 0$ *to* $\mathcal{I}_x - 1$ **do**
      $\mathcal{I}(p(x,y,z)) = \min(\mathcal{I}(p), \min_{\mathbf{v_k} \in \mathcal{M}_C^{forward}}(I(p + \mathbf{v_k}) + w_k))$;
    end
  end
end
Backward scan;
for $z = \mathcal{I}_z - 1$ *to* 0 **do**
  for $y = \mathcal{I}_y - 1$ *to* 0 **do**
    for $x = \mathcal{I}_x - 1$ *to* 0 **do**
      $\mathcal{I}(p(x,y,z)) = \min(\mathcal{I}(p), \min_{\mathbf{v_k} \in \mathcal{M}_C^{backward}}(\mathcal{I}(p + \mathbf{v_k}) + w_k))$;
    end
  end
end

Rosenfeld & Pfaltz (1966) sequentially achieves the same result, in 2D, in two scans using two symmetric masks (chamfer masks), such as the ones in Figure 4.6 on page 78. In the case of this mask there are three weights denoted ω_1,ω_2, and ω_3. After initialising the image, i.e. after assigning 0 to all points in the background and 1 to those in the foreground, Rosenfeld & Pfaltz's algorithm performs two scan

(Algorithm 2 on page 79):

(i) ***A forward scan (top left to bottom right):*** Starting at the top left point in the image, the forward scan operates as follows: (a) the algorithm assigns to each point in the forward neighbourhood the sum of its value in the current iteration and its corresponding weight (note that all those points have already been processed since the image is processed from the top-left to the bottom right), (b) then it compares the new values of all forward neighbourhood points with that of the centre point, and finally (c) it assigns the minimum value to the centre point.

(ii) ***A backward scan (bottom right to top left):*** Using the result of the forward scan as the initial image, the backward scan follows the same logic, but in the reverse order, i.e. starting at the bottom right point of the image and using the backward neighbourhood.

Figure 4.6 on page 78 shows examples of chamfer masks in 2D and 3D.

The following is a formal definition of chamfer masks (Fouard, 2005)

Definition 4.6.4. Let (E, A) be a module, where $E = \mathbb{Z}^3$ is the abelian group and A is the ring, and let F be a subgroup of $\mathbb{R}$. A chamfer mask $\mathcal{M}_c$ with weights $w = (w_k)$ is a finite set of vectors

$$\mathcal{M}_C = \{(\mathbf{v_k}, w_k) \in E \times F, 1 \leqslant k \leqslant m\}$$

which have at least one base in E, and which meets the following requirements:

(1) $\forall\ k \in E \qquad w_k > 0$ and $\mathbf{v_k} \neq 0$

(2) $\forall\ (\mathbf{v}, w) \in \mathcal{M}_c \quad ((\pm v_i), w) \in \mathcal{M}_c$ where $\boldsymbol{v} = (v_i)$.

The shortest path between a point in the foreground and the background (known as chamfer distance), provides an approximation of its Euclidean distance. The path

between a point p in the foreground and a point q in the background is a linear combination of chamfer vectors and is defined as follows:

Definition 4.6.5. Let $\mathcal{M}_C$ be a chamfer mask, and let $p, q \in E$, **a path** from p to q is the sum of vectors $\mathbf{v}_k \in \mathcal{M}_C$ starting at p, and ending at q,

$$\mathcal{P}_{pq} \quad = \quad \sum_{\mathbf{v}_k \in \mathcal{M}_C} \lambda_k \mathbf{v}_k \text{ where } \lambda_k \in \mathbb{R} \text{ and } \lambda_k \geqslant 0; \ \forall \ k$$

The **cost associated to path** $\mathcal{P}_{pq}$ is given by

$$W(\mathcal{P}_{p,q}) = \sum_{k=1}^{m} \lambda_k \cdot \omega_k.$$

Definition 4.6.6. Let p and q two points in E, **the chamfer distance** d_C between p and q is the minimum cost associated to all paths between p and q

$$d_C \quad = \quad \min_{\mathcal{P}_{pq}} W(\mathcal{P}_{p,q}).$$

Given a module (E, A), a chamfer mask $\mathcal{M}_C \in C(E, A, F)$, and a subgroup in R, Verwer (1991) shows that d_C is a distance in E

Proposition 4.6.7. Let (E, A) be a module, and let F be a subgroup of $\mathbb{R}$. If $\mathcal{M}_C \in C(E, A, F)$ is a mask, then the corresponding chamfer distance d_C is a distance in E.

Details and theory of distance maps have been formulated and thoroughly investigated in Bertrand & Malandain (1994); Cuisenaire (1999); Kong & Rosenfeld (1989); Malandain *et al.* (1993); Rosenfeld (1975); Rosenfeld & Pfaltz (1966), and the most important aspect of them from the point of view of this thesis is their error with respect to the Euclidean distance; ***Fouard* et al. *(2006) reports that with a*** $3 \times 3 \times 3$ ***mask, the maximum error between chamfer maps and***

the euclidean distance is 6.5% and the number of operations required to achieve this approximation amounts to 13 per voxel. With a $5 \times 5 \times 5$ ***mask, the maximum error is 2.5% and the number of operations per voxel is 37. Finally with a*** $7 \times 7 \times 7$ ***mask, the maximum error is around 2.0% with 97 operations on each voxel. This means that if the diameter of the solid ER is around a 200*** nm ***then the maximum error in the measurement of the diameter is around 13*** nm ***which is well below the confocal resolution power (see Chapter 3.)***

4.7 Chapter Summary

This chapter has shown that denoising the images of the solid ER requires two basic filters; the median filter to remove salt-and pepper noise and close tiny holes, and the Gaussian filter to obtain smooth skeletons. It has also explained the two approaches to binarise the image: (a) the global approach where the same useable threshold value, chosen from a range of useable thresholds, is applied to whole image, and (b) the adaptive approach where the image is split into smaller regions and the local threshold value is calculated on basis of the mean and standard deviation of the pixels with that region. It has also shown that the Distance Ordered Homotopic Thinning algorithm yields thin, medial, homotopic skeletons that conserve the homotopy type of the original shape, and concluded that it is best used with chamfer maps because they can rapidly be computed and offer good approximation to the euclidean distance and can be rapidly computed.

5

Motion Analysis

Chapter 4 has reviewed the different skeleton extraction methods that are currently used, both in the case of continuous as well as discrete data. It has concluded that distance ordered homotopic thinning technique offers a good trade-off between cost and accuracy. This technique yields thin, homotopic, and medial skeletons, that can be used to quantify the ER. This chapter uses a simplified version of the feature point tracking and trajectory analysis for video imaging algorithm developed by Sbalzarini & Koumoutsakos (2005). We use this algorithm to track, analyse, and quantify the movement of the solid ER based on the reconstruction of its skeleton.

5.1 Introduction

We observe the motion of the solid ER using Leica TCS SP2 (or SP5) confocal microscope (see Section 3.2 on page 29), which generates a series of digital images called a movie, at discrete time steps (called frames). Following the skeletonisation algorithm in Chapter 4, we transform this series of confocal images into a series of binary skeletons, from which we remove interior points to obtain a simplified graph representation of the specimen, where the vertices are geometric, i.e. they occupy the same spatial positions as the central points of the solid ER junctions (see Figure 5.1 on page 84).

To track the positions of the skeleton vertices, we use Crocker & Grier (1996)'s algorithm, and then exploit the improvements introduced by Sbalzarini & Koumoutsakos (2005), and hence follow the notation adopted therein. We refer to the images of the vertices as feature points (or simply points). Crocker & Grier 's algorithm consists of two main steps: (a) point detection, and (b) trajectory reconstruction. The former is essentially the identification of the moving points in all frames, and the latter is the linking of their locations in different frames to build their trajectories. The term *false detection* refers to the case where we detect a point where there is none, and the term *spurious detection* refers to the case where we correctly detect

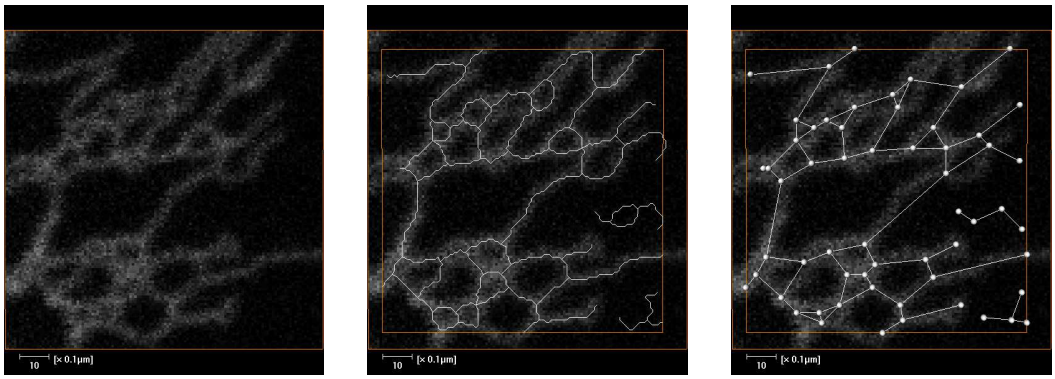

(a) Raw image (b) Skeleton (c) A geometric graph

Figure 5.1: An illustration of tracking the solid ER junctions. Scale bar $1.0\mu m$

a point where there is no particle of its kind in the real image. The term *false link* occurs when the algorithm links two points that do not represent the same vertex. Finally we call a trajectory *incomplete* if it lasts less than the image sequence.

5.2 Point tracking algorithm

There are two types of single point tracking algorithms: (a) the first type independently estimates the positions of the particle in each frame in a movie, and includes two algorithms, the center-of-mass algorithm, and the direct fitting of Gaussian curves to the intensity profiles; (b) the second type of algorithm compares the current and previous images to estimate the change in the position of a particle, and includes the cross-correlation and SAD algorithms. Both types of algorithms were reviewed and classified in in Yilmaz *et al.* (2006).

In the case of the solid ER, the type of motion is not known, a motion that seems to have a stochastic character whose trajectories entail several modes of motion (sudden, smooth, non-smooth parts etc.), which makes the tracking task more difficult due to the absence of a suitable mathematical model. Furthermore, we only require the two-dimensional case since the motion is mainly two-dimensional and is observed using two-dimensional confocal microscopy. On the basis of these observations we choose to use Crocker & Grier (1996)'s algorithm. This algorithm was later improved by Sbalzarini & Koumoutsakos (2005) to take into account several time steps in the linking stage.

The aim of tracking is to follow graph vertices as they travel with time, and analyse their motion in discrete trajectories in order to record the variations of their geometric parameters such as length and surface area, and measure their dynamic parameters, such as velocity and acceleration.

Because we used Crocker & Grier (1996)'s algorithm and exploited the improvements introduced by Sbalzarini & Koumoutsakos (2005), we refer to this algorithm as the original algorithm throughout the remainder of this chapter.

The original algorithm would start by calculating the global minimum I_{min} and the global maximum I_{max} of all intensity values in the entire movie in order to preserve intensity variations across frames by normalising pixel intensity values using the expression

$$\frac{I - I_{min}}{I_{max} - I_{min}};$$

The next steps in the original algorithm consist of the following: (a) image restoration, (b) point location estimation, (c) point location refinement, and (d) non-vertex discrimination. ***We represent the image at time*** t ***by an integer matrix*** $I^t(x, y)$ ***of point intensity values, where each point's intensity takes the value of either 0 or 1***. The integer coordinates $x = 1, \cdots, N_x$, and $y = 1, \cdots, N_y$ represent the pixel row and the pixel column indices respectively. N_x, N_y refer to the size of the image in the x and y directions respectively.

5.2.1 Image restoration

The image restoration step's main goal is to correct for imperfections in the image, by compensating against: (1) long-wavelength modulations of the background intensity due to non-uniform sensitivity among the camera pixels or uneven illumination, and (2) discretisation noise from the digital camera.

Background removal Assuming that the feature points are small compared to background fluctuations, i.e. well separated in spatial frequency, the algorithm

removes the background by a $2w+1$ pixel width boxcar average:

$$I_w^t(x,y) = \frac{1}{(2w+1)^2} \sum_{i=-w}^{w} \sum_{j=-w}^{w} I^t(x+i, y+j), \tag{5.1}$$

where $w \in \mathbb{N}$ is an integer larger than the apparent radius of a point and smaller than the smallest inter-point separation (in pixels).

The advantage of using graphs instead of the original network is that the background is already separated from the foreground. In addition, we can control the radii of the points to be detected.

De-noising filter The algorithm models the camera's discretisation noise as uniformly Gaussian with a correlation length of $\lambda_n = 1$, where n refers to noise. The denoising filter thus consists of convolving the image with a Gaussian of half width $\lambda_n = 1$:

$$I_{\lambda_n}^t(x,y) = \frac{1}{B} \sum_{i=-w}^{w} \sum_{j=-w}^{w} I^t(x+i, y+j) e^{\left(-\frac{i^2+j^2}{4\lambda_n^2}\right)}, \tag{5.2}$$

where

$$B = \left(\sum_{i=-w}^{w} e^{\left(-\frac{i^2}{4\lambda_n^2}\right)} \right)^2. \tag{5.3}$$

Subtracting Equation 5.1 from Equation 5.2 (Image - noise - background) yields the filtered foreground:

$$K(i,j) = \frac{1}{K_0} \left(\frac{1}{B} e^{\left(-\frac{i^2+j^2}{4\lambda_n^2}\right)} - \frac{1}{(2w+1)^2} \right), \tag{5.4}$$

where the normalisation constant K_0 is

$$K_0 = \frac{1}{B}\left(\sum_{i=-w}^{w} e^{-\frac{i^2}{2\lambda_n^2}}\right)^2 - \frac{B}{(2w+1)^2}, \tag{5.5}$$

and therefore the filtered image after restoration is given by:

$$I_f^t(x,y) = \sum_{i=-w}^{w}\sum_{j=-w}^{w} I^t(x-i, y-j)\cdot K(i,j), \tag{5.6}$$

In order to convolve the image with kernel K, the algorithm pads the image to $(N_x + 2w) \times (N_y + 2w)$ by repeating the first and last row and column. It also assigns value 0 to negative pixel values generated by the convolution. They are an artefact of the approximation of the camera noise by a Gaussian distribution, which breaks down at small intensity levels.

5.2.2 Estimating point locations

Let us assume that we detected a point p in frame t and we want to estimate its location in frame $t+1$. The original algorithm searches for local intensity maxima in the filtered image within a certain distance from p. It then takes the brightest pixel whose intensity value lies in the upper r^{th} percentile of the intensity values of the current frame. The algorithm calculates the intensity percentiles on a "*per frame basis*" and determines the local maximum using greyscale dilation (Gonzalez & Woods, 2008). It then finds the pixels that have the same intensity values before and after the dilation. Finally it selects all pixels that lie in the upper r^{th} percentile as candidate locations of point p.

Since our images are binary images we have neither non-specific signals, nor dust, nor particle aggregates, and so a point p_t ***in the current***

frame is taken as an approximate location of a point p_{t-1} ***in the previous frame if it is the only point present within a distance*** d ***from*** p_{t-1}

Because determining local maxima does not take into account noise, and may include spurious detections (bright background points or point aggregates), the original algorithm follows this step by a location refinement and a subsequent non-particle discrimination step.

5.2.3 Refining point locations

The aim of this step is to reduce the standard deviation of the position measurement, by assuming that the estimated new position $(\hat{x}_p, \hat{y}_p)$ is in the vicinity of the true geometric centre (x_p, y_p) given by the distance to the brightness-weighted centroid in the filtered image (see Crocker & Grier (1996); Sbalzarini & Koumoutsakos (2005)):

$$\begin{bmatrix} \epsilon_x(p) \\ \epsilon_y(p) \end{bmatrix} = \frac{1}{m_0(p)} \sum_{i^2+j^2 \leqslant w^2} \begin{bmatrix} i \\ j \end{bmatrix} I_f^t(\hat{x}_p + i, \hat{y}_p + j), \tag{5.7}$$

where

$$m_0(p) = \sum_{i^2+j^2 \leqslant w^2} I_f^t(\hat{x}_p + i, \hat{y}_p + j), \tag{5.8}$$

is the intensity moment of order 0 and the location estimation is refined as:

$$(\tilde{x}_p, \tilde{y}_p) = (\hat{x}_p + \epsilon_x(p), \hat{y}_p + \epsilon_y(p)) \tag{5.9}$$

if $|\epsilon_x(p)|$ or $|\epsilon_y(p)|$ is larger than 0.5 pixel, the candidate location $(\hat{x}_p, \hat{y}_p)$ is accordingly moved by one pixel and the refinement re-calculated.

5.2.4 Non-particle discrimination

We define the intensity moment of order 2 by the equation:

$$m_2(p) = \frac{1}{m_0(p)} \sum_{i^2+j^2 \leqslant w^2} (i^2 + j^2) I_f^t(\hat{x}_p + i, \hat{y}_p + j) \tag{5.10}$$

The original algorithm discriminates non-particles by assuming that the correctly detected points correspond to points which form a cluster in the $(m_0, m_2) - plane$ which follow a 2D Gaussian distribution given by:

$$P_p(m_0, m_2) = \frac{1}{2\pi\sigma_0\sigma_2 N_t} \exp\left(-\frac{(m_0 - m_0(p))^2}{2\sigma_0} - \frac{(m_2 - m_2(p))^2}{2\sigma_2}\right) \tag{5.11}$$

where $\sigma_0 = 0.11$ and $\sigma_2 = 0.1$ are the standard deviations and N_t the total number of detected points in the current frame. The contributions of all other points $q \neq p$ are summed for each point p at its location, giving a score

$$S_p = \sum_{q \neq p} P_q(m_0(p), m_2(p))$$

Every point detection having a score S_p above a certain user-provided threshold T_s (2 in our case) is considered as an observation of a true particle, all others are discarded.

5.2.5 Trajectory linking

Given a total set of T matrices C' with rows $[x_p, y_p]$ representing vertices detected in frame (t), we want to identify points that correspond to the same vertex in subsequent frames and link their positions.

The time evolution of the positions (their trajectories) is given by:

$$\rho(\mathbf{r}, t) = \sum_{i=1}^{N} \delta(\mathbf{r} - \mathbf{r}_i(t))$$

where $\mathbf{r}_i(t)$ is the location of the node i at time t. A reconstructed digital trajectory consist of an ordered series of point locations over time.

Linking the positions of these points means finding a set of associations between the point location matrices in different frames. This can be achieved by minimising a certain cost functional. The algorithm chosen to achieve this was implemented by Sbalzarini & Koumoutsakos (2005) and is based on the particle matching algorithm of Dalziel (1992) and Dalziel (1993), which uses the Graph theory technique introduced by Hitchcock (1941). We also include additional constraints to take into account physiological constraints (for example the connectivity of the network), concluded from our experimental observations.

Starting from frame t, in which there are N_t detected vertices which, denoted by p_i where $i = 1, ...N_t$, and considering R future frames, for all sets Ł$_r$. $r = 1, ..., R$ of points q_j where $j = 1, ..., N_{t+r}$, in frame $t + r$, the algorithm defines an association matrix G_r^t as follows:

$$G_r^t = g_{ij} = \begin{cases} 1 & \text{if } p_i \text{ in frame } t \text{ and } q_j \text{ in frame } t + r \\ & \text{are produced by the same vertex} \\ 0 & \text{otherwise,} \end{cases}$$

We assume that there is always exactly one physical particle producing a single point detection. This is a limiting assumption since particles could coalesce or come so close that they are indistinguishable by the used imaging equipment, giving raise to one single point observation.

To allow the number of points to vary between frames, every association matrix is augmented with both a row g_{0j} and a column g_{i0} for dummy particles at times t and t + r, respectively. Linking a point to the dummy means that the corresponding particle disappeared from the observed part of the scene between frames t and t + r, and linking the dummy to a point means that the corresponding particle newly appeared. This leads to the following topology constraint on the matrices: Every row $i > 0$ of G_r^t and every column $j > 0$ of G_r^t must contain exactly one entry of value 1, all others are 0. Row 0 and column 0 are allowed to contain more than one entry of value 1.

To find an optimal set of links g_{ij}, the algorithm uses a linear association of variables g to define a cost functional to be minimized. To be able to use the efficient solution algorithm based on the transportation problem this functional needs to be linear in the association variables g_{ij} and may thus be written as follows:

$$\Phi = \sum_{0}^{N_t} \sum_{j=0}^{j=N_{t+r}} \Phi_{ij} g_{ij}, \tag{5.12}$$

We define Φ_{ij} in terms of the quadratic distance between $p_i, i > 0$, and $q_j, j > 0$, as well as the quadratic differences in the intensity moments of order 0 and 2 as follows:

$$\Phi_{ij} = (\tilde{x}_{p_i} - \tilde{x}_{q_j})^2 + (\tilde{y}_{p_i} - \tilde{y}_{q_j})^2 + (m_0(p_i) - m_0(q_j))^2 + (m_2(p_i) - m_2(q_j))^2$$

for $i, j > 0$. The cost of linking a point to one of the dummy particles $i = 0$ or $j = 0$ is set equal to: $\Phi_{0j} = (rL)^2$ and $\Phi_{i0} = (rL)^2$. This places a limit to the allowed cost for point associations since no association of cost larger than $(rL)^2$ will occur between regular points because the dummy association would be more favourable. The parameter $L = 3$ is specified by the user and represents the maximum distance a point is allowed to travel between two subsequent frames when its intensity moments

remain constant. To speed up the linking process, all costs $\Phi_{ij} : \Phi_{ij} > 0$ are set to ∞.

5.3 Chapter Summary

Most of the feature point tracking algorithms rely on a priori knowledge to accurately reconstruct the trajectories of moving objects. Even so most of them are computationally intense, which prohibits tracking of long video sequences. Since the motion of the solid ER is not known, this thesis uses the algorithm of Crocker & Grier (1996) and Sbalzarini & Koumoutsakos (2005), because it does not assume any a priori knowledge about the physics of the problem to construct effective and robust feature point tracking procedures. The use of the graph representation simplifies the algorithm further by using binary rather than grey level images on the one hand and by controlling the size of the points to be tracked on the other hand. Furthermore, we only require the two-dimensional case since the motion is mainly two-dimensional and is observed using two-dimensional confocal microscopy.

6

Data Abstraction

So far we know the origin of the data, how it was processed, how to extract skeletons of the solid ER from isosurfaces (obtained using the commercial software Amira) and how to track moving solid ER junctions in a confocal time series. The next step in the methodology is quantification. The aim of this chapter is to explain how to combine 3D reconstruction and skeletonisation to characterise static and dynamic solid ER samples, together with a short review about graph theory to associate basic geometric quantities to such a skeleton.

6.1 Introduction

The ER has the most complex geometry in the secretory pathway (see Chapter 2). Investigating its shape is not a straightforward task, especially when addressing problems such as surface area, local diameter, and volume. This chapter simplifies this problem by a 1D representation of the solid ER as described in Section 4.1 on page 54. It explains how using its skeleton, extracted in Chapter 4, one can reduce a complex 3D problem to a simple 1D one. The basic geometric properties such as the length, surface area, and volume of a branch, are what characterise the solid ER in a certain physiological condition. The following sections assume that data have already been processed, 3D reconstructed, and their triangulations obtained and skeletons extracted. These sections demonstrate how to approximate the above geometric properties using skeletons, isosurfaces and triangulations.

We consider the solid ER network as a set of connected branches, and represent each branch by its homotopic skeleton (central line), see Chapter 4. It is possible to characterise the skeleton by representing each edge by its skeleton which is made of a set of connected points. Consecutive points in a branch are connected by a line segment. There are two types of points in an edge: inner and end points. The former are those which have exactly two neighbours, whereas the latter have either a single neighbour or three (or more) neighbours. Consecutive points are connected by segments. A branch of the solid ER network is characterised by its length, surface area and volume. The sum of the Euclidean lengths of the segments making the branch is equal to its length.

6.2 Length of the skeleton

We define the length of a branch in the solid ER by the euclidean distance between the end points (nodes) of the corresponding skeleton. Let N_{b_j} be the number of the ordered points, $P_{j_i}(x_{j_i}, y_{j_i}, z_{j_i})$, contained in the *connected*, *centred*, *thin*, *homotopic* skeleton $\mathcal{S}(b_j)$ of branch b, as described in Chapter 4; then the length of branch b_j, denoted by $\mathcal{L}_{b_j}$ can be expressed in terms of the sum of the Euclidean lengths (straight line distances) of its $N_{b_j} - 1$ line segments as follows:

$$\mathcal{L}_{b_j} = \sum_{i=0}^{N_{b_j}-2} \|\overrightarrow{P_{j_i}P_{j_{i+1}}}\| = \sum_{i=0}^{N_{b_j}-2} \sqrt{\left(x_{j_{i+1}} - x_{j_i}\right)^2 + \left(y_{j_{i+1}} - y_{j_i}\right)^2 + \left(z_{j_{i+1}} - z_{j_i}\right)^2}$$

where $\| \cdot \|$ denotes the length of a vector.

The total length of a solid ER specimen can be approximated by summing the lengths of the edges of its skeleton,

$$\boldsymbol{\mathcal{L}_T = \sum_{j=0}^{N_b-1} l_{b_j} = \sum_{j=0}^{N_b-1} \sum_{i=0}^{N_{b_j}-2} \sqrt{\left(x_{j_{i+1}} - x_{j_i}\right)^2 + \left(y_{j_{i+1}} - y_{j_i}\right)^2 + \left(z_{j_{i+1}} - z_{j_i}\right)^2}}$$

6.3 Surface area of the specimen

We define an isosurface as a surface in 3-D space that defines constant values of the grey level intensity. If the surface area of a solid ER specimen (see Figure 6.2(a) on page 99) is represented by a triangulated mesh $\mathcal{M}$ (see Figure 6.2(b) on page 99), then its total surface area can be obtained by summing the areas of its triangles. Given three points in space $T_{j_0}(x_{j_0}, y_{j_0}, z_{j_0})$, $T_{j_1}(x_{j1}, y_{j_1}, z_{j_1})$, and $T_{j_2}(x_{j_2}, y_{j_2}, z_{j_2})$ (see Figure 6.2(c) on page 99); from linear algebra it is known that the area of triangle $T_j = \Delta T_{j_0} T_{j_1} T_{j_2}$, denoted $\mathcal{A}(T_j)$, is half the magnitude of the cross product

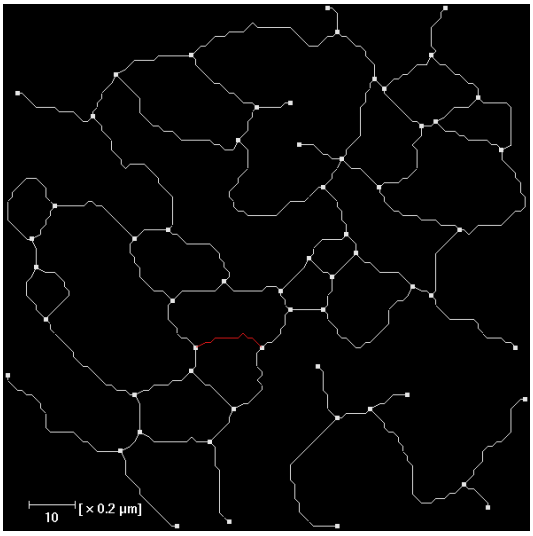

(a) A 1D representation of the solid ER using its skeleton

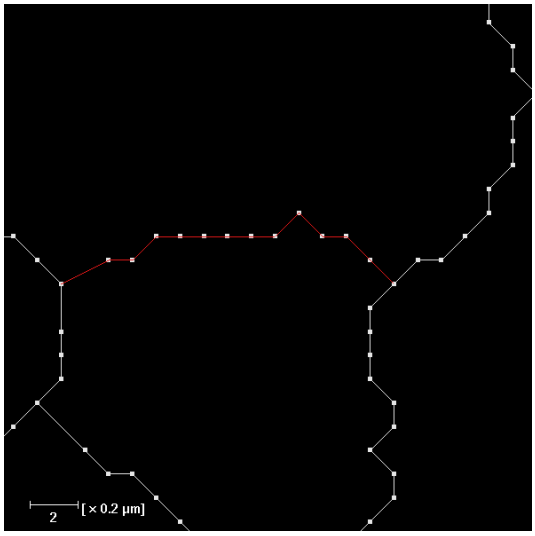

(b) Each edge skeleton consists of a discrete number of points

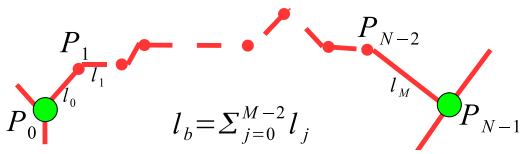

(c) The total length of a branch is approximated by the length of its skeleton.

Figure 6.1: The approximation of the length of a solid ER branch by the length of its skeleton

$\overrightarrow{T_{j_0}T_{j_1}} \times \overrightarrow{T_{j_0}T_{j_2}}$,

$$\mathcal{A}(\Delta T_j) = \frac{1}{2}\|\overrightarrow{T_{j_0}T_{j_1}} \times \overrightarrow{T_{j_0}T_{j_2}}\|$$

$\overrightarrow{T_{j_0}T_{j_1}} \times \overrightarrow{T_{j_0}T_{j_2}}$ can be obtained by the following determinant

$$\overrightarrow{T_{j_0}T_{j_1}} \times \overrightarrow{T_{j_0}T_{j_2}} = \begin{vmatrix} \overrightarrow{i} & \overrightarrow{j} & \overrightarrow{k} \\ (x_{j_2} - x_{j_1}) & (y_{j_2} - y_{j_1}) & (z_{j_2} - z_{j_1}) \\ (x_{j_0} - x_{j_1}) & (y_{j_0} - y_{j_1}) & (z_{j_0} - z_{j_1}) \end{vmatrix}$$

where $\overrightarrow{i}$, $\overrightarrow{j}$, and $\overrightarrow{k}$ are the unit vectors in the x, y, and z directions respectively.

If mesh $\mathcal{M}$ consists of N_T triangles, T_0, T_1, ..., T_{N-1}; then its total area

$\mathcal{A}_T(\mathcal{M})$ ***is the sum of the areas of these triangles.***

$$\boxed{\mathcal{A}_T(\mathcal{M}) = \sum_{j=0}^{N-1} \mathcal{A}(T_j)}$$

6.4 The volume of the specimen

Since the dimensions d_{XY} and d_Z (and therefore the size $\mathcal{V}_{size} = d_{XY} \times d_{XY} \times d_Z$) of a voxel are provided by the confocal microscope at the data acquisition step (see

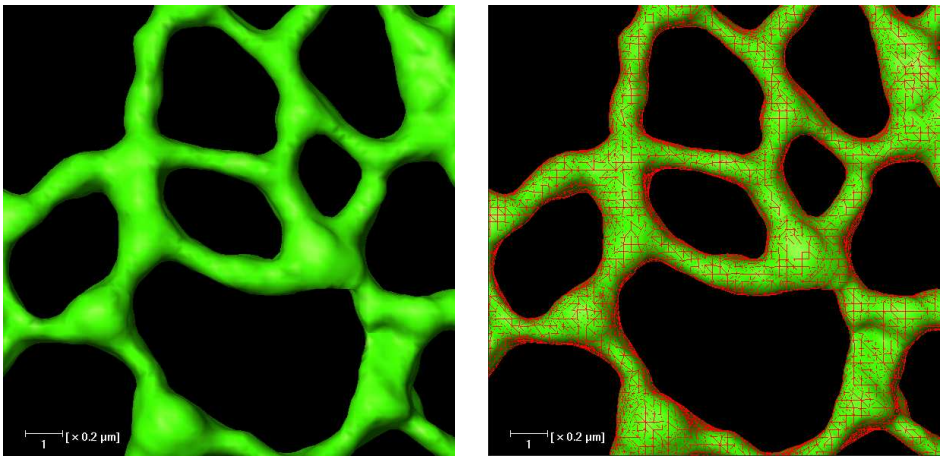

(a) An isosurface of a solid ER sample (b) The corresponding triangulation

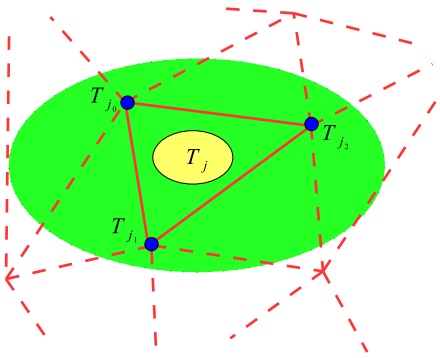

(c) The area of a triangle is half the magnitude of the cross product of the vectors made by two adjacent edges.

Figure 6.2: The specimen's total surface area is approximately equal to the sum of the areas of the triangles.

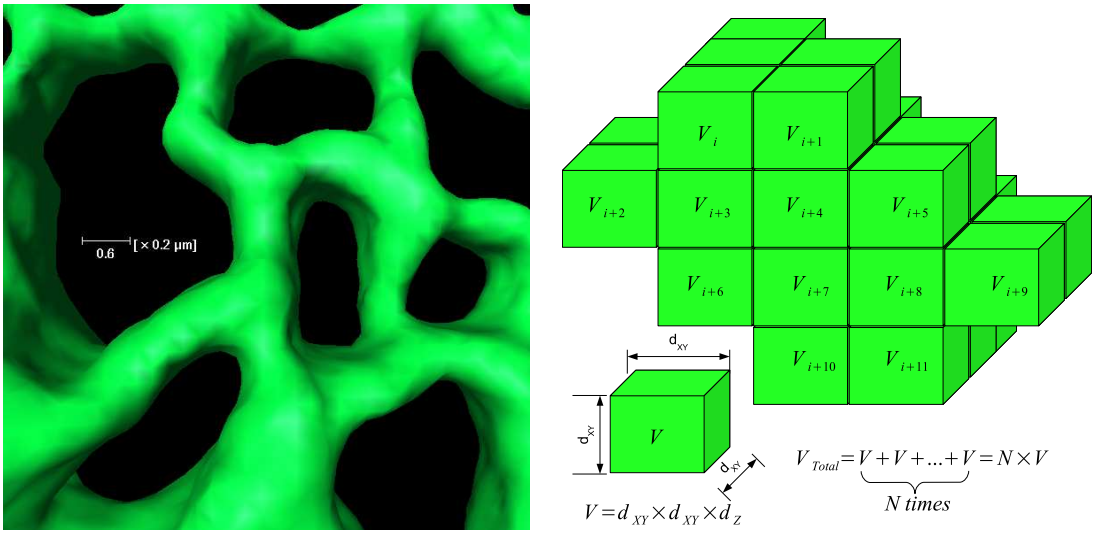

(a) An isosurface of a solid ER sample (b) The voxels forming isosurface

Figure 6.3: The sum of voxels making the foreground of an image is equal to its volume.

Section 3.3.5 on page 46), then the total volume of the specimen (foreground of the images) can be approximated by discarding voxels in the background and summing the non-zero voxels, then multiplying the result by the size of one voxel.

$$\mathcal{V}_T(M) = \mathcal{V}_{size} \times N_F$$

6.5 Characterisation of a Junction

Junctions are where the branches of the solid ER meet. This thesis characterises a solid ER junction by the number of branches emerging from it. In mathematical terms this is equal to the degree (valence) of the corresponding vertex.

6.6 The local diameter

The radius of the solid ER at a point p in the skeleton is equal to the distance between p and the closest point in the background. This can directly be obtained using distance maps (see Section 4.5.2 on page 70).

Algorithm 3: The average cross section diameter of a solid ER tubule.

Input: Distance map ($dist(I)$) of a solid ER image I, and the corresponding Skeleton $\mathcal{S}(I)$

Output: Average local diameter of each edge $d(E_j)$

```
1  load distance map dist(I);
2  load skeleton S(I);
3  split the skeleton into edges S(I) = sum_{j=0}^{M} E_j;
4  foreach edge E_j in the skeleton do
5      initialise the local diameter of edge E_j to zero: d(E_j) = 0;
6      foreach point P_{j_i} in edge E_j do
7          read intensity value g(P_{j_i});
8          increment the edge local diameter d(E_j) ← d(E_j) + g(P_{j_i}) ;
9      end
10     d(E_j) ← d(E_j)/N_j, where N_j is the number of points in edge E_j.
11 end
```

6.7 The length and area densities

The length density of the cortical solid ER can be estimated by dividing the total length by the area of the ROI $l_V = l_{Total}/A_{ROI}$. The area density of the cortical solid ER can be estimated by dividing the total area by the area of the ROI $A_V = A_{Total}/A_{ROI}$.

6.8 Associating surface areas and volumes to edges

Algorithm 4: Surface area of a solid ER branch

Input: Voxelised solid ER specimen

Input: The corresponding triangulation

Input: The corresponding skeleton

Output: Surface area per branch

1 *load triangulation*;
2 *load skeleton*;
3 *calculate total surface area of the specimen*;
4 *split the skeleton into edges*;
5 *initialise the surface areas of all edges to zero*;
6 **foreach** *Triangle* T_i **do**
7 *calculate the surface area of triangle* T_i, A_{T_i};
8 *obtain the centre of gravity* T_{cg_i};
9 *find the closest point in the skeleton to* T_{cg_i};
10 *find edge* $E_{\mathcal{S}_j}$ *such that* $\mathcal{S}_j \in E_{\mathcal{S}_j}$;
11 *increment the surface area of edge* $A(E_{\mathcal{S}_j})$ *by* A_{T_i};
12 **end**

To calculate the surface area of the edges, this thesis splits the skeleton of a solid ER specimen into edges, and each edge into a set of points. It then uses the triangulation of the surface area of the specimen to associate each of its triangles T to the nearest edge point in the skeleton. In this way this thesis associates to each point the areas of the set of triangles that are closer to it than to any other point in the skeleton, and hence it obtains the surface area of each point by adding its associated triangle areas. Finally the surface area of an edge is the sum of the surface areas of its inner points plus the surface area of each edge end point divided by its degree (see Algorithm 4 on page 102).

6.9 Associating volumes to edges

Algorithm 5: Volume of a solid ER branch

Input: Voxelised solid ER specimen, the corresponding Triangulation, and Skeleton

Output: Surface area, volume and average local diameter of each edge

1 *load isosurface*;
2 *load skeleton*;
3 *calculate total volume of the isosurface*;
4 *split the skeleton into edges*;
5 *get the size of one voxel* V_{size};
6 *initialise the volumes of all edges to zero*;
7 **foreach** *voxel* V_i *in the solid ER* **do**
8 *obtain* (xc_i, yc_i, zc_i) *the coordinates of the upper top left corner of voxel* V_i;
9 *find* $\mathcal{S}_j$ *the closest point* S_j *in the skeleton to* (xc_i, yc_i, zc_i);
10 *find edge* $E_{\mathcal{S}_j}$ *such that* $\mathcal{S}_j \in E_{\mathcal{S}_j}$;
11 *increment the volume of edge* $V(E_{\mathcal{S}_j})$ *by* V_{size};
12 **end**

To calculate the volumes of the edges, this thesis splits the skeleton of a solid ER specimen into edges, and each edge into a set of points. It then uses the isosurface of the specimen to associate each of its voxels V to the nearest edge point in the skeleton. In this way this thesis associates to each point of the skeleton the set of voxels that are closer to it then to any other point in the skeleton, and hence it obtains the volume of each point by counting its associated voxels and multiplying the result by the size of one voxel. Finally the volume of an edge is the sum of the volumes of its inner points plus the volume of each edge end point divided by its

degree (see Algorithm 5 on page 103).

6.10 Short review of Graph Theory

This thesis represents the solid ER skeleton by an undirected weighed graph $\mathbf{G} = (\mathbf{V}, \mathbf{E})$, where $\mathbf{V} = [v_1^T, v_2^T, \cdots, v_n^T]^T$ is a finite set of vertices representing the positions of the junctions in the reticulum, and $\mathbf{E} = [e_1, e_2, \cdots, e_n]$ the edges connecting them. We call the number of edges emerging from vertex v_i^T its ***degree (or valence)*** and the closed path, starting from vertex v_i^T, which does not have repeated vertices a ***cycle***. While degree distribution represents the branches at a vertex, cycle distribution describes the number of holes in the network. Since the ER is almost two dimensional through the z-axis, meaning that different z-cross-sections have the same topology, this thesis maps the extracted skeleton, which is three dimensional, to a graph, that is two dimensional, without affecting the homotopy type of the original network. The advantage of this mapping is that it is easier to analyse different homotopic features of an ER specimen such as the distribution of vertex degrees and the network cycle distribution. The degree distribution is a fundamental property in graph theory. The number of cycles in the graph corresponds to the number of holes the solid ER forms in the original network. This thesis draws the graphs in a plane, whereas the network obtained from the thinning algorithm still has nodes with the original three-dimensional coordinates.

Part III

Results

7

Quantification of the Static ER

In this chapter we look at the homotopy type of an almost static sample of the plant cortical solid ER under close to normal physiological conditions using a multi-disciplinary approach combining confocal microscopy, image processing techniques, visualisation, computational geometry and graph theory. Data collected from a series of optical sections taken at short regular intervals along the optical axis are used to reconstruct the solid ER in 3D. A graph structure of the ER network is obtained after thinning the solid ER geometry to its essential features. The graph is the final and most abstract quantification of the solid ER and serves very well as a geometrical invariant, even, and very importantly, in cases where the ER sam-

ple is moving or slightly changing shape during image acquisition. Moreover graph theoretic features, such as the number of nodes and their degrees, and the number of edges and their lengths, are very robust against different kinds of small perturbations, provided none of the edges is very short, which should not change the ER function. We will also attach surface areas and volumes estimated for the plant ER network as weights to the graph, allowing an even more precise quantitative characterisation of this organelle. In total we have compared 28 different samples under similar experimental conditions. The methods used in this chapter should also be applicable to the quantification of other organelles where geometric abstraction is possible to analyse function. Finally by the use of confocal microscopy our techniques will be transferable to situations where protein markers can move inside the organelle's lumen and/or on the membrane surface to test further aspects of protein distribution.

7.1 Introduction

Chapter 2 has indicated that the endoplasmic reticulum (ER) is the port of entry of the secretory pathway in all eukaryotic cells, and that it is a pleiomorphic organelle, which greatly varies in shape, from smooth sheets around the nuclear envelope to a polygonal network of tubules extending throughout the cell volume (see (Lichtscheidl & Hepler, 1996; Vitale & Denecke, 1999) and Vitale *et al.* (1993)). Chapter 3 has also concluded that plant cells offer a very attractive model for the study of this organelle due to its pleiomorphic nature (Staehelin, 1997), because in vegetative cells, whose volume is in large part occupied by the central vegetative vacuole, the ER is forced by turgour pressure against the plasma membrane and the cell wall. Therefore cortical ER occupies a very thin, almost two dimensional, layer of cytoplasm beneath the plasma membrane. This is ideal for the study of the ER architecture and dynamics using light microscopy (see Section 2.9 on page 20 for

more details).

7.2 Material and methods

7.2.1 Plant material

Nicotiana tabacum cv Petit Havana SR1 was grown in greenhouse conditions. Healthy, 5 to 8 week old leaves were selected for agroinfiltration.

7.2.2 Agroinfiltration and confocal analysis

Leaves were infiltrated with a suspension of *Agrobacterium tumefaciens* containing expression vector pVKH18En6-GFP-HDEL as described previously (see Batoko *et al.* (2000)). Agrobacteria were at an OD600 of 0.05. After 72 h, leaf sections were incubated in 1 μM latrunculin B (Calbiochem) in water for 30 min, then mounted in water and visualised with a Leica TCS SP2 confocal scanning microscope using a 63× oil immersion objective (NA1.3). GFP was excited at 488 nm and visualised with an emission window of 500-530 nm.

Optical sections were acquired with a z step size of 0.2 μm, matching the x-y pixel size (voxel-width = voxel-height = voxel-depth = 0.2 μm). Each specimen contained 20 z-sections. The pinhole size was set to 1.0 AU (178 μm), the scan speed to 400, the frame-average to 1, and the line-average to 2. There were 8 bits per sample and the zoom was set to 2.32.

7.2.3 Coding

Pre-processing, skeletonisation, 3-D reconstruction and isosurface generation of the z-series data were implemented in Tool Command Language (TcL) using *Amira 4.1.2*, a commercial software on a Linux platform. More details can be found in Appendix A.4 TcL scripts. Degrees, lengths, surface areas, and volumes were associated to the corresponding Edges/Nodes using a newly developed C++ code (see Appendix A.1: C++ codes for details). Adjacency matrices, weights and their corresponding graphs were obtained by using the *BOOST* graph library and *graphviz* (BGL, 2002) through the DOT graph description format. All the statistics were obtained using Matlab (see Appendix A.3: Matlab files for details). Isosurfaces

7.2.4 Key background information

We obtained data from seventy samples taken from twenty-eight different cells. From each of sixteen cells (*Sample Set 1*) we took a single sample of size 22 μm × 12 μm × 4 μm near the cell wall. From each of the remaining twelve cells (*Sample Set 2*) we took several samples of size 11 μm × 12 μm × 4 μm starting near the nucleus and extending to the cell wall, totalling fifty-four samples.

The samples taken from the last twelve cells demonstrate that the key solid ER characteristics we are looking at in this chapter do not vary significantly with distance from the nucleus. Throughout the remainder of this chapter we refer to *Sample Set 1* or *Sample Set 2* if we wish to distinguish between the sixteen cells set or the twelve cells set respectively.

7.2.5 Image analysis

To geometrically quantify the solid ER network, within each of the seventy regions of interest, described in section 8.3.1 on page 140, we associate to each edge its length, its surface area, and its volume, and to each node the number of edges emerging from it (or its degree in graph theoretic terms), its surface area, and its volume. We use the average values of these parameters to characterise the network at rest.
To obtain these averages we follow three main steps: (a) an image pre-processing step to denoise data, followed by (b) a 3-D reconstruction and skeletonisation step, and finally (c) a calculation step where we allocate lengths, surface areas and volumes to their corresponding edges. These steps are explained in Sections 7.2.5 on page 111, 7.2.5 on page 114, and 7.2.5 on page 117 respectively.

Image pre-processing

Raw data contain noise, which is mainly due to photon statistics (a sub-optimal signal-to-noise ratio), and artifacts such as light absorption from other slices occurring during data acquisition. To avoid missing important information and obtain the closest possible reconstruction to the real network we use the minimum processing possible. To reduce the artifact due to the intensity of light coming from other z-slices we apply the Amira automatic z-drop correction, also known as **intensity attenuation** (Fouard *et al.*, 2006; Zuse, 2006).

Using a sample of size 24.91 μm × 33.55 μm × 8.80 μm, we demonstrate the entire image pre-processing procedure in Figure 7.1 on page 112, using confocal slices, and in Figure 7.2 on page 113, using isosurfaces.

The z-drop corrected data, Figure 7.1(b) and Figure 7.2(b), contain small unconnected elements scattered around a large connected network structure. We remove

these elements using **3-D median filter** (kernel size set to 3 throughout our calculations, Figure 7.1(c) and Figure 7.2(c)), see (Gonzalez & Woods, 2002), . To obtain a smooth skeleton we finally apply a **3-D Gaussian filter**, with $\sigma = 0.4$, kernel size = 3, Figures 7.1(d) and 7.2(d), as discussed in 7.2.5. The effects of the z-drop correction, the median filter and the Gaussian filter are discussed in the following paragraphs.

Figure 7.2(b) shows the effect of Amira automatic z-drop correction on Figure 7.2(a)

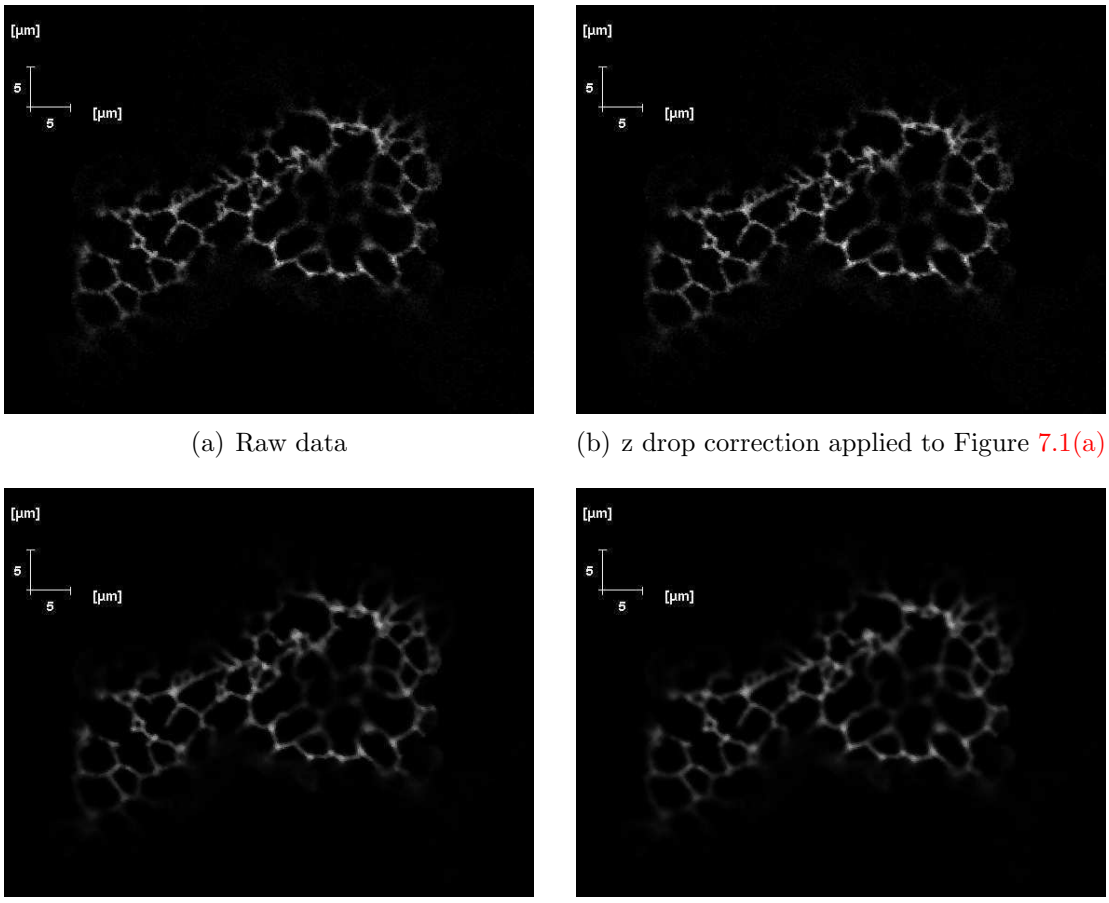

(a) Raw data

(b) z drop correction applied to Figure 7.1(a)

(c) 3D median filter applied to Figure 7.1(b)

(d) 3D Gaussian filter applied to Figure 7.1(c)

Figure 7.1: An illustration of the pre-processing procedure: (a) raw image (slice 28 out of 44 of size: 65.4 μm × 57.2 μm) of *Nicotiana tabacum cv* Petit Havana SR1 cell when treated with latrunculin B (Calbiochem) taken with a Leica TCS SP2 confocal scanning microscope using a 63× oil immersion objective (NA 1.3), (b) automatic z-drop corrected image, (c) Image after applying 3-D Median, kernel size = 3, (d) Result after applying a 3-D Gaussian, $\sigma = 0.4$, kernel size = 3, to the 3-D median filtered image. Scale bars: 5μm and 5μm in the x and y directions respectively

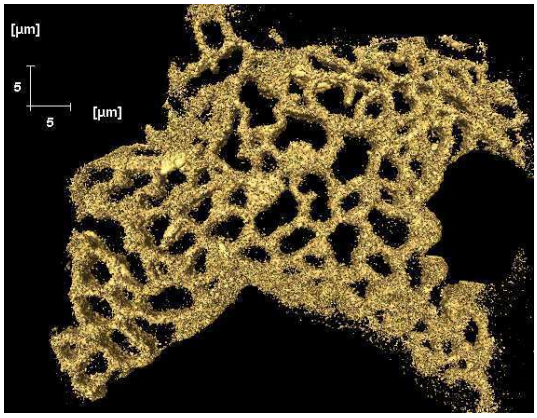

(a) Raw data isosurface (Volume (V)=1405.51 μm^3, Surface Area (A)=14702.7 μm^2)

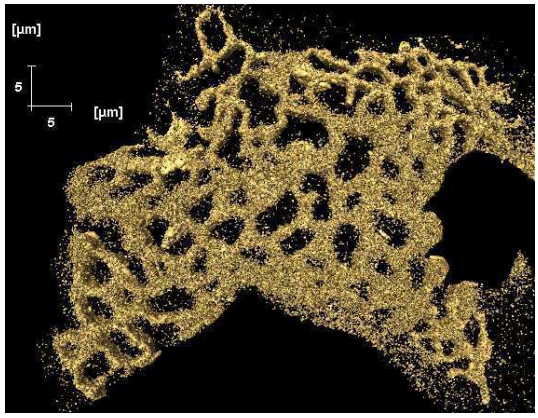

(b) z-drop correction applied to raw data in Figure 7.2(a) (V=1707.55 μm^3, A=14480.7 μm^2)

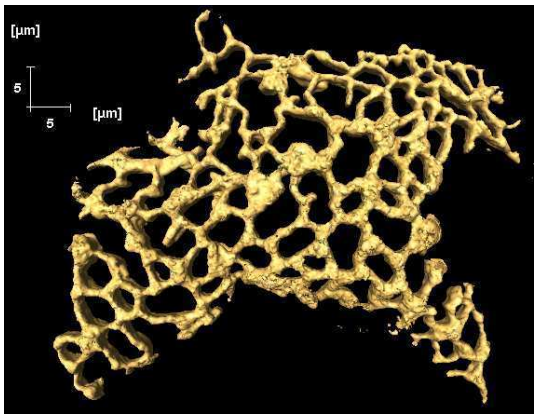

(c) 3-D median filter applied to the z-drop corrected data in Figure 7.2(b) (V =1691.9 μm^3, A=5565.13 μm^2)

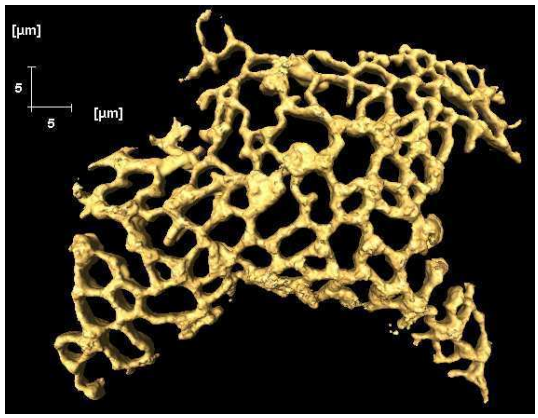

(d) 3D Gaussian filter applied to the median filtered data in Figure 7.2(c) (V=1805.59 μm^3, A=5361.13μm^2)

Figure 7.2: The pre-processing procedure illustrated using isosurfaces (Threshold = 6): (a) raw sample of size: 65.4 μm × 57.2 μm × 11.2 μm, (b) Sample after applying an automatic z-drop correction, (c) z-drop corrected sample after after applying a 3-D median filter, with kernel size = 3, (d) the final result after applying a 3-D Gaussian filter, $\sigma = 0.4$, kernel size = 3, to the 3-D median filtered sample. Scale bars: 5μm and 5μm in the x and y directions respectively

for a threshold value equal to 6 (21 % increase in the total volume and nearly 2% decrease in the total surface area). When applying a 3-D median filter, as in Figure 7.2(c), to the z-drop corrected data in Figure 7.2(b), we obtain a decrease of 1% in the total volume and a considerable decrease of 62 % in the total surface area due to the removal of isolated elements (salt and pepper noise in image analysis terms).

Applying the Gaussian filter for the sample in Figure 7.2 causes a change of around 1% in volume, compared to the median filtered data, and 7% change in its total surface area; see Figure 7.2(d) and Figure 7.2(c) .

We investigated the Gaussian filter kernel size effect on the final results, by repeating the calculations for sizes 1 to 7, see Figure 7.3 on page 115 and Figure 7.4 on page 116. Deviations from the median filter results increase with the kernel size in both surface areas and volumes.

Figure 7.5 on page 117, showing the effect of the standard deviation on the final results, indicates that, in both cases, deviations from the median results increase with the standard deviation σ. A similar approach was adopted by Fouard (2005) to analyse 3-D images of the cerebral micro-vascular network which involves centre lines extraction and vessel diameters estimation.

3-D Reconstruction and skeletonisation

The result of the pre-processing procedure is a three dimensional distribution of fluorescence, that can be visualised by separating the solid ER from the background using a thresholding technique. It is important to note that the final results in any such study will greatly depend on the choice of the threshold value. We justify such choices by repeating the analysis over a wide range of usable thresholds, i.e. those which yield a connected network structure. Figure 7.6 on page 118 shows that

for threshold values below 1, for this particular sample, we obtain an amalgamated network which is not biologically relevant.

Between threshold values 2 and 6 we obtain a complete connected network. As we reach threshold 7 we start losing parts of the network. A statistical summary of the results can be found in Figure 7.7 on page 119. It should be noted that in principle for every individual sample an own biologically relevant threshold must be computed. The reason is that the circumstances how light is diffracted can differ over a wide range of relevant properties, for example depending on thickness of the cuticule. This does of course complicate the ability to compare samples, mainly with respect to surface areas and volume. Nevertheless, in order to reach comparability, the same threshold can be applied globally for samples that have been taken under very similar circumstances, for example in cases where the ROIs have been selected from one given larger image, see Figure 7.18 on page 130.

To count the number of edges in a solid ER sample, and to measure their lengths, surface areas, and volumes we use its skeleton, which has the same homotopy type. Full details on how to obtain such a skeleton, in Amira, is not the focus of this chapter and can be found in Calabi & Harnett (1968); Fouard (2005); Malandain & Fernández-Vidal (1998) and Zhou *et al.* (1998)).

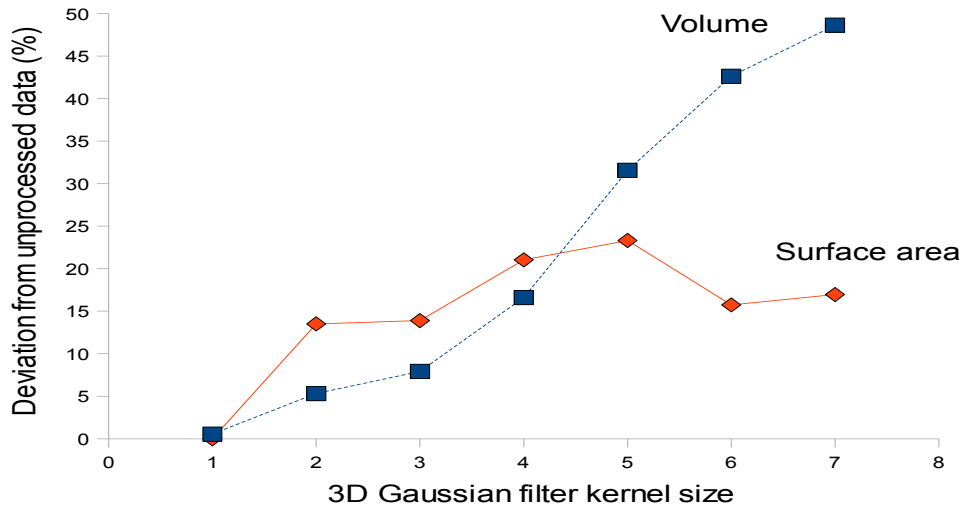

Figure 7.3: Effect of the 3-D Gaussian filter kernel size on the total surface area and total volume.

Effect of smoothing edges Since we are operating in discrete voxel space, the path going through the vertices belonging to a branch could be quite rough as segments between directly neighbouring voxels may contain many 45^0 and 90^0 turns. To assess how this might affect the final edge lengths we repeated the calculations by varying the degree of smoothing while keeping all other parameters fixed.

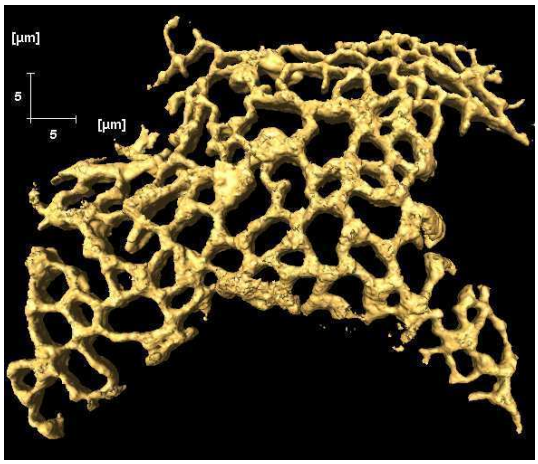

(a) 3D Gaussian filter kernel size 2: V=1712.04 μm^3(22 % deviation from unprocessed data), A= 5541.48 μm^2(−62% deviation from unprocessed data)

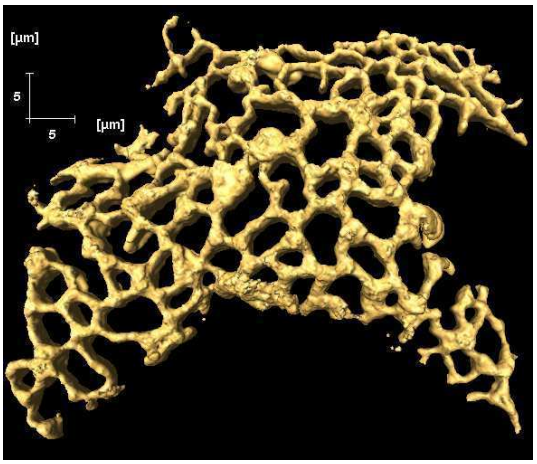

(b) 3D Gaussian filter kernel size 3: V=1805.59 μm^3, (28 % deviation from unprocessed data) A= 5361.13 μm^2(−64% deviation from unprocessed data)

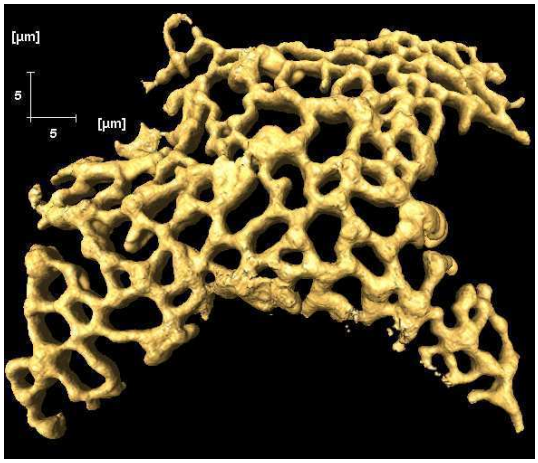

(c) 3D Gaussian filter kernel size 6: V=2327.9 μm^3,(-67 % deviation from unprocessed data). A= 5581.52 μm^2, (−62% deviation from unprocessed data)

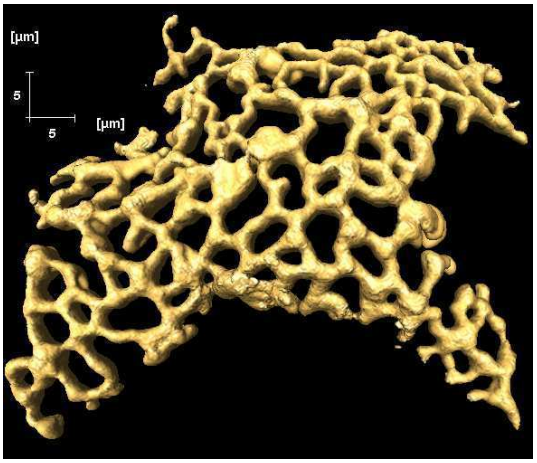

(d) 3D Gaussian filter kernel size 7: V=2275.18 μm^3 (62 % deviation from unprocessed data), A= 5341.81 μm^2(−64% deviation from unprocessed data)

Figure 7.4: Effect of 3-D Gaussian filter kernel size on the volume and surface area. Scale bars: 5μm and 5μm in the x and y directions respectively.

The results, summarised in Figure 7.8 on page 120, show that there is little variation in length between smoothed and unsmoothed edges.

Length, surface area, and volume calculation

We calculate the total volume of an isosurface by simply counting the number of its voxels and then multiply the result by the volume of one voxel ($8{\times}10^{-3}\mu m^3$ in this case). To compute the total surface area we first triangulate the isosurface, then sum the surface areas of its triangles. The effect of the threshold on these two parameters is discussed in section 7.2.5 on page 114.

We obtain the lengths of edges by adding the Euclidean distances of all of their relevant sub-segments. The effect of smoothing on the final edge length can be found in see Section 7.2.5 on page 116.

To calculate the volumes and surface areas of the edges and nodes, we associate each voxel V (in the isosurface) and each surface triangle T (in the triangulated isosurface) to the nearest edge points in the skeleton, using their centre of gravity, see Figure 7.10 on page 121. Finally we estimate the minimum radius of a point

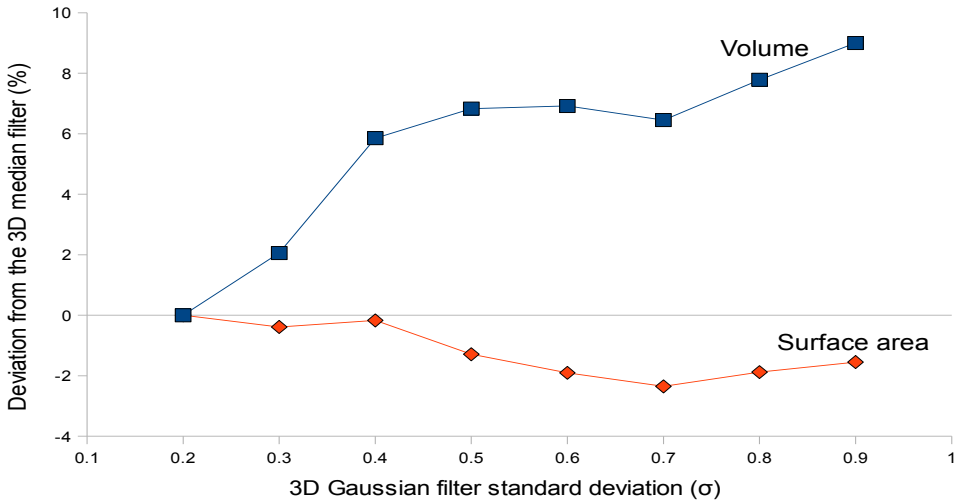

Figure 7.5: Effect of the 3-D Gaussian filter standard deviation on the total surface area and total volume.

in the skeleton by calculating its distance to the nearest point in the background. Note that by adding up all surface areas or volumes associated to edge points and segments of the skeleton (and finally the graph G) the result is total surface or volume of the solid ER inside the ROI.

In the end we associate to each vertex $\mathbf{v}$ its degree Deg_v, its outer surface area $S_{\mathbf{v}}$, and its volume $V_{\mathbf{v}}$; and to each edge $\mathbf{e}$ we associate its length L_e, its outer surface

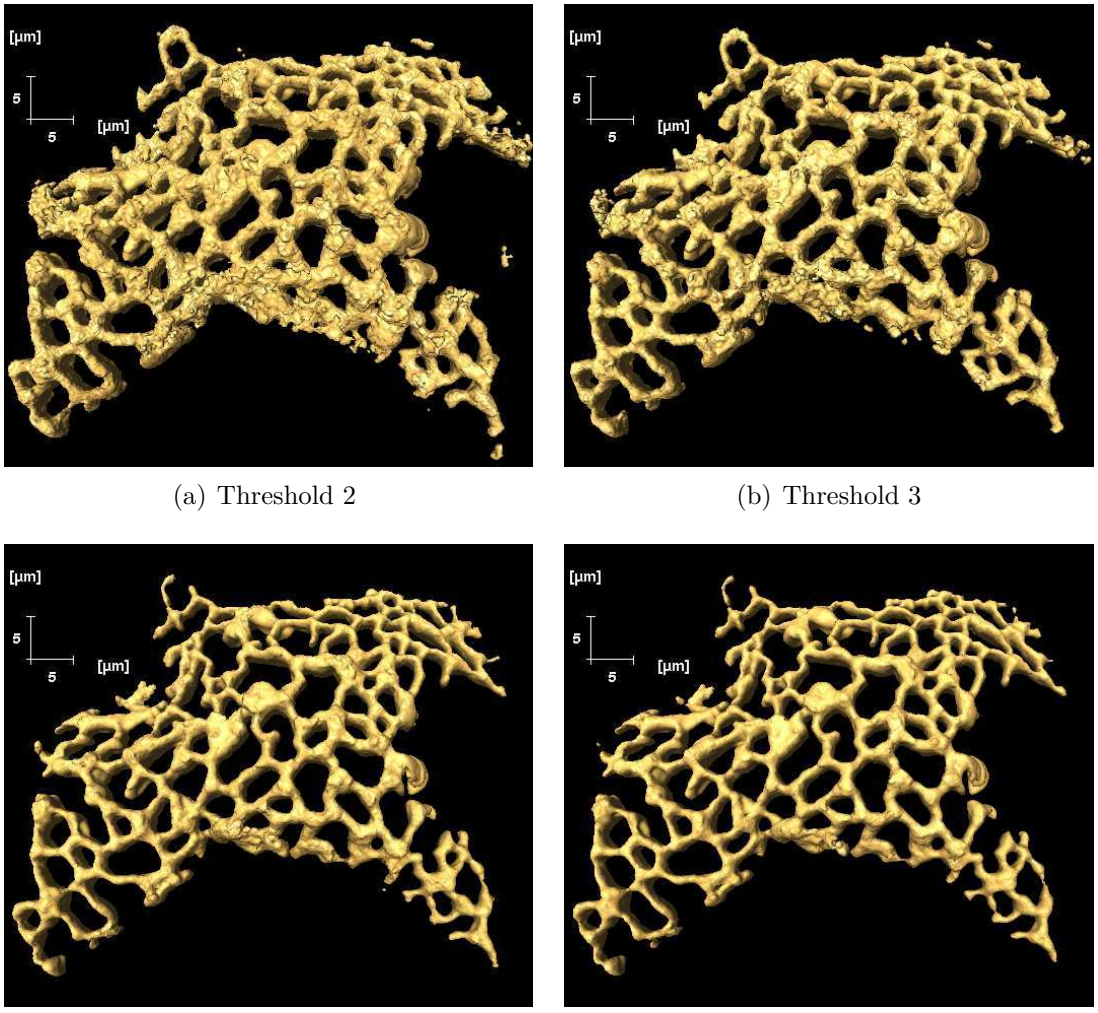

(a) Threshold 2 (b) Threshold 3

(c) Threshold 6 (d) Threshold 7

Figure 7.6: Effect of threshold values on the size of the isosurface when applying the above procedure, i.e. z-drop correction, followed by a 3-D median filter (kernel = 3), then a 3-D Gaussian filter (kernel size = 3, and $\sigma = 0.4$). (a) For threshold values below 2 we obtain a melted object that is not biologically relevant. (b) between thresholds 3 and 6, frames (b) and (c) respectively, we get a fully connected network. (d) The network starts to fragment for thresholds above 6. Scale bars: 5μm and 5μm in the x and y directions respectively

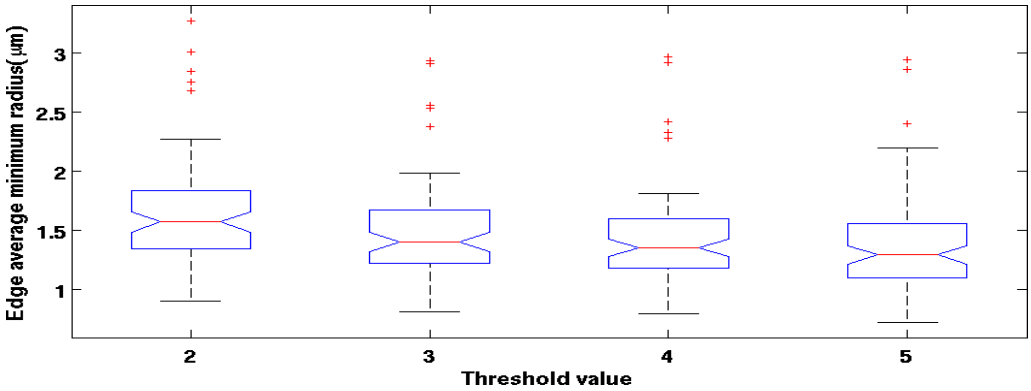

(a) Effect of the threshold value on the edge average minimum radius

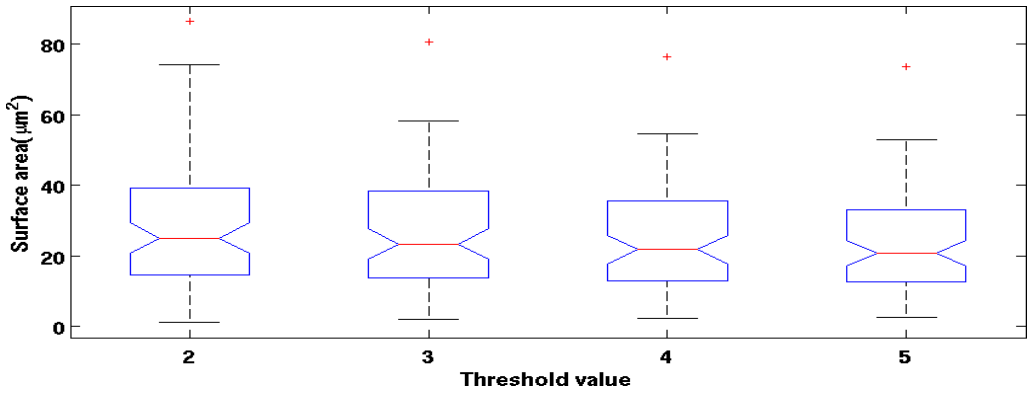

(b) Effect of the threshold value on the surface area

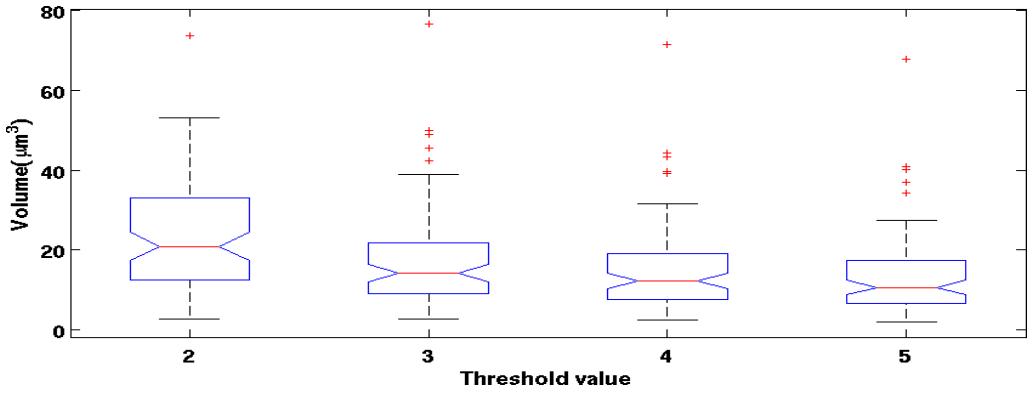

(c) Effect of the threshold value on the volume

Figure 7.7: Box plots showing the effects of the threshold value T on the final results for the solid ER surface and volume values of the sample shown in Figure 7.1 on page 112. For threshold values in the range 2 to 6 the average edge surface area A_e varies from a maximum value of 28.88 μm^2, with standard deviation $\sigma = 18.06$ and corresponding to $T = 2$ and a minimum value of 23.31 μm^2, with $\sigma = 13.74$ corresponding to $T = 5$. The average volume of an edge decreases from 22.83μm^3 with $\sigma = 15.55$ to 13.51 μm^3, with $\sigma = 10.49$

area $S_\mathbf{e}$, its volume $V_\mathbf{e}$, and its average diameter $D_\mathbf{e}$. We use the averages of these parameters to characterise the solid ER geometry.

Smoothing	L_e (μm)
Original	3.49
2	3.06
3	3.02
4	2.99
5	2.97
6	2.96
7	2.94
8	2.93
9	2.92
$\overline{L}$	**3.03**
Min	**2.92**
Max	**3.49**
σ	**0.18**

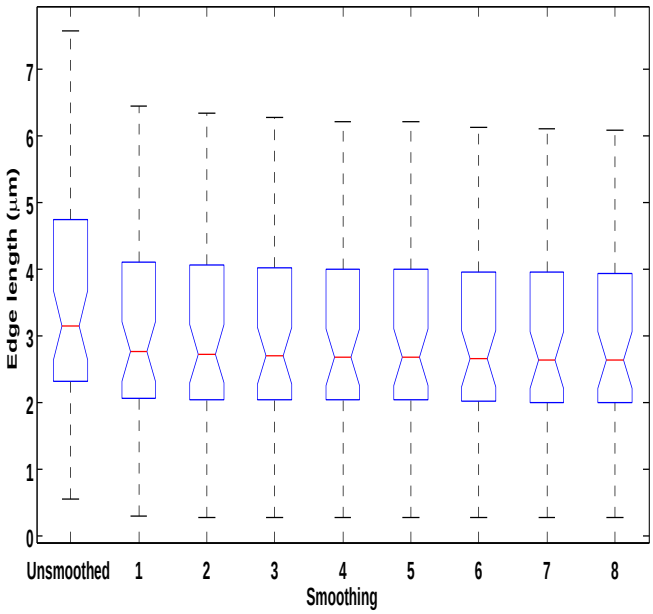

Figure 7.8: Edge length L_e vs. smoothing applied to the sample of Figure 7.1 on page 112

7.2.6 The ER as an abstract geometrical structure

To simplify the analysis of the network we finally represent the solid ER as a mathematical object, *a graph* $G = (V, E)$, where V is the set of vertices representing the nodes, and E the set of edges connecting them. For a representative part of the

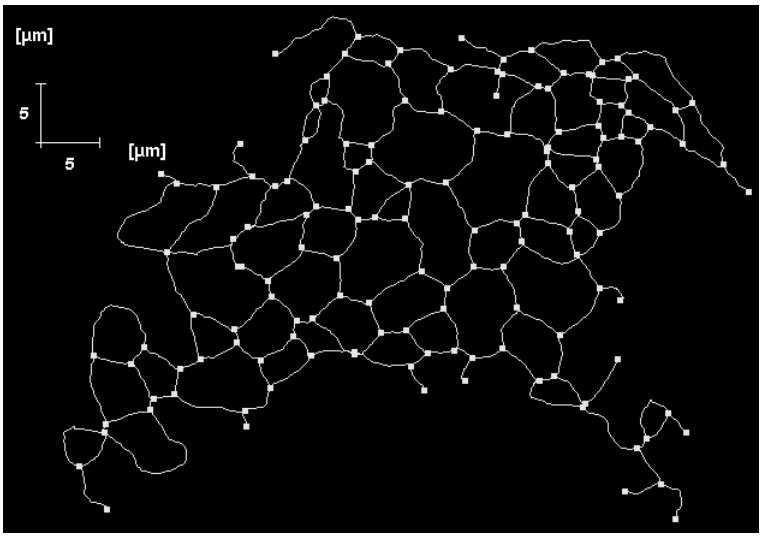

Figure 7.9: The result of the skeletonisation process is a thinned object that is homotopically equivalent to the solid ER. Shown is the skeleton of the sample seen in Figure 7.1 on page 112.

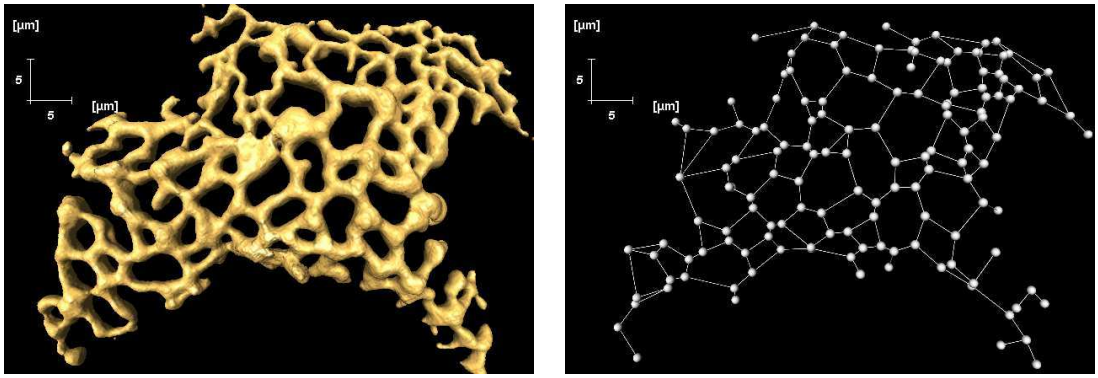

(a) ROI with reconstructed solid ER surface. (b) Graph G, the final geometrical abstraction.

Figure 7.10: The solid ER inside the ROI (sample from Figure 7.1 on page 112) has been reduced to its skeleton (see Figure 7.9 on page 120). In a further processing step we can associate solid ER voxels and ER surface triangles used to construct the ER surface shown in (a) to edges and vertices of a graph G shown in (b). Note that the segments of the skeleton shown in Figure 7.9 are geometrical, i.e. not voxel based. In the graph G associated to the ROI we can introduce an additional characterisation (a weight which is a real number, numbers not shown in the graph representation (b), but see Figure 7.17 on page 129 for an example) given by the segment lengths of the skeleton, or the surface area associated to a segment. In the latter case we can add the triangle area composing the ER surface close to the segment, as shown in (a). Finally we can introduce also volume as weights for both vertices and edges of G. In this case we count directly voxels below the triangulated surface as shown in (b). These weights are associated to the segments (creating edges) and edge points (creating vertices) of the skeleton (that later constitute the graph G). All data abstracted from the sample shown in Figure 7.1. Scale bars: 5μm and 5μm in the x and y directions respectively. The steps from raw data to the graph G are shown again in Figure 7.11 on page 123.

solid ER we can now analyse different geometric features such as the distribution of vertex degrees and the network cycle distribution. The degree distribution is a fundamental property in *graph theory*. It is defined as the number of edges adjacent to a vertex (node). The number of holes in the solid ER corresponds to the number of independent cycles in the graph. A cycle is the edge set of an undirected closed path without repeated vertices. Our graphs are drawn in a plane, whereas the network obtained from the thinning algorithm still has nodes with the original three-dimensional coordinates. We could equally display the graph in three dimensions, but the mapping to planar coordinates does not destroy any of the topological features, and is therefore done routinely. Nevertheless the given topological invariants are not sufficient to recover other typical ER properties, like the typical sequence

of broader structures (cisternae) and thinner pipes joining them. In order to get a relative picture of such characteristic geometric features we attach weights to the graph representing length of pipes. This makes the graph a weighted graph. In case of volume and surface we can choose to attach such features only to the edges, or both to vertices (nodes) and edges (links) of the graph G. According to the biological interpretation (often speaking of cisternae) we also attach volumes to nodes representing these cisternae in our graph abstraction. We have assigned a simple algorithm which takes into account ER thickness variations by distributing parts of the ER, and therefore parts of surface and volume. Obviously the weight attaching algorithm can be refined by taking variations of surface and volume along the edges into account.

A summary of the different steps followed to obtain a graph can be found in Figure 7.11 on page 123.

7.3 Results

As explained in section 8.3.1 on page 140, we extracted seventy samples from twenty-eight different cells. We then obtained 3-D reconstructions and topologically equivalent skeletons using the mean value of usable thresholds. We split the samples into two sets. Sample Set 1 consisted of sixteen samples of size 22μm $\times$ 12μm $\times$ 4 μm taken near the cell wall, as shown in Figure 7.16 on page 128, while Sample Set 2 consisted of fifty-four samples of size 11μm $\times$ 12μm $\times$ 4 μm taken from successive regions of size 11μm $\times$ 12μm $\times$ 4 μm, starting at the nucleus and extending out to the cell wall as shown in Figure 7.18. For each edge in the skeleton we calculated the average diameter, the length, the surface area and the volume, and for each vertex in the skeleton we calculated the average diameter, the degree, the surface area and the volume as described in Section 7.2.5 on page 117, including only edges whose end points have degrees strictly greater than 2 (to avoid artificial edges, i.e. the

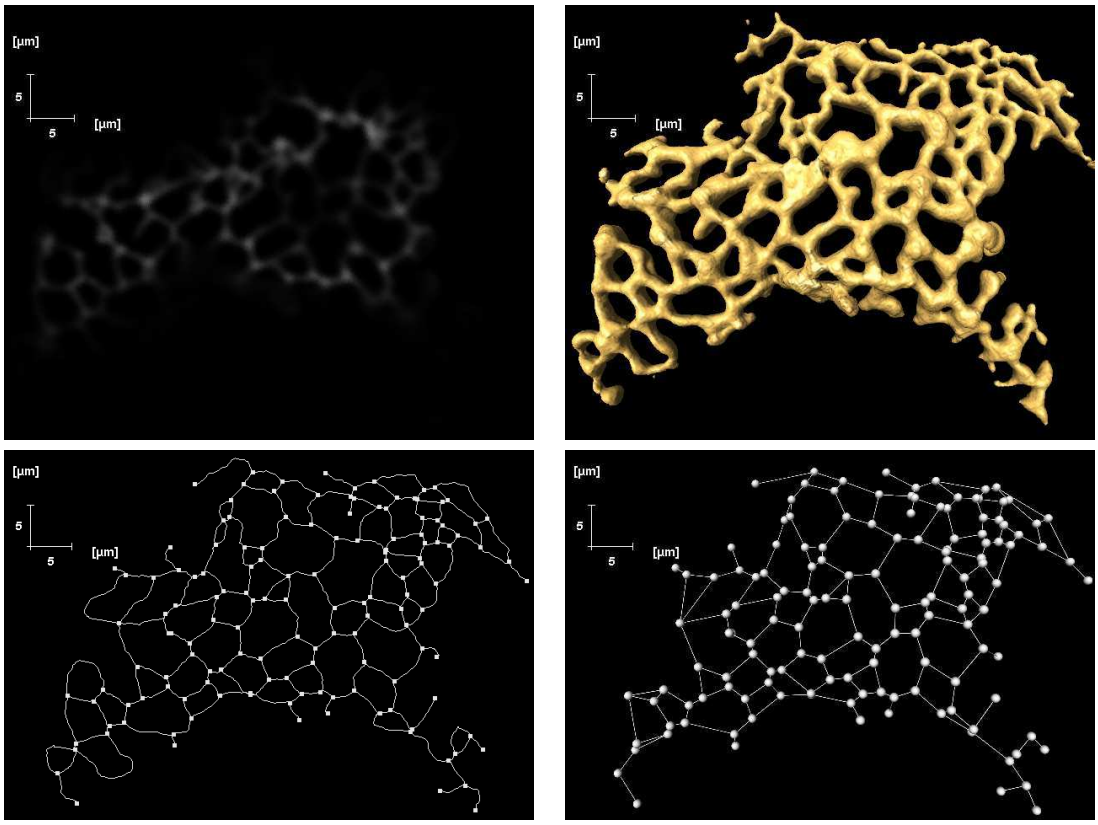

Figure 7.11: Steps followed to obtain a graph from the sample shown in Figure 7.1 on page 112. (a) raw data (threshold value 6) (b) processed data isosurface (threshold value 6) (c) thinned image (d) the equivalent graph representing volumes associated to edges obtained using the BOOST graph library. Scale bars: 5μm and 5μm in the x and y directions respectively.

edges located at the intersection planes of the ROI and the sample introduced as a result of cropping.)

Analysis of variance We used both parametric (ANOVA), and non-parametric (Friedman) tests to check if the above parameters, obtained from Sample Set 2, change with distance to the nucleus (see Figure 7.18 on page 130). When assessing the validity of one-way ANOVA, after checking for outliers by discarding edges with lengths and diameters that are less than the confocal resolution, and applying Levene's test to check for homogeneity followed by Kolmogorv-Smirnov (KS) test for normality see (Grafen & Hails, 2002), we found that despite transforming the data, using *log*, *arcsin* and *power* transforms, our data passed the homogeneity test

but failed KS's normality test which left us with the non-parametric choice that is Friedman's test. In the following paragraphs we highlight the main findings.

Source of Variation	SS	df	MS	χ^2	$P_{value} > \chi^2$	$\chi^2_{crit.}$
Columns	240.683	3	80.228	6.884	0.0757	7.815
Interaction	3079.017	66	46.652			
Error	11958.3	368	32.495			
Total	15278	459				

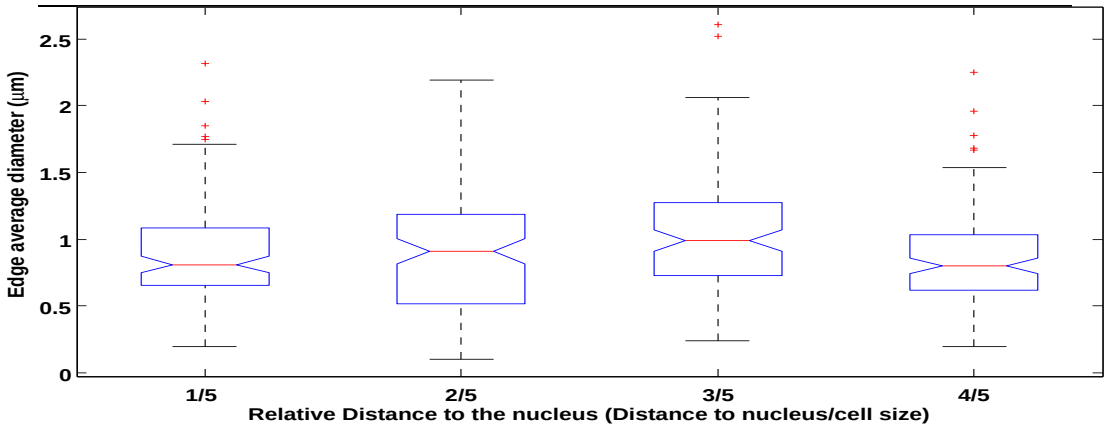

Figure 7.12: Average edge diameter vs. distance to the nucleus and the corresponding Friedman test results showing that the mean average diameters do not change significantly with distance to the nucleus $\chi^2 < \chi^2_{crit.}$ ($\alpha = .05$, df $= 3$)

Average diameter vs. distance to the nucleus The outcome of Friedman's test, summarised in Figure 7.12 shows that the computed χ^2 (6.884) is strictly less than $\chi^2_{crit.}$ ($\alpha = .05$, df $= 3$), that is 7.815. Therefore, the null hypothesis is not rejected and it can be claimed that the average diameter does not vary significantly with distance to the nucleus. Furthermore P_{value} (0.0757) exceeds the declared value that is 0.05 and there is, accordingly, no difference in the average diameter at the four locations at this level of significance (0.05). So differences in mean average diameters at the four locations are due only to chance.

Average length vs distance to the nucleus Friedman's test for edge lengths, Figure 7.13 on page 125, also shows that the computed χ^2 (1.185) is strictly less than $\chi^2_{crit.}$ ($\alpha = .05$, df $= 3$), that is 7.815. The null hypothesis is not rejected and

Source of Variation	SS	df	MS	χ^2	$P_{value} > \chi^2$	$\chi^2_{crit.}$
Columns	41.478	3	13.826	1.185	0.757	7.815
Interaction	2728.922	66	41.347			
Error	12522.1	368	34.027			
Total	15292.5	459				

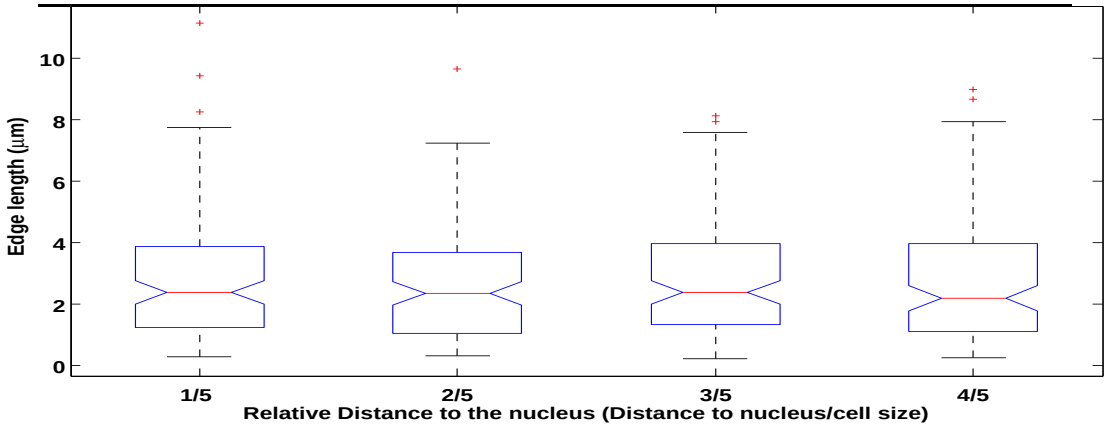

Figure 7.13: Edge length vs. distance to the nucleus and the corresponding Friedman test results showing that the edge length does change significantly with distance to the nucleus $\chi^2 < \chi^2_{crit.}$ ($\alpha = .05$, df $= 3$)

we can claim that the average diameter does not vary significantly with distance to the nucleus. The P_{value} (0.757) exceeds the declared value, 0.05, which suggests that there is no difference in edge lengths at the four locations at this level of significance.

Surface area vs distance to the nucleus Friedman's test for edge surface area vs distance, Figure 7.14 on page 126, also shows that the computed χ^2 (4.048) is strictly less than $\chi^2_{crit.}$ ($\alpha = .05$, df $= 3$), i.e. 7.815, The null hypothesis is not rejected and we can claim that the average diameter does not vary significantly with distance to the nucleus. The P_{value} (0.256) exceeds the declared value, 0.05, so there is no difference in edge surface areas at the four locations at this level of significance (0.05).

Volume vs distance to the nucleus Friedman's test for edge volume vs distance, Figure 7.15 on page 126, also shows that the computed χ^2 (5.9) is strictly less than $\chi^2_{crit.}$ ($\alpha = .05$, df $= 3$), i.e. 7.815, The null hypothesis is also not rejected and we can

Source of Variation	SS	df	MS	χ^2	$P_{value} > \chi^2$	$\chi^2_{crit.}$
Columns	141.683	3	47.228	4.048	0.256	7.815
Interaction	3042.417	66	46.097			
Error	12110.4	368	32.909			
Total	15294.5	459				

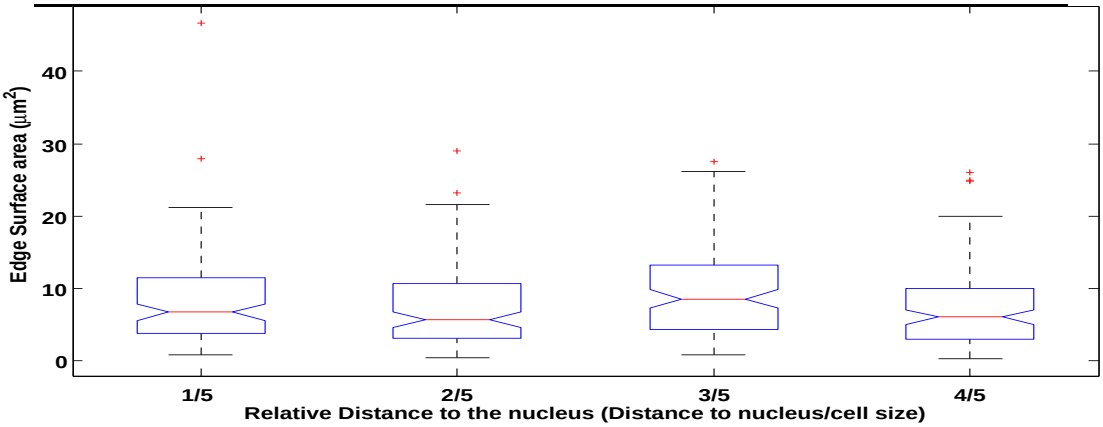

Figure 7.14: Edge surface area vs. distance to the nucleus and the corresponding Friedman test results showing that the edge surface area does change significantly with distance to the nucleus $\chi^2 < \chi^2_{crit.}$ ($\alpha = .05$, df $= 3$)

Source of Variation	SS	df	MS	χ^2	$P_{value} > \chi^2$	$\chi^2_{crit.}$
Columns	206.430	3	68.810	5.900	0.117	7.815
Interaction	3342.570	66	50.645			
Error	11742	368	31.980			
Total	15291	459				

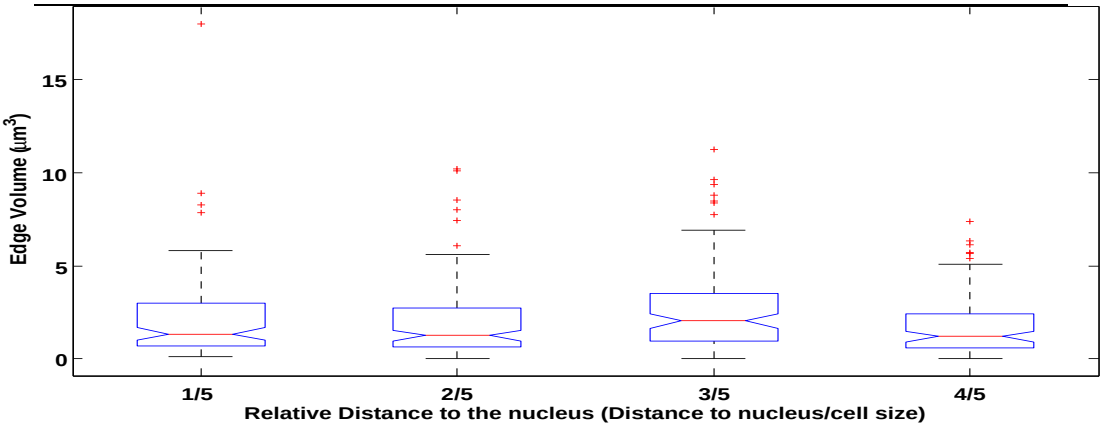

Figure 7.15: Edge volume vs. distance to the nucleus and the corresponding Friedman test results showing that the edge volume does not significantly change with distance to the nucleus $\chi^2 < \chi^2_{crit.}$ ($\alpha = .05$, df $= 3$)

claim that the edge volume does not vary significantly with distance to the nucleus. The P_{value} (0.117) exceeds the declared value, 0.05, so there is no difference in edge volume at the four locations at this level of significance (0.05).

In summary there are no significant differences in the four parameters at the four locations at 0.05 significance level. Table 7.1 on page 127 and Table 7.2 on

Table 7.1: Edge parameters (D_e: average diameter, L_e: length, S_e: surface area, and V_e: volume obtained using the average usable threshold value)

	D_e (μm)	L_e (μm)	S_e (μm^2)	V_e (μm^3)
μ	**0.87**	**2.78**	**7.53**	**1.81**
Min	0.24	0.26	0.26	0.02
Max	2.25	8.98	26.04	7.36
Var	0.13	4.14	31.21	2.56
σ	0.36	2.04	5.59	1.6

page 127, summarising the averages suggest that the solid ER can be modeled by a network made up of spheres (with an average diameter of $2.0\mu m$) connected by cylinders of nearly half diameters (0.96μm). The volume and surface area of a cylinder with length l and diameter d are given by $V = \pi(d/2)^2 l$ and $S = 2\pi(d/2)l$ respectively.

Assuming the branches of the ER are cylindrical, the average diameter of a branch can be obtained by dividing its volume by its surface area $d = 4V/S$. Replacing the values of V and S with the mean values of V_e and S_e taken from Table 7.1 on page 127, we get $d = 0.96\mu m$. Table 7.1 also shows that the average diameter of a branch using distance maps is $0.87\mu m$. The difference between the two calculations $0.96 - 0.87 = 0.2\mu m$ is less the width of a voxel. This shows that the ER branches are cylindrical in shape.

The respective undirected weighted graphs G representing the ROIs of the different

Table 7.2: Vertex parameters (S_v: surface area, V_v: volume, and Deg_v: degree obtained using the average usable threshold value (16))

	S_v (μm^2)	V_v (μm^3)	Deg_v
μ	**3.21**	**1.13**	**3.07**
Min	0.33	0.01	3
Max	10.98	9.61	4
Var	3.94	2.18	0.01
σ	1.98	1.48	0.3

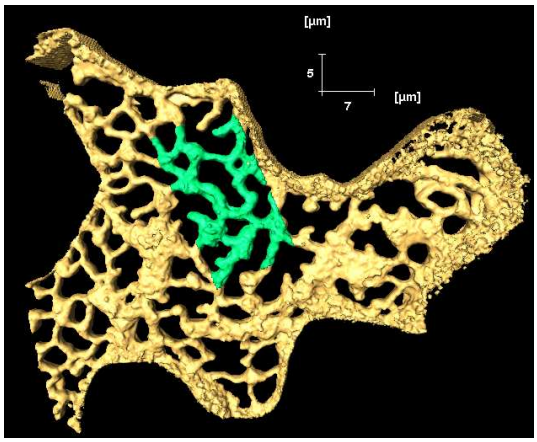

(a) Cell 1 (Threshold value 11)

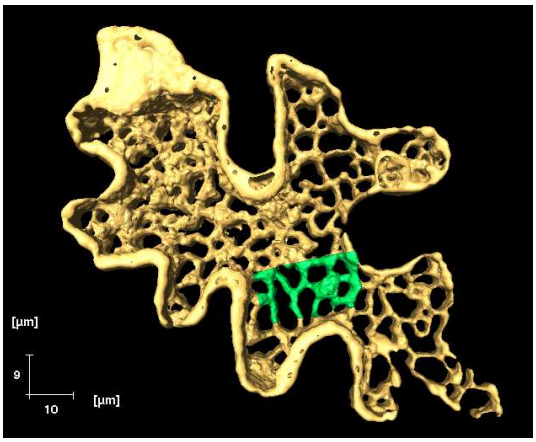

(b) Cell 2 (Threshold value 11)

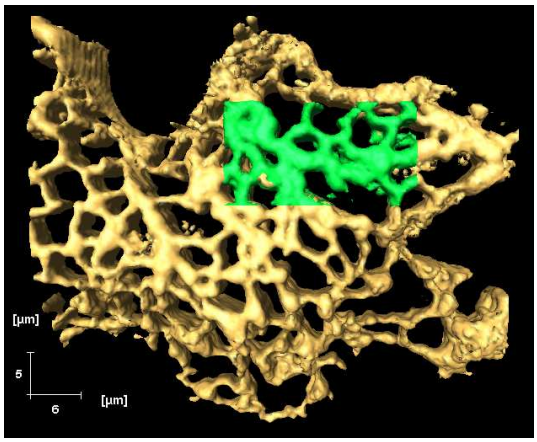

(c) Cell 3 (Threshold value 11)

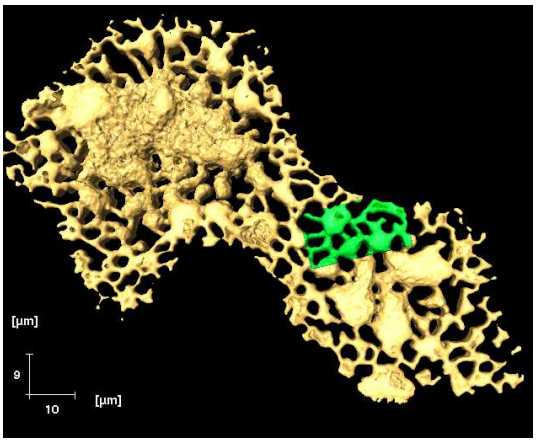

(d) Cell 4 (Threshold value 11)

Figure 7.16: Cropped regions of cortical plant ER near the cell wall, samples 1 to 4

ER samples are illustrated in Figure 7.17 on page 129. In these figures the solid ER is represented in terms of edge lengths. Similar graphs representing the solid ER with the edges' outer surface areas and volumes can also be obtained.

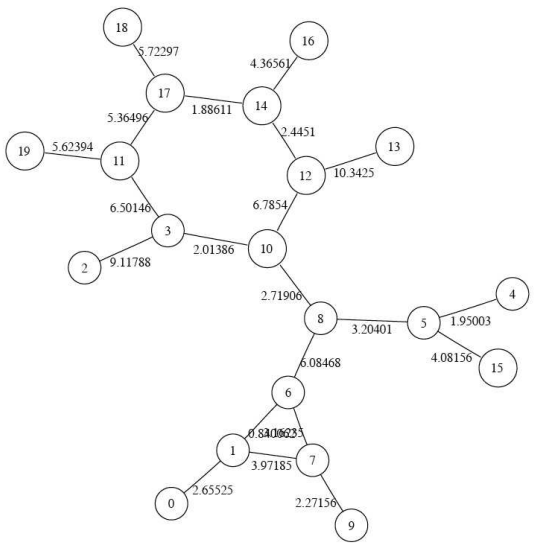

(a) Sample 1

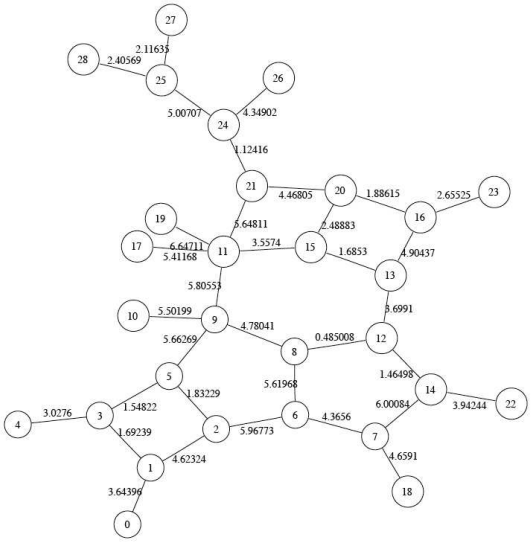

(b) Sample 2

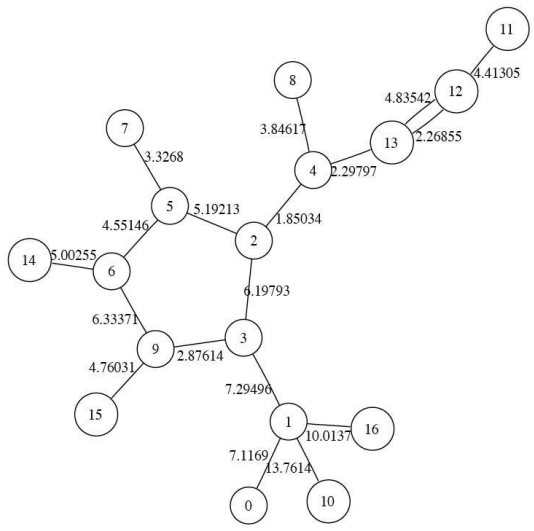

(c) Sample 3

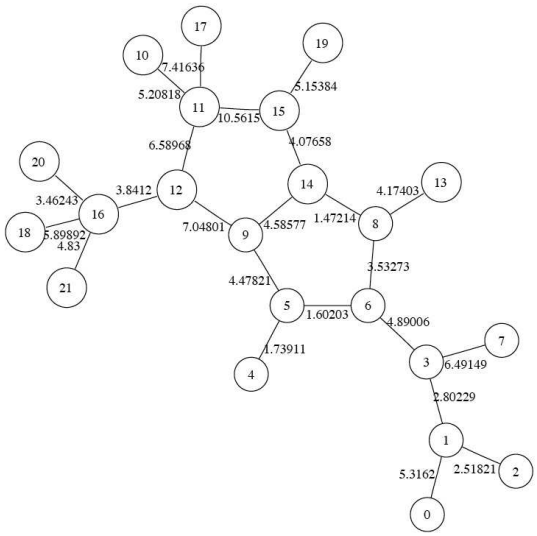

(d) Sample 4

Figure 7.17: The solid ER network of different samples ((1) - (4)) is represented in each case as an undirected weighted graph G with weights representing the length of edges. The integers in the nodes are an arbitrary ordering of the vertices (nodes).

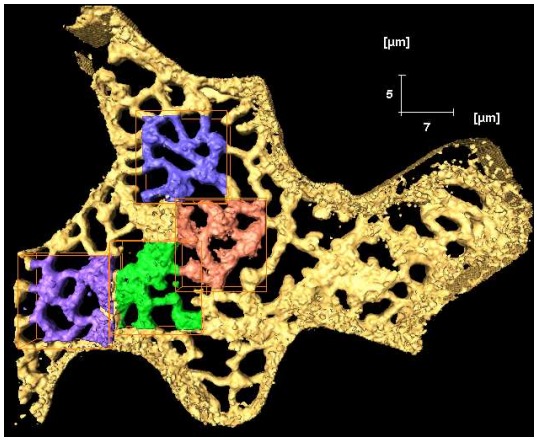

(a) Cell 1 (Threshold value 11)

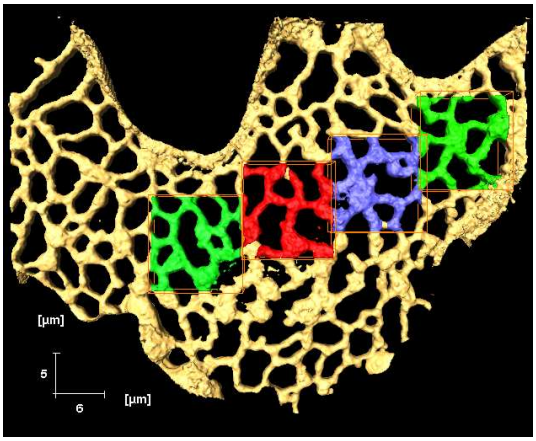

(b) Cell 2 (Threshold value 11)

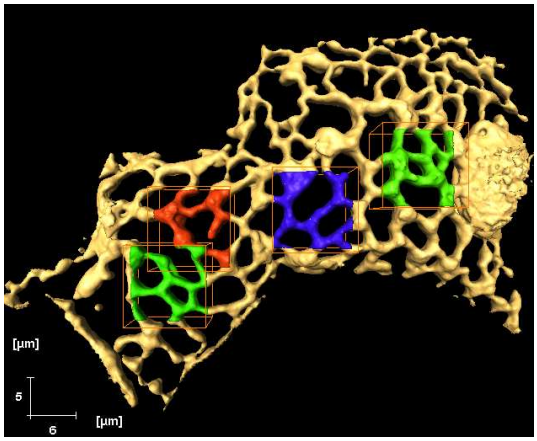

(c) Cell 3 (Threshold value 11)

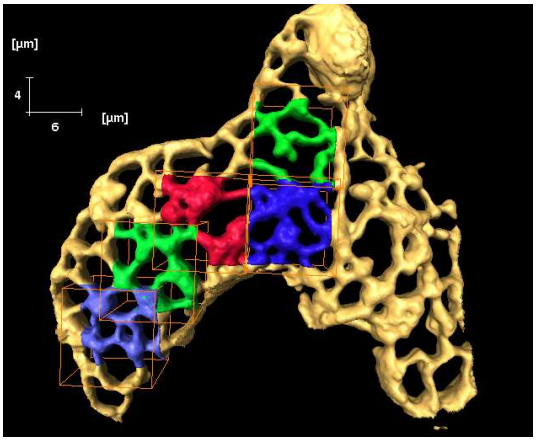

(d) Cell 4 (Threshold value 11)

Figure 7.18: Cropped regions of the plant ER starting from the nucleus and extending out to the cell wall samples 1 to 4

7.4 Discussion

Image analysis of confocal images relies on thresholding boundary grey values in the calculation of surface areas and volumes. The thresholds chosen in this chapter have been such that the original confocal pictures showed the same homotopy type as the extracted skeletons. But as this holds for a range of threshold values certainly the surface and volumes calculated for the plant ER would differ in a certain range. This is another motivation to introduce the graph structure, as the geometric invariants established with the graph are not dependent on the threshold value for the surface boundary as long as the ER stays connected and holes are not filled by choosing the threshold too low or too large. These invariants are also not dependent on any movement of the sample during data retrieval. The graph weights nevertheless also do make sense as they establish valid relative quantities for comparison between samples. Absolute values if needed could be estimated through measuring the point spread function and then deconvolving the final image. In fact even by using deconvolution, anisotropy in space remains and does not completely resolve the problem. Here it should be noted that every specimen might have slightly different optical properties, and the results of this chapter on surfaces and volumes do heavily rely on the assumptions that these conditions differ minimally from one specimen to another.

The main advantages of our approach are its simplicity and speed. We can easily vary different parameters such as digital image filter kernel sizes, and the threshold value for detecting sample boundaries. We also mostly rely on quantities that are largely independent of the errors mentioned above, such as the degree distribution of the skeleton (the graph associated to the solid ER) and the length of arcs (edges).

We like to give a motivation of this work relevant for cell biologists. Confocal microscopy opens new ways of discovering the interplay of form and function in

cellular structures. Many results of outstanding biological importance retrieved from different microscopy images are relying on pure visual inspection, even so this is often hidden in publications. This chapter makes a contribution in changing biological imaging into a more quantitative discipline, where finally physiological changes and their consequences captured by the image can be accurately described in terms of relevant quantities of a mathematical object attached to each image. Here the degree distribution are important quantities corresponding to the connection structure of the graph, and so influence the pathway a protein or protein complex could use to pass from location a to b. It also determines how close a part of an ER membrane is approaching any chosen volume or organelle in the cytosol. In general this is the underlying idea of a network structure, like a road system. The degree distribution itself is biologically connected to the question how the ER membrane system can remodel itself.

In general every mathematical model is an abstraction. In this chapter we abstract an entity associated typically to networks, i.e. a graph. In one interpretation (our generic one) the nodes (vertices) correspond to cisternae, the tubules to the edges (links). We are able to quantify how many such structures exist in a certain volume, and how they are typically connected. The chapter gives the basis of quantification in a new way; it does itself not discuss any function. Investigation of function is planned as future work. With the given approach we will for example be able to measure how efficiently proteins or other larger complexes will be able to spread along the network, a major property creating ER function.

In this study we tried to quantify the solid ER network geometrically using confocal microscopy; which is subject to a list of limitations including (a) the resolution limitations in confocal microscopy due to diffraction. A point source, under a confocal microscope, appears as an Airy Disk whose radius depends on the wavelength and Numerical Aperture (NA) of the objective lens. The size of the Airy disk dictates

the best reachable resolution and the scale of resolvable details. (b) The strength of optical sectioning requires small pin holes, but at the same time may lead to reduced signal-to-noise ratio due to the reduction in the number of photons arriving at the detector from the specimen. A good approximation can be obtained by making the size of the pinhole about the size of the Airy disk. (c) The pinhole size and the optics preceding it reduce the emission that reaches the detector which make its sensitivity and the noise behaviour very important. The accuracy of measurements can be improved by increasing the number of photons arriving at the detector, which can be reached by the intensity of the fluorescence signal or averaging data from many frames. (d) The chemical environment of the specimen may alter the position of the peaks of the excitation and emission of the spectra, see Semwogerere & Weeks (2005). (e) A sufficiently clear retrieval of solid ER geometry can currently only be obtained for cortical solid ER which is relatively flat and close to the cell wall. (f) In addition to these limitations, our calculations are subject to many errors, the majority of which were addressed in the previous section. They include (a) errors related to artifacts in the confocal microscope, (b) errors related to threshold as discussed, (c) errors related to cropping, (d) errors due to the filtering process, (e) errors due to noise, (f) errors due to triangulation, (g) errors due to thinning, (h) error due to z-resolution and finally (g) we acknowledge the error due to the unmatched refractive indices, sample mounted in water using oil immersion objective ($NA = 1.3$), which results in the axial displacement (Sheppard & Török, 1997) meaning that the nominal values measured in the axial direction are biased.

8

Quantification of the Dynamic ER

Besides the importance of the form of the ER and its relation to possible functions inside the cell, its dynamic behaviours are observed more and more with the help of improved microscopy techniques. This chapter introduces different measures of changing shapes of the plant ER in order to obtain a precise terminology combined with attached quantities. It introduces, and quantifies different dynamic properties of the plant ER (under standard physiological conditions) by applying image analysis techniques to confocal data.

8.1 Introduction

Time series acquired by confocal microscopy allow the appreciation of the dynamic nature of the cell compartments. According to Nebenfuhr *et al.* (1999), the ER exhibits an extraordinary heterogeneity in its morphology, and dynamic behaviour, that sets it apart from other cellular organelles whose movement is easier to track (see Figure 8.1 on page 137)

Morphologically the ER, observed by a confocal microscope, contains highly mobile regions that randomly remodel and appear to contain a dynamic flux of proteins. The rules that control the remodelling and reshaping of the tubular network are currently obscure. Unlike the mammalian ER, the plant ER is attached, not to microtubules, but to actin filaments, see Boevink *et al.* (1998). It is therefore predicted that specific myosin isoforms mediate this interaction.

This remodelling occurs through the formation and/or disappearance of tubules in very short time scales (fractions of a second); Lee & Chen (1988) reports that new mammalian ER tubules (those which correspond to points in the skeleton with one neighbour) extend from the network with an average velocity of $1.15 \mu m/sec$ ($+/- 0.33$ SD, $n = 29$). This topological heterogeneity is believed to be related to its functional diversity.

To analyse the movement of the ER, this chapter observes untreated, i.e. actin cytoskeleton intact, ER samples using confocal microscopy and image analysis. It extends the investigation in Chapter 7 further by providing the variations of the four introduced parameters with time and introduces new parameters: the average speed of a junction, and its maximum displacement as defined in Chapter 5 and Chapter 6.

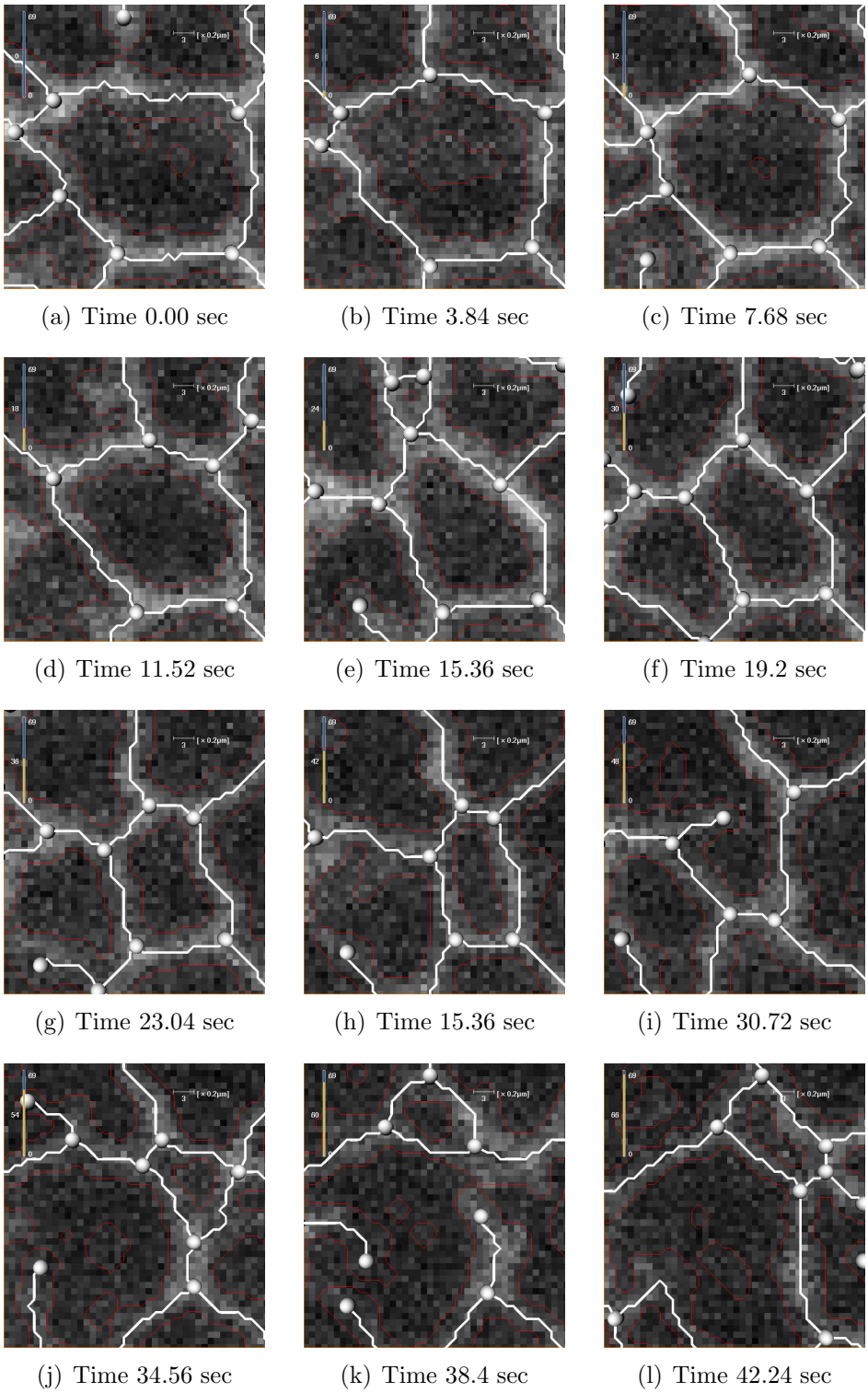

(a) Time 0.00 sec (b) Time 3.84 sec (c) Time 7.68 sec

(d) Time 11.52 sec (e) Time 15.36 sec (f) Time 19.2 sec

(g) Time 23.04 sec (h) Time 15.36 sec (i) Time 30.72 sec

(j) Time 34.56 sec (k) Time 38.4 sec (l) Time 42.24 sec

Figure 8.1: An illustration of the remodelling of the ER: images of the ER of a *Nicotiana tabacum cv* Petit Havana SR1 cell and the corresponding skeletons taken at different time steps. The skeletons were obtained by applying the Amira distance ordered homotopic thinning algorithm and chamfer maps (see Fouard *et al.* (2006)), the junctions are represented by circles of known radii (scaled to 2.5). The red contours represent the boundary between the foreground (the fluorescence of the GFP in the ER) and the background (the cytosol) of the cell. Scale bar (top right) $0.6\mu m$, and time bar represents 69×0.64 sec.

8.2 Assumptions

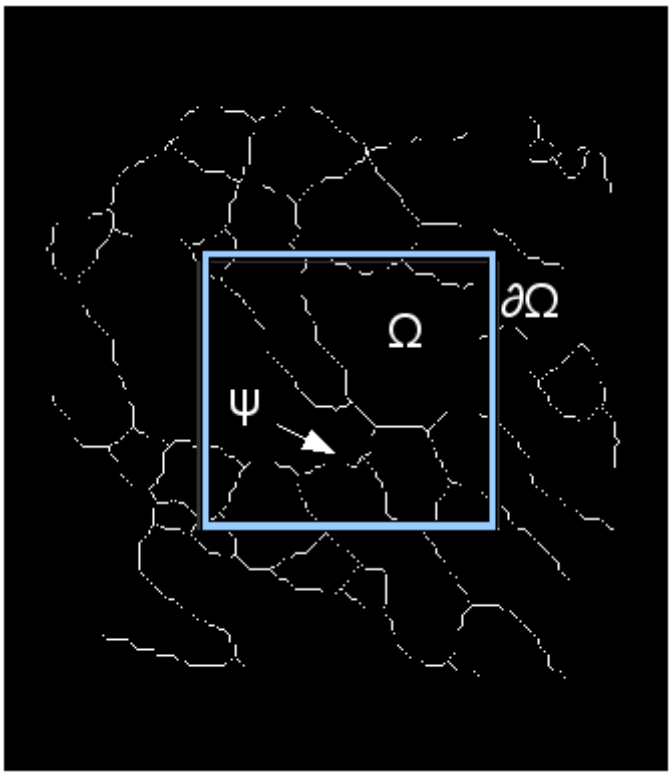

Figure 8.2: The square ROI (of size $12.78\mu m \times 12.78\mu m$) is cropped from the image ($25.57\mu m \times 25.57\mu m$) of the skeleton of the ER, and is denoted by Ω. Its boundary is denoted by $\partial\Omega$. The skeleton inside Ω is denoted by Ψ. All calculations are related to Ψ.

Since the ER is a single connected network of tubules and sheets (see Section 2.1 on page 8), it is possible for a protein to travel between any two points in the reticulum without leaving it. This is an important criterion for the validity of the image analysis chain described in Chapter 4 and Chapter 5.

Let $\mathcal{I}$ be the image of the skeleton of an ER specimen, from which a ROI Ω with boundary $\partial\Omega$ is cropped, and let skeleton Ψ be the part of the specimen skeleton which belongs to Ω (see Figure 8.2 on page 138). Since Section 2.11 on page 23 has stated that the ER is a connected network, Ψ can either be connected or it may contain isolated parts that emerge from $\partial\Omega$ (due to cropping). The third scenario, where the isolated parts do not intersect $\partial\Omega$, is not physiological because it implies that the ER is disconnected (which contradicts the initial observation). It may

sometimes however appear disconnected due to (a) out-of focus branching, (b) weak fluorescent signals, or (c) noise and artifacts.

In fact, it is not possible that case (a) is the reason since images were acquired in such a way that the topmost and bottommost focal planes lie completely outside of the ER. This leaves only the remaining two cases; but, regardless of the reason, any disconnected skeleton has to be discarded. As a result, in addition to the constraints described in Chapter 4, skeletons have to be connected to be considered for analysis. The ER is highly dynamic and its constant remodelling depends on its attachment to underlying cytoskeletal structures.

The ER network actively re-arranges itself in several forms, namely (a) elongation, (b) retraction, and branching of tubules, (c) sliding of junctions, (d) closing and formation of loops. Elongation, retraction, and branching refer to the movement of ER tubules, including their growth or shrinkage. Loop closing is related to the fusion of the ER membrane system with itself, where a tubule head merges with a tubule of the ER to create a new connection in the network. Understanding these mechanisms may provide biologists with further clues about the form-function relationship.

Independent of the detailed mechanisms causing the observed ER movement and/or the events involving membrane fusions (topological changes), we introduce different time-dependent quantities, which we believe are well suited to characterise the changing dynamic behaviour with respect to shape changes of the plant ER.

The majority of the quantities introduced in this chapter are extensions of the static ER analysis discussed in Chapter 7. In particular we discuss the following list of observables during a time interval $[0.00sec, 122.88sec]$ in a fixed 2-D ROI of size $17 \times 17\ \mu m^2$. There are both discrete and continuous quantities in this list, all functions of time. The goal is to monitor these quantities with time, i.e. interpret them as functions of time.

In the case of discrete quantities we interpret changes as events, and we are interested in how often such events occur (which is related to how 'dynamic' the ER movement is in a certain period of time). These quantities include: (a) ER skeleton length (continuous), (b) ER surface area (continuous), (c) ER volume (continuous), (d) number of nodes in the ROI (discrete), (e) number of edges in the ROI (discrete), (f) average degree (graph concept, excluding artificial boundary nodes) and degree distribution, (g) membrane fusion events, and (h) average velocity and direction of movement of nodes (node tracking).

8.3 Material, methods, and coding

This chapter follows the methods described in Section 3.2 on page 29. We wrote Matlab programmes to automate prefiltering, enhancing and thresholding images and combined these with Tool Command Language (TcL) scripts, using *Amira 4.1.2* Zuse (2006), to obtain the network skeletons at each time step. We also developed C++ programmes to associate degrees, lengths, surface areas, and volumes to the corresponding edges/nodes. Finally we extended Sbalzarini & Koumoutsakos (2005) java code to monitor and analyse the movement of the network.

8.3.1 Key background information

We collected $25.57\mu m \times 25.57\mu m$ time series images from 30 different cells, and from each of these images we selected a planar sample of size $12.78\mu m \times 12.78\mu m$ in a region half way between the nucleus, and the cell wall. On the basis of the observations of the results of Chapter 7, and throughout this chapter, we assume that the network can be modeled by cylinders (branches) connected with spheres (junctions). The samples were mounted in water and visualised with a Leica TCS

SP5 confocal scanning microscope using a 63× oil immersion objective ($NA1.3$). GFP was excited at 488 nm and visualised with an emission window of 500-530 nm. Optical sections were acquired with a z step size of 0.2 μm, matching the x-y pixel size (voxel-width = voxel-height = voxel-depth = 0.2 μm). Each specimen contained 20 z-sections. The pinhole size was set to 1.0 AU (178 μm), the scan speed to 400, the frame-average to 1, and the line-average to 2. There were 8 bits per sample and the zoom was set to 2.32.

8.3.2 Image analysis

The approach this chapter follows consists of two parts. It starts by de-noising individual images, performing intensity maximum z projection (to guarantee connectivity), obtaining skeletons of individual images, and finally isolating nodes in each skeleton. It then monitors the remodelling of the skeleton with time by recording the distribution of nodes throughout the movie using the algorithm proposed by Crocker & Grier (1996) and later enhanced by Sbalzarini & Koumoutsakos (2005).

The reason for choosing this algorithm is that it does not rely on any prior knowledge of the kind of movement of feature points (vertices); this is important since we do not have any idea why the ER junctions move. Furthermore, it has proven to be fast, efficient and accurate; see Sbalzarini & Koumoutsakos (2005).

As already explained in Section 5.2 on page 85 the algorithm consists of four steps (1) image restoration (2) followed by the estimation of point locations, then (3) the refinement of these locations, and finally (4) non-particle discrimination. The first step corrects for long-wavelength modulations of background intensity and discretisation noise from the digital camera. The second is achieved by finding local intensity maxima in the restored image where only the brightest pixels within a given distance that lie in the upper r^{th} percentile in the current frame are taken. In

step 3 the algorithm assumes that the found local maximum is near the true geometric centre of the detected point. The final step rejects spurious detections based on intensity moments of orders 0 and 2 where it is assumed that the correctly detected observations are those which form a dense cluster in the (m_0, m_2) plane. It is also assumed that the distribution of these points is a 2D Gaussian. Every detected point is given a score calculated from the contributions of all the other points. A point is kept only if it has a score that is above a given threshold. Details of the algorithm can be found in Crocker & Grier (1996) and Sbalzarini & Koumoutsakos (2005)

Pre-filtering using the median filter

To balance between noise reduction and preservation of as much information as possible in the original images, this chapter uses a median filter due to the heavy presence of salt and pepper noise in the original data. In order to keep as close to the original data as possible, we use the smallest possible kernel for the median filter (3×3). Thee main advantage of this filter is that it closes non-biological holes and removes isolated pixels. This is in contrast with the median-Gaussian smoothing chain described earlier in Chapter 7.

Contrast Limited Adaptive Histogram Equalisation

A common characteristic of confocal micrographs is that only the portions of the sample that are in the focus plane will show the signal (GFP in our case); so in order to obtain clear 2-D images of the ER it is usually necessary to scroll through the sample to find a portion that is aligned in the plane of focus. Even so signal strength might vary from one part of the image to another either because the ER does not lie completely in the same z-plane. To even out the distribution of used

grey values, make hidden features of the ER more visible, and more importantly to simplify the background removal operation, this chapter follows the above median filter operation by a Contrast Limited Adaptive Histogram Equalisation (CLAHE) enhancement step (described in Reza (2004)).

CLAHE partitions an image into smaller regions and applies a histogram equalisation to each one in turn. So rather than working on the entire image, CLAHE operates on partial contextual regions in the image. Each region's contrast is enhanced, so that the histogram of the output region approximately matches the histogram specified by a certain 'Distribution' (this thesis uses Rayleigh distribution because it yields 2 bell shaped histogram populations, which will come in handy in the next step). The method then combines the neighbouring regions using bilinear interpolation in order to eliminate artificially induced boundaries (see Reza (2004)).

Local Adaptive Background removal

In order to take into account local variations of the image grey levels, this section applies the state of the art Sauvola local adaptive thresholding technique to the denoised image. Sauvola treats the image as a set of inter-connected regions, windows of size $w \times w$ centred around pixel p(x,y), and associates a different threshold value to each one in turn, taking into account the local mean $\mu(x, y)$ and local variance $\sigma^2(x, y)$ of the pixel $pixel(x, y)$ intensities (Shafait *et al.*, 2008):

$$T(x, y) = \mu(x, y) \times [1 + k \times (\frac{\sigma^2(x, y)}{R} - 1)], \tag{8.1}$$

where R is the maximum value of the standard deviation (127.5 in our case) and k is a parameter in the range $[0.2, 0.5]$. This chapter sets $k = 0.34$ according to Shafait *et al.* (2008)

In contrast to the mean local adaptive background removal method, where only the

mean is taken into account, Sauvola also takes into account the local variance (the former can be obtained by setting $k = 0$ in Equation 8.1). This is another vital step to highlight details (holes) and avoid false edges (very close edges). The smaller the window size the more details we get. To improve the speed and efficiency of computations, this chapter uses integral and square images (that can be obtained by a single pass). The implementation of this part in Matlab yields much faster results, compared to normal implementation. Finally repeating the above steps (starting from the median filtering) until isolated pixel aggregates completely vanish yields an optimal binary image (usually obtained after 3 iterations). Figure 8.3 on page 145 illustrates the previous steps.

Clustering-Based Thresholding

Applying CLAHE and removing the background yields two distinct cluster populations, which have Gaussian histograms: a foreground and a background. Sezgin & Sankur (2004), suggested using the Minimum Error Global Thresholding (MEGT) method proposed by Kittler & Illingworth (1986) where the "safe" assumption that the image histogram contains two Gaussian distributions is exploited to turn the thresholding issue into a minimisation problem. This method scored best among 40 other thresholding techniques according to Sezgin & Sankur (2004)'s criteria. MEGT has, however, its drawbacks. First, it operates on the entire image and does not take into account the non-uniformity of the signal across the image. Second, it assumes that it is possible to separate between the pixel populations in the image by looking at their histogram distributions. Third, their survey was mainly based on non-destructive binarisation of old documents. Fourth, it heavily depends on the initial value which makes it user dependent. We found that by varying the initial value we get conflicting results especially at the end points of the range. These drawbacks turn our attention to clustering-based approaches, where we split

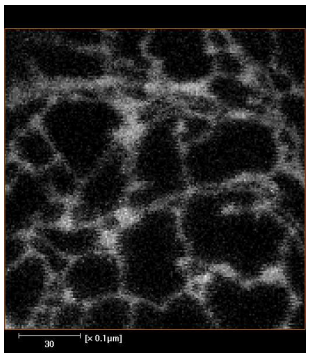

(a) Original image

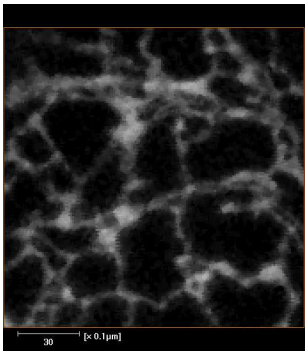

(b) Median after iteration 1

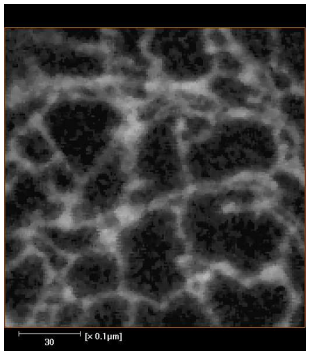

(c) CLAHE after iteration 1

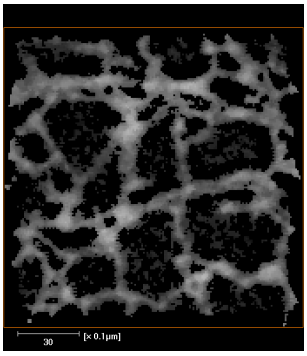

(d) Result after iteration 1

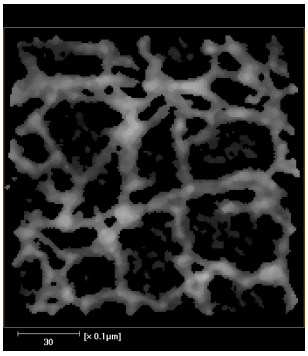

(e) Median after iteration 2

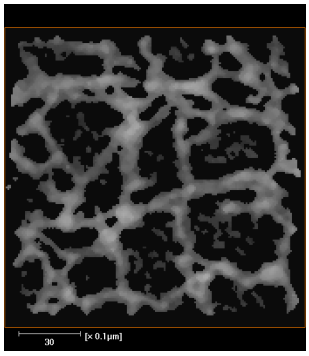

(f) CLAHE after iteration 2

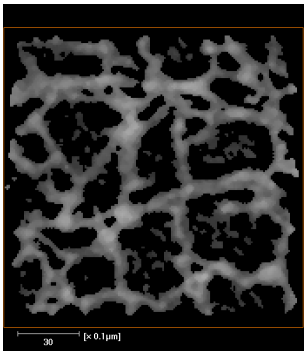

(g) Result after iteration 2

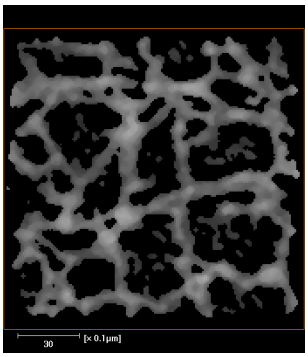

(h) Median after iteration 3

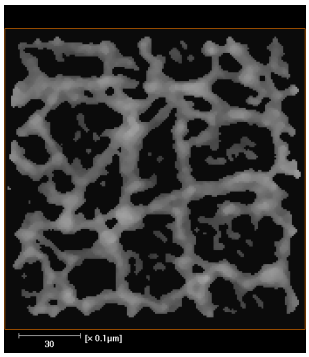

(i) CLAHE after iteration 3

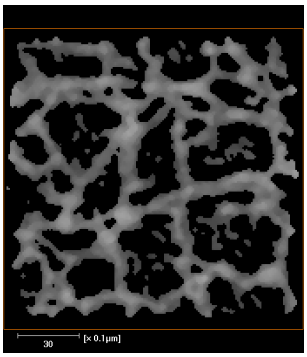

(j) Result after iteration 3

Figure 8.3: An illustration of the dynamic ER pre-processing steps: (a) the original image (b) image after applying the median filter, (c) the image after applying CLAHE, the remaining figures represent the second and third iterations. Scale bar $3\mu m$

grey-level data into two clusters corresponding to foreground and background and search for the midpoint of their peaks. Although simple, we demonstrate that it is an efficient way, at least in our case, to automatically separate between foreground and background.

Skeletonisation

In a similar way to the approach followed in Chapter 7, this chapter calculates the skeleton of the ER and associates the 3D geometric parameters to it, then observes their variation with time. As already mentioned in Section 4.5 on page 63, there are several skeletonisation algorithms to choose from and the most convenient to the kind of data of this chapter is the Euclidean Sequential voxel based thinning algorithm that is based on distance transforms and chamfer maps (which are good approximations to the Euclidean distance and are faster) due to the fact that it produces thin, homotopic, and centralised skeletons. Faster and more efficient methods, such as skeleton extraction by mesh contraction, Au *et al.* (2008) were avoided because of (1) time constraint (2) this is not the aim of this investigation and (3) most importantly, they produce the same results. We write the skeleton in a geometric form (points) rather than volumetric form (voxels). In addition to the constraints of the Distance Ordered Homotopic Thinning algorithm this chapter enforces the following additional constraints on the skeleton to comply with the reported physiological properties of the ER:

- Deg(v) $\neq 2$ (we ignore inner vertices)
- Deg(v) $\neq 0$ (we ignore isolated vertices)
- Deg(v) $\geqslant 3$ (we allow vertices with degree 3 and more)
- We ignore edges/vertices that suddenly appear in the middle of the ROI (the

plant ER is assumed to be planar and connected, so an edge cannot appear from nowhere); but we allow those coming from any of its four boundaries.

Abstraction of the moving ER

The main advantage of representing the network by its skeleton lies in the simplicity and ease of quantification. At each time step i we represent the network by *a graph* $G_i = (V_i, E_i)$, where V_i and E_i are the sets of vertices, and edges (respectively) at time step i. Using this terminology we can easily compare, monitor, analyse and quantify the network changes over time. These changes can be used to characterise the dynamic behaviour of the ER. Using a graph can also be exploited in comparing the dynamics of the ER in different cell types (plants vs. mammals for instance). For a representative part of the ER we can analyse different geometric features such as the distribution of vertex degrees and the network cycle distribution over time. The given geometric invariants are not sufficient to recover other typical ER properties, like the typical sequence of broader structures (cisternae) and thinner pipes joining them. In order to get a relative picture of such characteristic geometric features we attach weights to the graph representing length of pipes (a weighted graph). According to the biological interpretation we also attach volumes to nodes representing cisternae in our graph abstraction. Skeleton abstraction plays a crucial role in the calculations to come. Figure 8.4 on page 148 summarises the steps followed to abstract the ER by a graph.

Vertex Tracking and Motion analysis

To avoid unnecessary complexities in motion analysis, this chapter uses the obtained graph (an image that only contains the skeleton's end points connected with straight lines). This is to avoid inherent complications in the problem of tracking such as

noise and false and spurious detections (see Crocker & Grier (1996)). This chapter highlights the graph vertices by circles of known radii to make tracking and motion analysis even simpler (not only do we know the position of a vertex at a certain frame, but we also know its size). The next step is vertex tracking, and it consists of two main tasks: (a) the detection of vertices in each frame, and (b) linking these points to reconstruct their trajectories. Vertex positions provide a wealth of information which can be used to quantify the motion of the ER. The following steps are based on the work of Crocker & Grier (1996) and Sbalzarini & Koumoutsakos (2005).

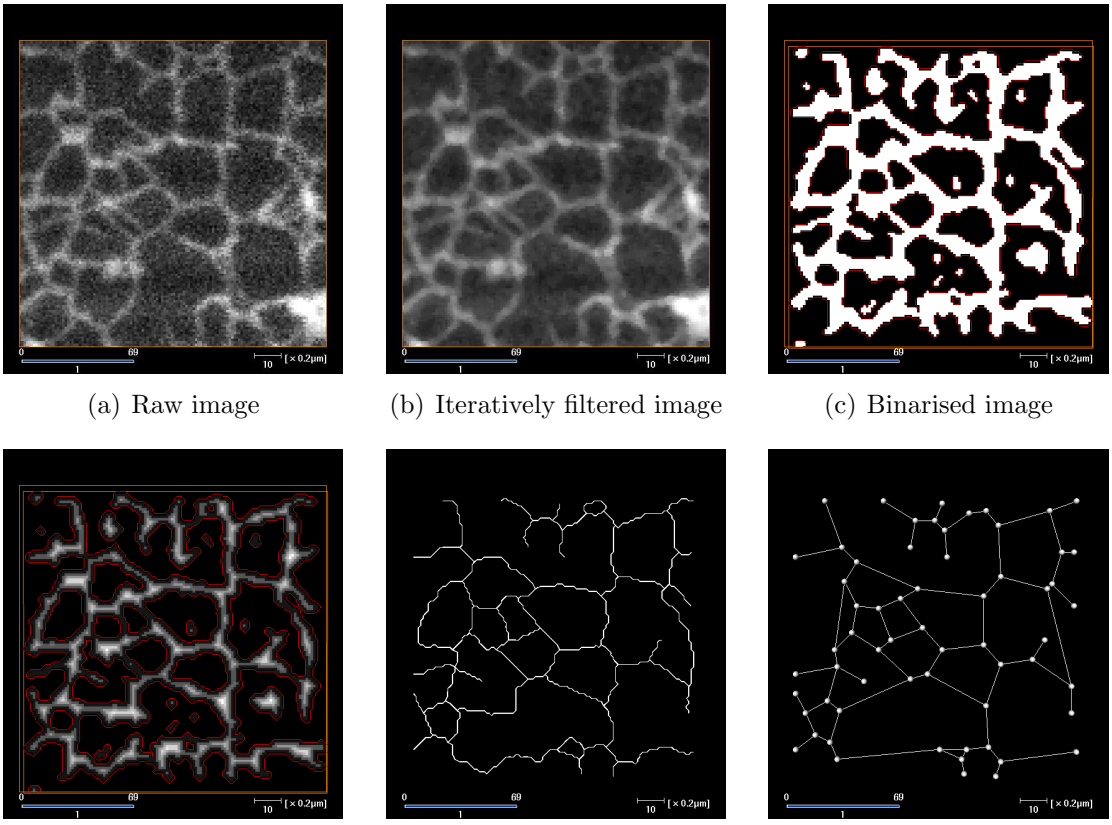

(a) Raw image (b) Iteratively filtered image (c) Binarised image

(d) Distance map (e) Skeleton (f) Simplified skeleton

Figure 8.4: An illustration of the steps followed to obtain the skeleton of the plant moving ER samples and the corresponding graph: (a) raw data, (b) the result of prefiltering using the 2D median filter (kernel 3×3), (c) the corresponding binary image using adaptive thresholding, (d) the corresponding distance map using chamfer distances (e) the skeleton obtained using the previous binary image and distance map,(notice the absence of the skeletons of isolated parts in the binary image), (f) the simplified skeleton (a graph). Scale bar represents $2\mu m$, and time bar represents $57.753sec$ (there are 69 time steps each time step lasts for $0.837sec$)

All that is needed in the case of this chapter are point locations. The point location detection step in the algorithm of Crocker & Grier (1996) is based on the intensity moments of order "0" and "2". The former (m_0) is defined as the sum of all pixel values within a local window of size (w), while the latter is given by

$$m_2 = \frac{\sum (i^2 + j^2) p(i,j)}{\sum p(i,j)},$$

where $p(i,j)$ is the pixel value at location (i,j). Crocker & Grier (1996) and Sbalzarini & Koumoutsakos (2005) base their algorithm on the assumption that the majority of the detected points correspond to real vertices if they form a cluster in the (m_0, m_2) plane and no vertex points lie outside. The cluster locus is identified by having each point "p" carry a 2D Gaussian. They consider a point as a real vertex only if it has a score above a threshold given by the sum of the contributions of all other points.

The linking algorithm finds points that correspond to the same vertex in subsequent frames and link their positions. This is achieved by finding a set of associations between point location matrices by minimising a certain cost functional. The cost functional can be expressed in terms of: (a) the sum of the quadratic distance between a point in a given frame and all the points in the subsequent frames (b) other physical quantities that differentiate the point from the others. These can be the intensity moments described above for example.

To calculate the displacements, velocities, and accelerations of the nodes, this chapter further simplifies the skeleton by removing the inner points in its edges leaving only end-points, i.e. vertices (see Figure 8.5 on page 150). It then represents these vertices by discs, with radii obtained from the calculated distance map transforms. The reason for this simplification becomes apparent when one tries to track the network. Rather than tracking a complex shaped network this chapter ends up tracking a set of discs as illustrated in Section 8.4 on page 153.

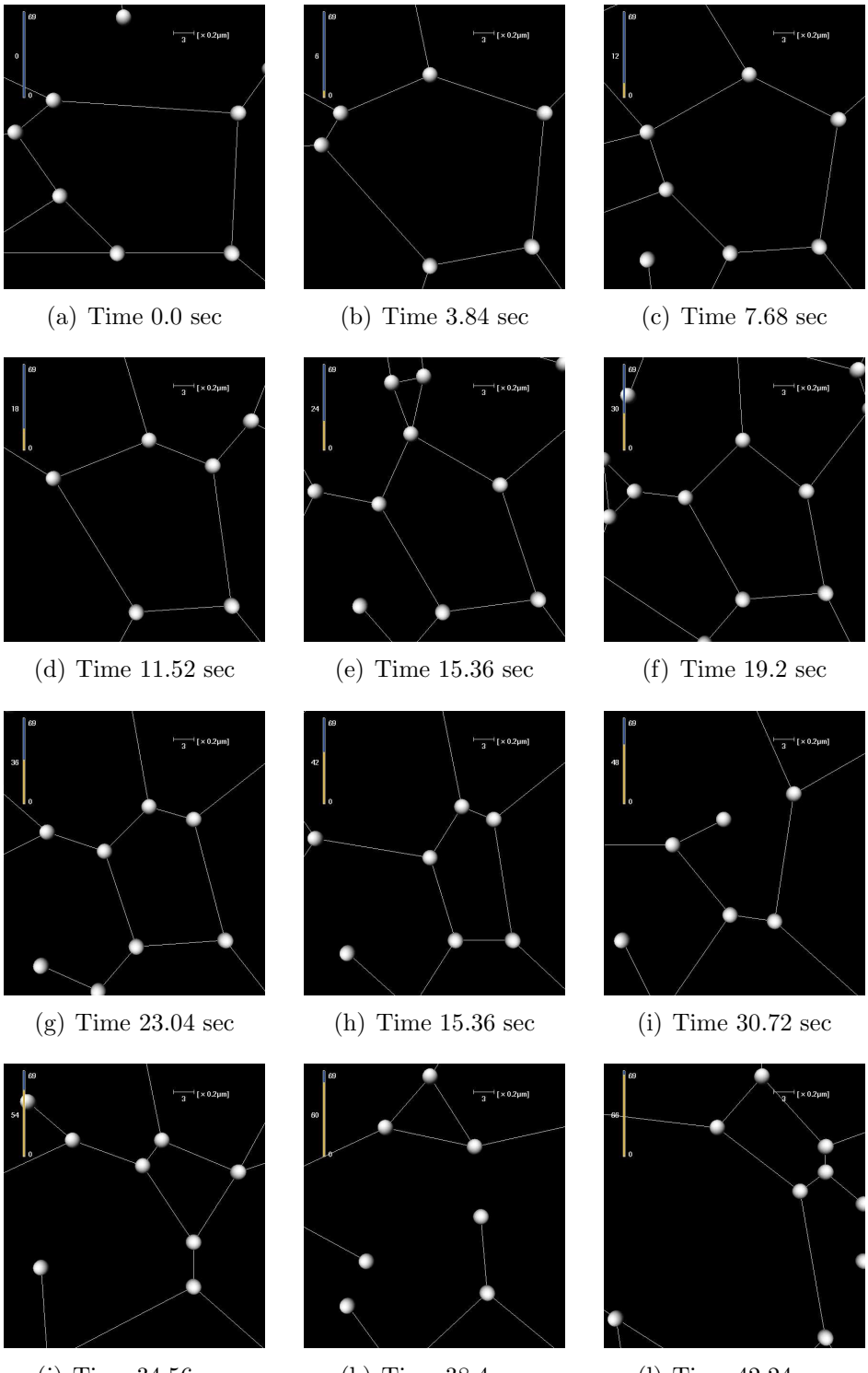

(a) Time 0.0 sec (b) Time 3.84 sec (c) Time 7.68 sec

(d) Time 11.52 sec (e) Time 15.36 sec (f) Time 19.2 sec

(g) Time 23.04 sec (h) Time 15.36 sec (i) Time 30.72 sec

(j) Time 34.56 sec (k) Time 38.4 sec (l) Time 42.24 sec

Figure 8.5: An illustration of the movement of the ER using graphs: the white circles represent the vertices and the straight line segments the edges. Scale bar (top right of each frame) $0.6\mu m$, and time bar $69.64sec$

Given a total set of T matrices with rows $[x_p, y_p]$ representing vertices detected in frame (t), we want to identify points that correspond to the same vertex in subsequent frames and link their positions. Linking the positions of these points means finding a set of associations between the point location matrices in different frames. This can be achieved by minimising a certain cost functional. The algorithm chosen to achieve this was implemented by Sbalzarini & Koumoutsakos (2005) and is based on the particle matching algorithm of Dalziel (1993, 1992), which uses the Graph theory technique introduced by Hitchcock (1941). We also include additional constraints to take into account physiological constraints (for example the connectivity of the network), concluded from our experimental observations.

Starting from frame t, in which there are N_t detected vertices which, denoted by p_i where $i = 1, ...N_t$, and considering R future frames, for all sets Ł$_r$. $r = 1, ..., R$ of points q_j where $j = 1, ..., N_{t+r}$, in frame $t + r$, the algorithm defines an association matrix G_r^t as follows:

$$G_r^t = g_{ij} = \begin{cases} 1 & \text{if } p_i \text{ in frame } t \text{ and } q_j \text{ in frame } t+r \\ & \text{are produced by the same vertex} \\ 0 & \text{otherwise,} \end{cases}$$

and the time evolution of the distribution of isolated vertices (their trajectories) is given by:

$$\rho(\mathbf{r}, t) = \sum_{i=1}^{N} \delta(\mathbf{r} - \mathbf{r}_i(t))$$

where $\mathbf{r}_i(t)$ is the location of the node i at time t. A reconstructed digital trajectory consist of an ordered series of point locations over time. Details of this algorithm can be found in Sbalzarini & Koumoutsakos (2005). Figure 8.6 on page 152 shows the trajectories of the junctions of the ER after $57.753sec$.

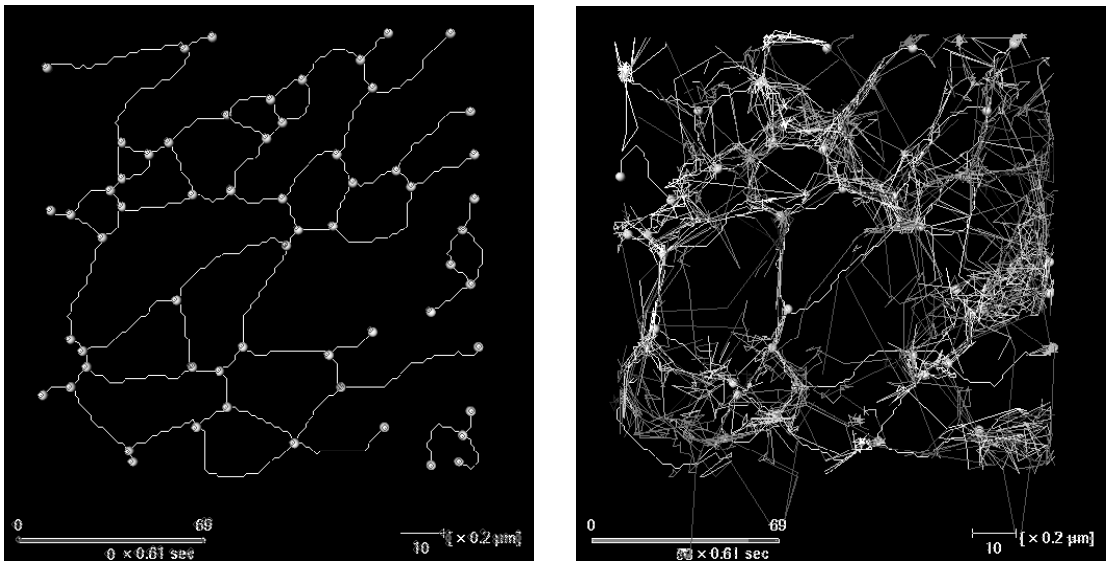

(a) Detected points at timestep 0 (b) All trajectories

Figure 8.6: Vertex tracking illustration (a) represents the vertices at time 0.0 sec, (b) shows the trajectories of these vertices after $57.753sec$. ROI size is $17 \times 17\mu m$, scale bar represents $2\mu m$, and time bar represents $57.753sec$ (there are 69 time steps and each time step lasts for $0.837sec$.)

8.3.3 The ER as an abstract dynamic geometric structure

At each time step, during time interval $[t_0, t_{end}]$, within a fixed ROI, this chapter calculates for each skeleton (a) its Euclidean length by summing the lengths of its segments, (b) the degrees of its vertices[1] (c) the diameter at each of its inner points using distance maps[2] and consequently (d) its surface area and (e) volume assuming that branches are cylindrical in shape Voeltz & Prinz (2007). The benefit of representing the reticulum by its skeleton becomes more apparent when trying to quantify its movement. Not only is the skeleton homotopic, medial, and thin, but it also conserves the homotopy type of the ER sample (see Chapter 4). A graph representation of the skeleton further simplifies the ER, by only conserving the positions of the end points in each edge and joining them by straight lines. At each time step i we represent the network by *a graph* $G_i = (V_i, E_i)$, where V_i and

[1] In *Graph theory* terms this is defined as the number of edges emerging from it,

[2] These are grey scale images where each point in the foreground is given the value of its distance to the closest point in the background,

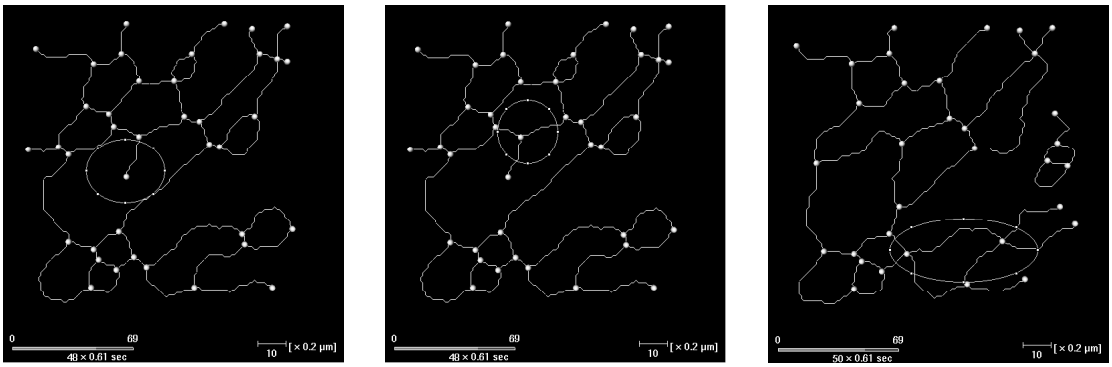

(a) (b) (c)

Figure 8.7: Types of junctions in the ER (vertices inside the white circles): (a) end point, (b) three way, and (b) four way junctions.

E_i are the sets of vertices, and edges (respectively). Using this terminology we can easily compare, monitor, analyse and quantify the network changes over time, and characterise the dynamic behaviour of the ER.

8.4 Results

As explained in Section 8.3.1 on page 140, this chapter obtained data from 30 different cells, and from each of these cells we randomly picked a set of useable planar samples of size $17\mu m \times 17\mu m$ in a region half way between the nucleus and the cell wall. 96 samples for 196 times steps were observed; each times step lasts 0.64 sec.

8.4.1 Types of junctions

The first observation this chapter makes is that there are three types of junctions in the specimens we observed (see Figure 8.7 on page 153): (a) the first type corresponds to end points in the skeleton, i.e. when the vertex in the skeleton has only one neighbour, (b) the second type is the most common type and corresponds to

three way junctions, i.e. when the vertex in the skeleton has three neighbours, (c) the third type is less frequent and takes place when a loop of the ER closes. It occurs when the nodes in a loop consisting of more than three nodes come gradually closer to each other while the loop gets smaller until all nodes disappear leaving only one node.

Although three way junctions are most common, Figure 8.7 on page 153 suggest that four (and above) way junctions can also occur. The "more than three way" junctions take place when the branches in a loop get shorter and shorter, till they melt together in one single junction. In theory it is possible to have "n-way" junctions when a loop consisting of "n" vertices closes.

Each edge consists of (a) two end points (vertices in graph theory terms) and (b) a collection of inner points (edge in graph theory terms). The former represent the junctions in the original ER sample, while the latter represent the branches. Connecting these end points with straight lines yields the corresponding ER graph (note that the positions of the vertices in the graph correspond to the junctions in the original ER sample). The simplified skeleton's main advantage is the simplification of tracking the vertices. So rather than tracking a whole edge, probably containing many vertices, we simply track its two end points.

It is important to note that in all calculations we discard edges which intersect the boundary faces of the ROI[3]. The vertices that lie in such faces usually have degree one.

8.4.2 Plant ER remodelling

The following sections demonstrate that the plant ER under normal physiological conditions constantly remodels itself in different ways, sometimes through the for-

[3]These are artificial and were created as a result of the cropping process.

mation of new tubules (Figure 8.8 on page 156), and sometimes through the closing of existing loops (Figure 8.9 on page 157). This can occur in very short time scales of less than 0.64 sec (i.e. less than one frame of the scanned timeseries). Remodelling in mammalian cells was reported in Lee & Chen (1988), the following sections demonstrate remodeling in the plant ER.

The generation of new tubules and junctions

The generation of a new tubule starts with the formation of a bend in the middle of a tubule (some sort of attraction force pulls it away from the edge, see Figure 8.8). This bend is usually accompanied by an increase in the intensity level in the direction of its convex side. A new tubule and a new junction are born when the "bubble" meets the tubule. This observation remains a speculation and has to be double checked by high resolution microscopy. If this is true then the bubble can be considered as the source of the attraction force that pulls away part of the branch to form a new one.

The closing and opening of loops

The closing of an existing loop (illustrated in Figure 8.9 on page 157), starts by gradual decrease in the length of its tubules and a gradual decrease in diameter of the circumcircle. The tubules gets shorter and shorter till they meet near the circumcenter of the original loop. Both phenomena occur in mammals and were reported in Lee & Chen (1988).

This chapter distinguishes between two sorts of movements in the ER: (1) shear (or bending) movement that is not related to the remodelling of the ER; this is the movement where the whole reticulum changes its position, while conserving its initial structure (the initial tubules and junctions

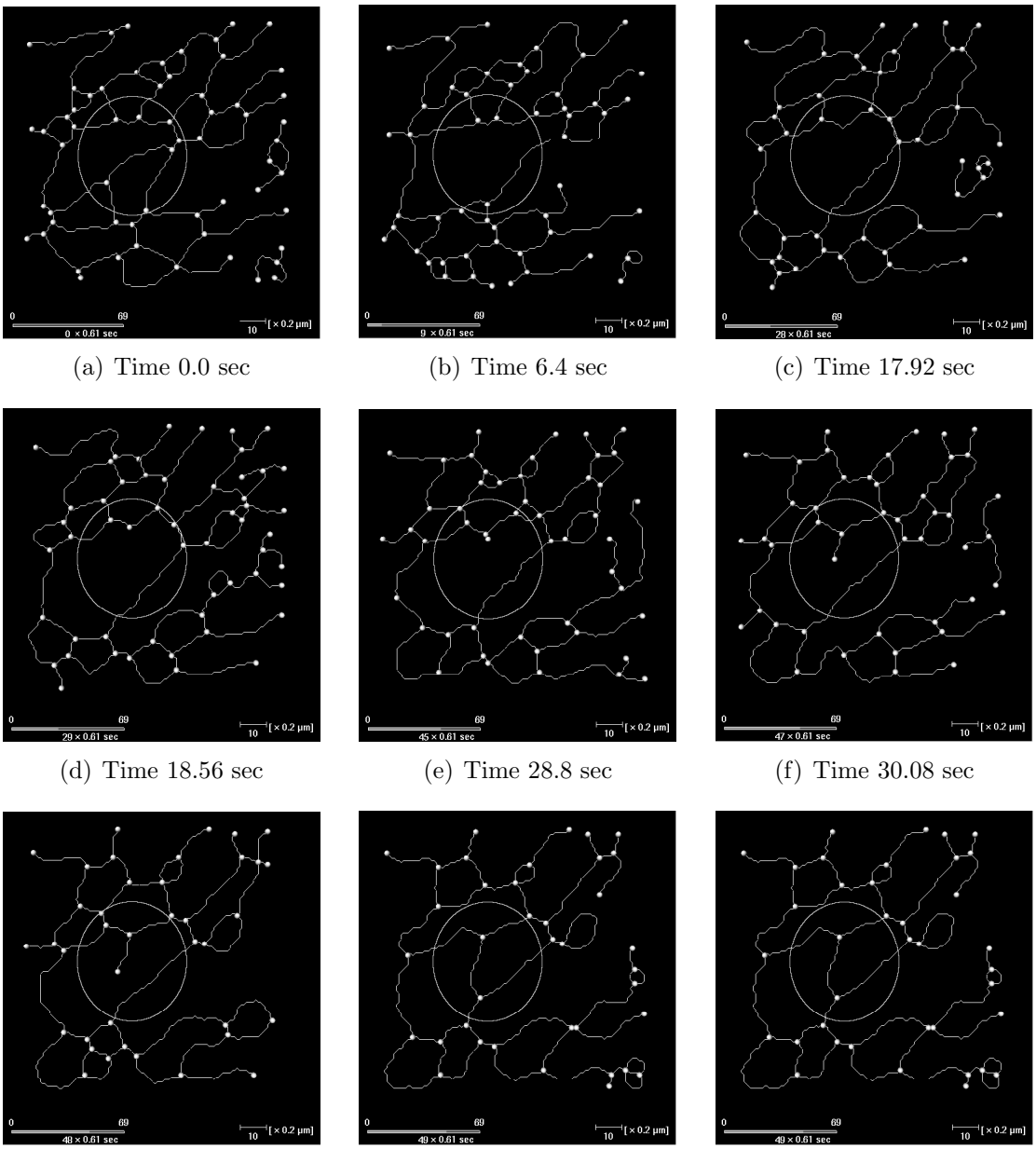

(a) Time 0.0 sec (b) Time 6.4 sec (c) Time 17.92 sec

(d) Time 18.56 sec (e) Time 28.8 sec (f) Time 30.08 sec

(g) Time 30.72 sec (h) Time 31.36 sec (i) Time 44.16 sec

Figure 8.8: An illustration of the plant ER loop closing, and the formation of new tubules (within the white circle): A tubule starts forming by the appearance of a bend in the middle of an edge (branch), which stretches towards the opposite edge to fuse with it forming a new edge and a new vertex(junction). (a), and (b) show the network before the appearance of the bend, (c) shows the start of the formation of a bend in the middle of the tubule, (d) and (e) show the stretching of the newly formed tubule towards the opposite edge (branch), (h), and (i) show the fusion of the extended end point with the opposite edge forming a stable loop. Scale bar (bottom right of each frame) $0.6\mu m$, and time bar (bottom left) $69.64sec$

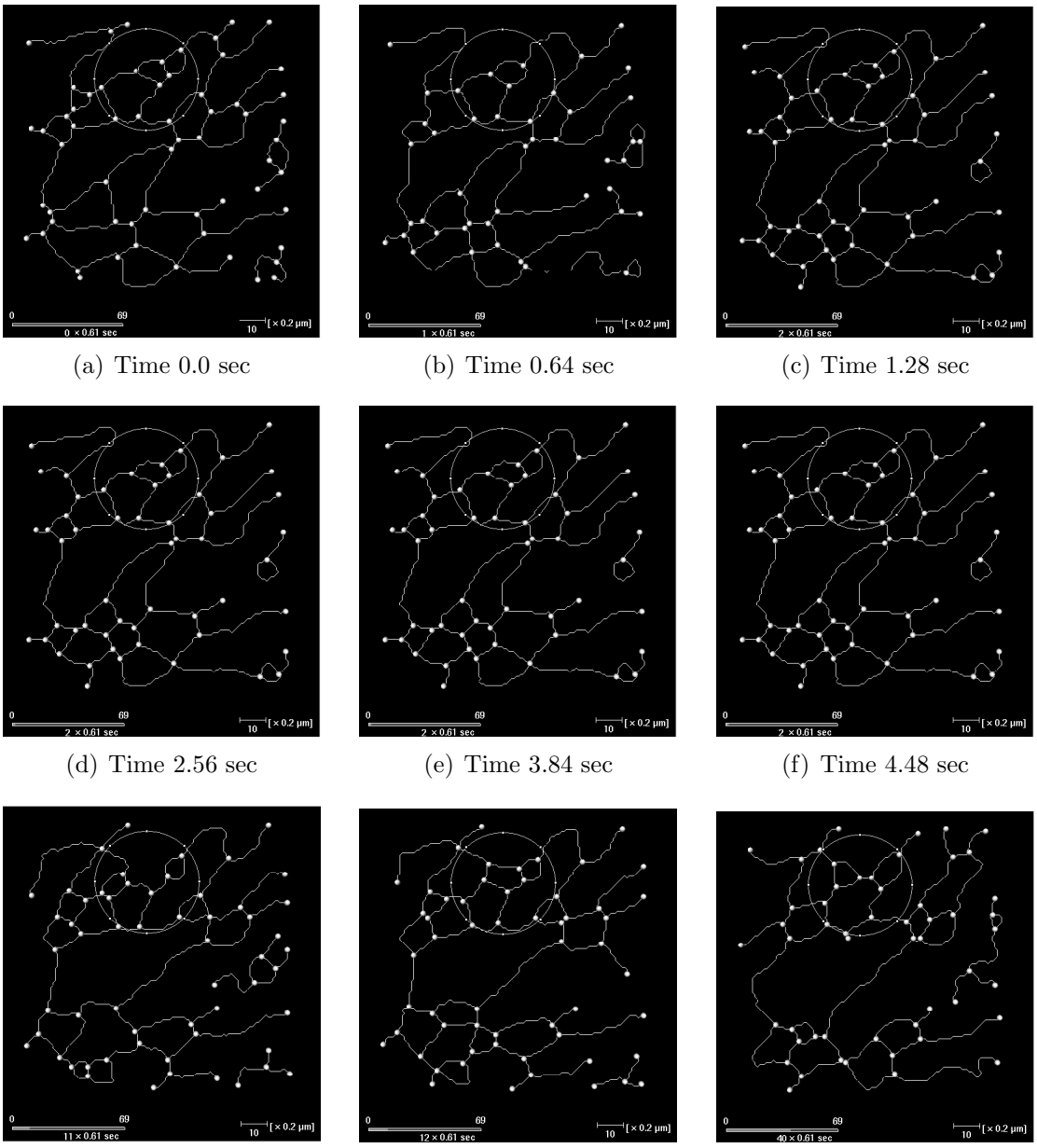

(a) Time 0.0 sec (b) Time 0.64 sec (c) Time 1.28 sec

(d) Time 2.56 sec (e) Time 3.84 sec (f) Time 4.48 sec

(g) Time 7.04 sec (h) Time 7.68 sec (i) Time 25.6 sec

Figure 8.9: An illustration of the ER loop opening (within the white circle) and the dynamic nature of the plant ER: (a) initially there were three loops within the circle of focus, (b) within a very short time (less than 0.64 sec) the upper loop closes, then (c) it opens again after 0.64 sec it stays stable for about 3.20 sec shown in Figures (c) to (f), and in Figure (g) the middle loop closes and in the subsequent Figures the new loop closes again (h). Figure (i) shows the network after 25.6 sec. Scale bar (bottom right of each frame) $0.6\mu m$, and time bar (bottom left) $69.64sec$

remain unaffected without any disconnection or disappearance), and (b) remodelling movement where the initial structure of the ER changes either by a change in the number of its tubules or a variation in the number of its junctions. Examples of this kind of movement include the stretching and retraction of tubules as well as the closing and opening of loops.

Throughout the remainder of this chapter we refer to movement of type 1 or movement of type 2 if we wish to distinguish between the bending type of movement or the remodelling type of movement respectively.

The following sections show time series of a set of the ER parameters as sequences of observations ordered in time. Some of these parameters are of type 1 while others are of type 2. The observations include: (a) the number of vertices, (b) the number of edges, (c) the average vertex degree, (d) the total length of the specimen, (e) the total surface area of the specimen, (f) the total volume of the specimen, (g) the specimen length density, (h) the specimen's area density, as well as (i) the volume-to-surface area ratio of the specimen.

We repeated the observations on 10 ROIs taken from 10 different ER samples, and we display the data in the order in which they occur using 3D line plots that include all observations. In each plot the parameter value is plotted on the vertical axis and time t on the horizontal axis. The observations are taken at regularly spaced intervals of $0.64sec$

8.4.3 Number of vertices vs time

The variations of the number of vertices with time is related to type 2 movement and can be interpreted as events related to functions of the network such as quality control and protein distribution. In Figure 8.10 on page 159, ROI 5 ($MIN = 99$

$MAX = 156$, and $MEAN = 128.3$) suggests a more active ER than ROI 1 ($MIN = 66$, $MAX = 99$, and $MEAN = 82.6$). The difference in activities in the two ER ROIs can also be inferred from the difference in the smoothness of their graphs (the former is smoother than the latter which indicates smaller local variations.)

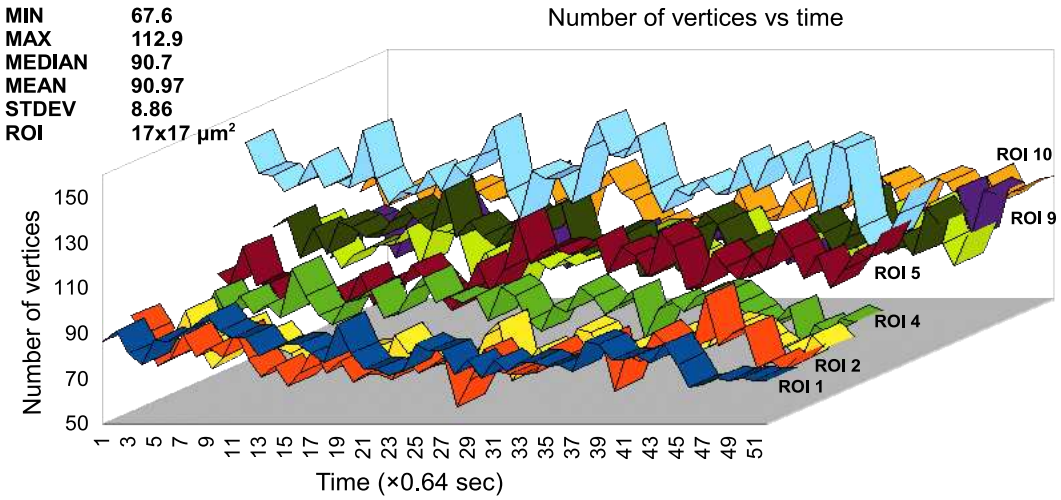

ROI	(1)	(2)	(3)	(4)	(5)	(6)	(7)	(8)	(9)	(10)
Min	66	52	58	56	78	99	76	69	70	52
Max	98	101	90	102	118	156	121	109	121	113
Med	80	74	72	82	96	127	99	89	90	98
μ	80.2	73.8	72. 8	81.3	95.7	128.3	99.03	89.3	91.0	98.3
σ	7.4	8.5	6.85	9.4	9.2	12.3	9.4	8.0	9.7	8.0

Figure 8.10: A graph showing the variation of the number of vertices with time. The measurements were performed on 10 different ROIs taken from 10 different samples. The graphs are colour coded, each one referring to a different ROI. The size of the ROI is $17 \times 17 \mu m^2$. There are 69 time steps each lasting for 0.64 sec.

8.4.4 Number of edges vs time

The variations of the number of edges with time is also related to the ER type 2 movement. The number of edges is related to the number of vertices, because each occurrence of a new tubules would be accompanied by the formation of two new vertices. The graphs in Figure 8.11 on page 160 show the variation of the number of edges with time in the 10 ROIs. Here again ROI 5 ($MIN = 131$ $MAX = 228$, and

$MEAN = 184$) suggests a more active ER than ROI 1 ($MIN = 66$, $MAX = 98$, and $MEAN = 80.0$). Again the difference in activities in the two ER ROIs can also be inferred from the difference in the smoothness of their graphs (the former is smoother than the latter which indicates smaller local variations). Figure 8.10 on

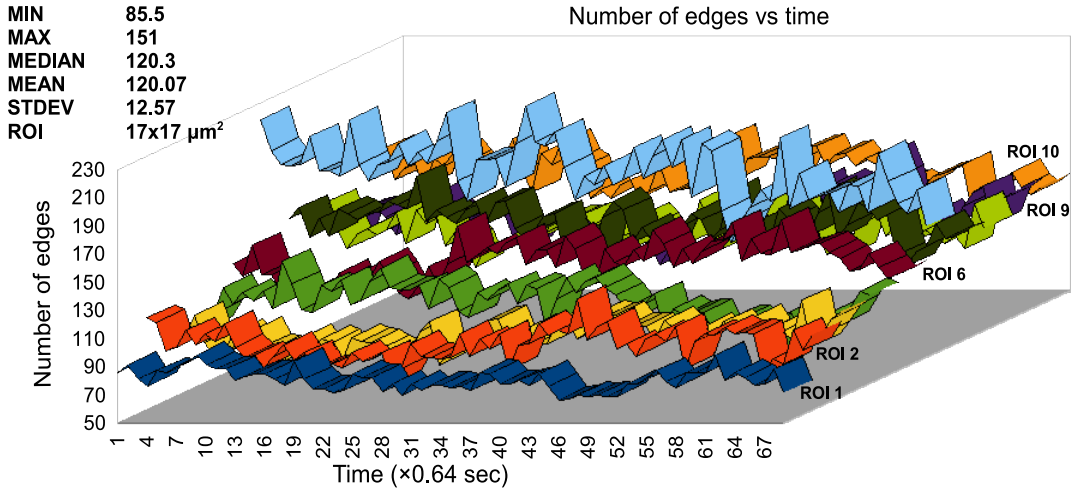

ROI	(1)	(2)	(3)	(4)	(5)	(6)	(7)	(8)	(9)	(10)
Min	66	67	72	69	100	131	104	94	86	66
Max	98	129	118	136	156	228	168	144	165	168
Med	80	96	92	106	126	184	137	119	118	145
μ	80.2	95.2	93.0	106.4	126.2	181.1	135.0	119.9	120.7	143.0
σ	7.4	11.5	9.61	13.6	13.6	20.3	12.5	10.8	14.6	11.8

Figure 8.11: A graph showing the variation of the number of edges with time. The measurement were performed on 10 different regions of interests taken from 10 different samples. The graphs are colour coded, each one refers to a different ROI. The size of the ROI is $17 \times 17 \mu m^2$. There are 69 time steps each lasting for 0.64 sec.

page 159 and Figure 8.11 on page 160 together demonstrate that the two parameters affect each other. This is because the creation of a new tubule always means the creation of a new vertex, and the closing of a loop means a decrease in the number of vertices.

8.4.5 Average vertex degree vs time

The variations of the average vertex degree with time is another example of ER type 2 movement. Figure 8.12 on page 161 shows graphs of the same ROIs as in

Figure 8.10 on page 159 and Figure 8.11 on page 160. In this case however, it is difficult to draw any conclusions with regards to the activity of the network. ROI 6 ($MIN = 2.49$, $MAX = 2.87$, and $MEAN = 2.68$) and ROI 1 ($MIN = 2.42$, $MAX = 2.74$, and $MEAN = 2.59$), which showed the extreme cases in the previous two sections, do not vary significantly from each other.

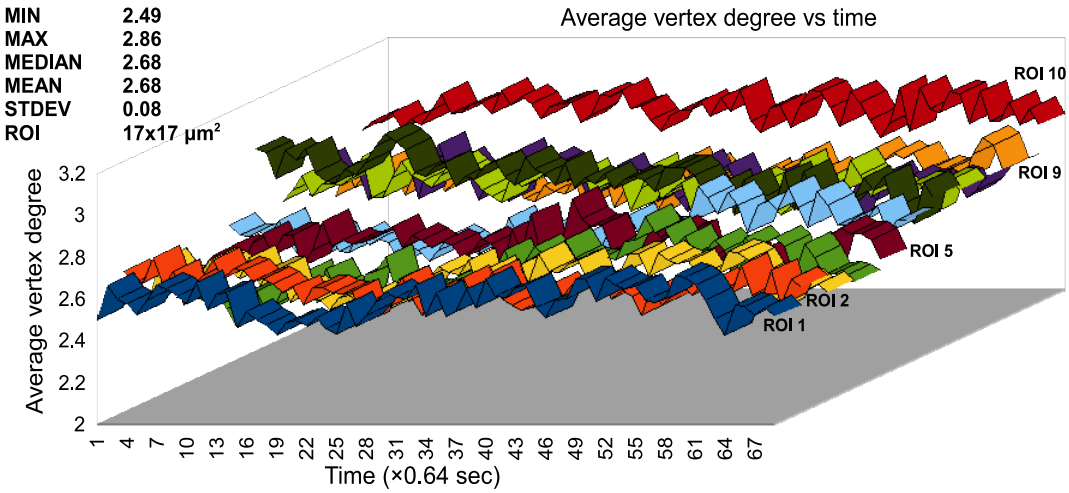

ROI	(1)	(2)	(3)	(4)	(5)	(6)	(7)	(8)	(9)	(10)
Min	2.42	2.42	2.29	2.37	2.47	2.6	2.59	2.49	2.46	2.78
Max	2.74	2.71	2.82	2.84	2.84	3.03	2.87	2.87	2.84	3.02
Med	2.59	2.59	2.54	2.62	2.62	2.83	2.74	2.69	2.65	2.91
μ	2.59	2.58	2.56	2.61	2.63	2.82	2.73	2.68	2.65	2.91
σ	0.06	0.08	0.11	0.08	0.09	0.09	0.07	0.08	0.08	0.06

Figure 8.12: A graph showing the variation of the average vertex degree with time. The measurement were performed on 10 different regions of interests taken from 10 different samples. The graphs are colour coded, each one refers to a different ROI. The size of the ROI is $17 \times 17 \mu m^2$. There are 69 time steps each lasting for 0.64 sec.

8.4.6 Total length vs time

The variations of the total length of the reticulum vs time is related to the ER type 2 movement. This parameter is illustrated in Figure 8.13 on page 162. A change in the total length may be due to the stretching and retraction of the tubules.

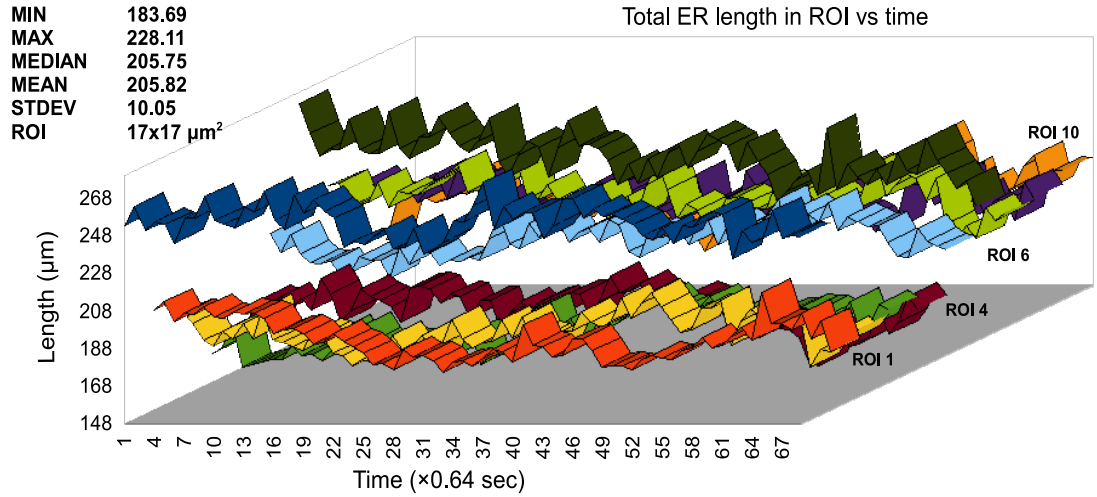

ROI	(1)	(2)	(3)	(4)	(5)	(6)	(7)	(8)	(9)	(10)
Min	235.3	168.0	163.4	155.9	149.6	188.7	219.0	192.9	190.7	173.3
Max	276.2	210.5	203.0	193.8	197.1	230.6	273.9	235.8	224.6	235.6
Med	253.8	182.4	181.5	176.5	179.5	209.2	247.1	217.0	208.7	201.7
μ	254.3	184.5	181.9	175.7	178.9	209.0	245.6	216.6	208.9	203.0
σ	8.6	10.4	9.3	11.0	9.9	9.7	11.8	9.2	8.2	12.3

Figure 8.13: A graph showing the variation of the total length of the ER in the ROI with time. The measurement were performed on 10 different regions of interests taken from 10 different samples. The graphs are colour coded, each one refers to a different ROI. The size of the ROI is $17 \times 17 \mu m^2$. There are 69 time steps each lasting for 0.64 sec.

8.4.7 Total surface area vs time

We calculate the total surface area of the ER within a ROI by adding the areas of all triangles in the corresponding triangulation, see Section 6.3 on page 97. The variations of the total surface area of the reticulum vs time is related to the ER type 2 movement. The variation of this parameter with time is illustrated in Figure 8.14 on page 163. A change in the total surface area of the ER may be due to the stretching and retraction of the tubules, or the dilation of the tubules.

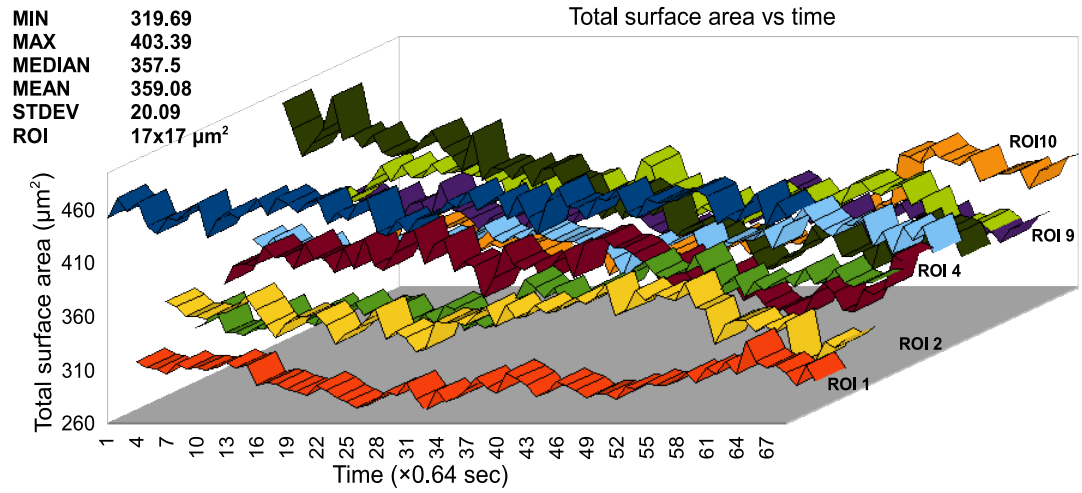

ROI	(1)	(2)	(3)	(4)	(5)	(6)	(7)	(8)	(9)	(10)
Min	434.2	258.5	283.0	304.1	306.1	333.6	326.5	343.3	326.8	280.8
Max	480.7	323.4	365.6	378.9	390.6	397.6	490.2	418.6	383.3	405.0
Med	458.2	283.2	333.9	336.9	355.8	366.4	387.7	382.1	349.5	321.4
μ	459.6	285.3	331.5	337.3	352.4	365.4	393.5	383.4	350.6	331.7
σ	11.6	12.9	16.9	19.7	20.5	11.9	43.7	17.5	12.8	33.2

Figure 8.14: A graph showing the variation of the total surface area of the ER with time. The measurement were performed on 10 different regions of interests taken from 10 different samples. The graphs are colour coded, each one refers to a different ROI. The size of the ROI is $17 \times 17 \mu m^2$. There are 69 time steps each lasting for 0.64 sec. (ROI: $17 \times 17 \mu m^2$).

8.4.8 Total volume vs time

We calculate the total volume of the ER within a ROI by counting the voxels in the foreground, see Section 6.4 on page 99. The variations of the total volume of the reticulum vs time is related to the ER type 2 movement. The variation of this parameter with time is illustrated in Figure 8.15 on page 164. A change in the total surface area of the ER may be also be due to the stretching and retraction of the tubules, or the dilation of the tubules.

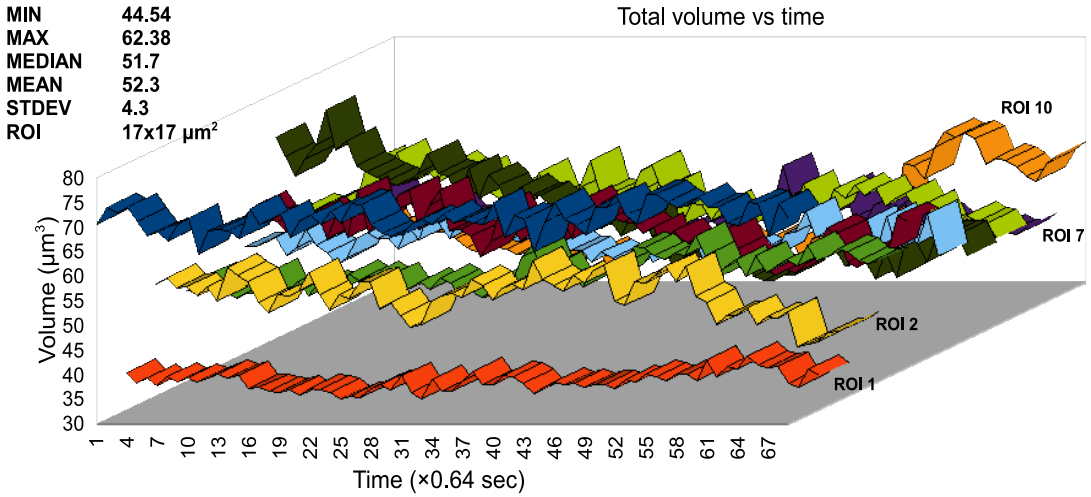

ROI	(1)	(2)	(3)	(4)	(5)	(6)	(7)	(8)	(9)	(10)
Min	64.5	32.0	39.9	46.7	48.6	46.3	41.7	47.5	42.8	35.4
Max	76.7	41.0	57.4	59.6	66.0	58.8	76.7	65.0	59.3	63.4
Med	71.3	35.5	50.5	51.4	57.6	52.4	52.4	55.5	48.9	41.6
μ	71.6	35.6	50.0	51.8	57.4	52.5	54.4	55.8	49.2	44.7
σ	2.7	1.9	4.1	3.3	4.3	2.7	9.0	4.1	3.0	8.0

Figure 8.15: A graph showing the variation of the total volume of the ER with time. The measurement were performed on 10 different regions of interests taken from 10 different samples. The graphs are colour coded, each one refers to a different ROI. The size of the ROI is $17 \times 17 \mu m^2$. There are 69 time steps each lasting for 0.64 sec. (ROI: $17 \times 17 \mu m^2$).

8.4.9 Volume-surface area ratio vs time

This chapter introduces the volume surface area ratio (Volume divided by the surface area) as a means of comparing the ER in different types of cells or under different physiological conditions. This is also linked to both types of the ER movements. An increase in this parameter may be due to the variation in either the volume or the surface area or both. Figure 8.16 on page 165 shows the variation of this parameter vs time.

8.4.10 Node displacement and average velocity vs time

The average velocity of a vertex is linked to type 2 movement of the ER. It is a vector quantity and so can give clues on the direction of movement of vertices. It is

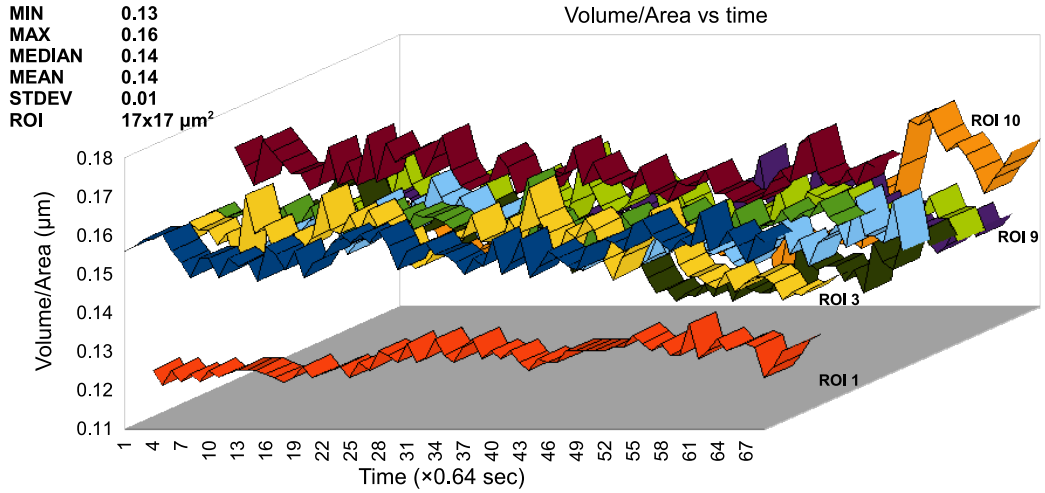

ROI	(1)	(2)	(3)	(4)	(5)	(6)	(7)	(8)	(9)	(10)
Min	0.15	0.12	0.14	0.15	0.16	0.14	0.12	0.14	0.13	0.12
Max	0.17	0.13	0.17	0.17	0.17	0.16	0.16	0.16	0.16	0.16
Med	0.16	0.13	0.15	0.15	0.16	0.14	0.14	0.15	0.14	0.13
μ	0.16	0.12	0.15	0.15	0.16	0.14	0.14	0.15	0.14	0.13
σ	0	0	0.01	0	0	0.01	0.01	0.01	0.01	0.01

Figure 8.16: A graph showing the variation of the total volume/surface-area of the ER with time. The measurement were performed on 10 different regions of interests taken from 10 different samples. The graphs are colour coded, each one refers to a different ROI. The size of the ROI is $17 \times 17 \mu m^2$. There are 69 time steps each lasting for 0.64 sec. (ROI: $17 \times 17 \mu m^2$).

defined as the rate of change of displacement, where displacement is the straight-line distance between the objects starting and finishing points.

Assuming vertex v was detected at position (x_t, y_t) in frame t and moved to position (x_{t+1}, y_{t+1}) in frame $t+1$. If the time between the two frames is δt, we calculate the

Table 8.1: Junction dynamic averages: Total displacement $D_{tot}(\mu m)$, maximum displacement D_{max} in a single frame, time of travel $t(sec)$, and velocity $\|\mathbf{V}\|(\mu m/sec)$

$n = 2346$	$D_{tot}(\mu m)$	$D_{max}(\mu m)$	$t(sec)$	$\|\mathbf{V}\|(\mu m/sec)$
MIN	1	0.38	0.64	0
MAX	12.96	1.5	37.76	1.7
Med	2.68	1.5	5.76	0.17
μ	3.68	1.48	8.98	0.25
σ	2.74	0.06	8.45	0.23

average velocity using the following expression:

$$\mathbf{V} = \frac{x_{t+1} - x_t}{\delta t}\mathbf{i} + \frac{y_{t+1} - y_t}{\delta t}\mathbf{j}$$

$\mathbf{i}$, $\mathbf{j}$ are the unit vectors in the x and y directions respectively. Negative values of the velocity of a vertex indicate a movement in the opposite direction to those having positive values. Table 8.1 on page 165 shows the dynamic averages of the movement of the ER, all of these parameters are linked to the type2 class of movement of the ER since they refer to single vertices. These parameters can be used to quantify the movements of the ER in different cell types (or under different physiological conditions).

8.5 Discussion

It is well known that the plant ER under normal physiological conditions performs a constant remodelling of its network structure. It is virtually impossible to apply our methods for such fast moving ER in full 3-D resolution. This is why we inhibited ER movement with the actin cytoskeleton-disrupting drug latrunculin B. Although effects of latrunculin treatment on ER morphology have been reported in other experimental systems (Radochová *et al.*, 2005; Zheng & Staehelin, 2001), in our experimental system (tobacco leaf epidermal cells), these effects can be considered negligible within the relative short time of treatment and confocal observation (Boevink *et al.*, 1998). For the analysis of moving ER, 2-D representation should be sufficient for the purpose of finding how the ER degree distribution changes over time because we imaged cortical ER which is relatively flat. An alternative to using 2D images only is to produce a 3D-stack with low resolution in the z direction and apply a maximum intensity projection into one plane. This has the advantage that connections of the ER away from the focal plane can be better recovered.

This chapter has shown that the plant ER, under normal physiological conditions, constantly remodels itself in different forms; the most noticeable of which are the formation of new tubules and the creation of new loops. It has also shown that, similar to the ER in mammals, the plant ER actively re-arranges itself in 4 types of movements:

1. *The elongation and retraction of tubules:* this is the simplest among the four types of movement and is related to the simple movement of the branches.
2. *The growth and shrinkage of tubules:*
3. *The branching of tubules:* is linked to the fusion of the membrane system with itself, where a tubule head merges with another part of the ER creating new connections.
4. *The displacement of the entire network:* this is where the entire network move without the creation or disappearance of tubules.

The average velocity of a junction is found to be in the range 0 to $1.7\mu m/sec$ which matches the reported actin filament range. The mean velocity is around $0.25\mu m/sec \pm 0.23$, this is due to the fact that the majority of the junctions are fixed 3-way junctions (attached to actin filaments).

The tubule branching, ring closure, and sliding cause the construction, disassembly, and rearrangement of the ER network. Ring closure performs the opposite function to tubule branching and fusion. I makes the ER less reticulated. It thus causes disassembly of the reticulum. Sliding causes simple rearrangements without affecting the overall area of the ER. Although we examined well-formed plant ER, where these movements generate new ER polygons on the basis of an existing network, it is possible that such movements could generate the reticulate structure by extending tubules outward from a nontubular body of membrane.

As in the case of mammals (see Lee & Chen (1988)), the motions of ER reported here share a common mechanism of motion of a point along a line. Tubule branching is occasionally marked by successive retreats and advances, the next advance again follows the original line of motion, suggesting that a linear underlying structure may be directing its motion (actin-myosin and associated motors which produce linear movements with velocities in the approximate range, see Yamada *et al.* (1990)).

If tubule branching is important in constructing the ER network by extending new tubules outwards along a cytoskeletal framework, then that framework would remain closely associated with the ER thus produced, possibly as an anchoring structure stabilising it. Actin filaments could participate in generating ER motions either by direct connection of the ER membrane to an actin filament sliding against another actin filament, predicting alignment of each ER tubule with two actin filaments in parallel, or by connection of the ER membrane to a motile protein moving along a stationary actin filament, predicting alignment with a single actin filament. Both models predict the existence of an anchoring protein (or proteins) on the ER membrane, binding to cytoskeletal filaments or associated motile proteins.

This chapter has showed the possibility of the creation of new loops at junctions or in the inner parts of a branch. Trajectories can be classified into either straight line paths or random motions. The former are usually associated with one degree vertices, which usually move forward and backwards before joining the opposite edge. The latter are usually associated with almost fixed junctions and have degree 3 or greater.

A sufficiently clear retrieval of ER geometry can currently only be obtained for cortical ER which is relatively flat, and slow. For the analysis of moving ER samples, 2D images are sufficient to find how the ER degree distribution changes over time. Using the Z-maximum projection and image enhancement(CLAHE), 2D images may even yield more accurate results than the corresponding 3D stacks, assuming that

the ER is cylindrical. This is because the axial confocal resolution is two to three times less than the lateral resolution (see Chapter 3). Furthermore, if the average diameter of an ER tubule is known (using electron microscopy for instance), then it is sufficient to measure its length to obtain the surface area and volume.

This chapter has introduced a new way of quantifying the ER data by (a) giving precise abstraction of the ER as long as it is 'network-like', using its skeleton and the corresponding geometric graph, where the nodes and vertices occupy the same positions in space, (b) allowing one to study the process of linking of the ER tubules and their dynamics (what we could call changing graph or network structure), (c) the well-defined positions, and controlled size of vertices allow the precise recordings and analysis of the ER movement, and finally (d) plotting time variation of the positions of the nodes provides a visual and quantitative summary of the dynamic of the ER. This means that we now have different well defined quantities, which characterise moving ER samples, which can be used to quantitatively compare the geometry and movement of the ER.

The results summarised in Table 8.2 on page 173 demonstrate the capability of the approach proposed in this chapter to quantify and characterise the geometry and dynamics of the ER using confocal images.

Another important aspect in this chapter is related to thresholding. As is the case for static samples, thresholding plays a crucial part in the accuracy of the calculations in dynamic samples. Due to the large number of images to be thresholded in each case an automatic, rather than manual, approach is vital; so in contrast to the global thresholding approach presented in the previous chapter, this chapter splits each image into smaller regions, and each pixel is automatically assigned a threshold value that depends on the mean and the variance of the grey level values in its neighbourhood. Therefore, thresholding in this chapter is fundamentally different from the one presented in Chapter 7. This chapter has introduced the concept of

dynamic graphs which evolve with time. The graph weights also vary with time and offer a way of comparing different samples under different conditions. It is important to realise that edge lengths and vertex degrees are less affected by confocal resolution and thresholding than edge surface areas and volumes, which is another motivation for using skeletons and graphs rather than the original 3D network. Furthermore, tracking graph vertices is much easier and more accurate than tracking the corresponding real junctions.

It must also be noted that the calculations in this chapter are subject to most of the errors mentioned in the previous chapter such as the errors introduced by using the confocal shot noise, the median filter and CLAHE, the errors due to triangulation, thinning, and those due to the mismatch of refractive indices between oil and water. Here the number of cycles and the degree distribution are important quantities which correspond to the connection structure of the graph, and therefore heavily influence how a protein or protein complex can pass from one location in the ER lumen or on its membrane to another. The remodeling of the ER may affect the efficiency of protein transport within its lumen or on its membrane. In general this is the underlying idea of a network structure, like a moving road system. The degree variation with time is linked to the question of how the ER membrane system can remodel itself with time, i.e. can make connections where part of the membrane system fuses with itself.

In this chapter we abstract the ER dynamics to a time dependent graph. The nodes (vertices) correspond to cisternae, and the tubules to the edges (links). We are able to quantify how many such structures exist in a certain ROI, how they are typically connected, and how this connection varies with time. This chapter gives the basics of comparative quantification in a new way. This can be exploited in future work.

Table 8.2: A summary of the dynamic ER analysis: each ROI was observed during 70 time steps, where each time step lasts for 0.64 sec, n_v, n_e, and v_{deg} refer to the number of vertices, the number of edges and the average vertex degree per time step respectively. In the last row, n refers to the number of trajectories analysed, D_{tot} to the total distance travelled by a node, D_{max} to the average maximum distance travelled by a node in one time step, and $\mathbf{V}$ to the average velocity.

Number of	vertices
Min	67.6
Max	112.9
Med	90.7
μ	90.1
σ	8.89

Number of	edges
Min	85.5
Max	151
Med	120.3
μ	120.1
σ	12.57

Vertex degree	
Min	2.49
Max	2.86
Med	2.68
μ	2.68
σ	0.08

Total length	μm
Min	183.7
Max	228.1
Med	205.8
μ	205.82
σ	10.1

Total area	μm^2
Min	319.7
Max	403.4
Med	357.5
μ	359.1
σ	20.1

Total volume	μm^3
Min	44.5
Max	62.4
Med	51.7
μ	52.3
σ	4.3

Volume/area	μm
Min	0.13
Max	0.16
Med	0.14
μ	0.14
σ	0.01

$n = 2346$	$D_{tot}(\mu m)$	$D_{max}(\mu m)$	$t(sec)$	$\|\mathbf{V}\|(\mu m/sec)$
Min	1	0.38	0.64	0
Max	12.96	1.5	37.76	1.7
Med	2.68	1.5	5.76	0.17
μ	3.68	1.48	8.98	0.25
σ	2.74	0.06	0.23	0.23

Part IV

Conclusion

9

Conclusion and Suggestions for Future work

While the confocal microscopes used in this study have a lateral resolution of as little as 200 nm and an axial discrimination of around 500 and 800 nm, electron microscopes have x/y resolution of 5 nm and z resolution between 120 and 160nm in the z plane. Despite this apparent superiority of the latter, this thesis adopts the former technique because of the following reasons: EM is more time consuming, it reveals much less ER network structure than confocal microscopy; the tubular network is almost invisible, all that can be seen are the sheets and more importantly it is not possible to capture the movement since the cell has to be killed.

The presented reconstruction step does heavily depend on thresholding where grey value information are prerequisite for reliable parameter measurements. More accurate measurements might be achieved by avoiding the use of thresholding altogether. A possible alternative to thresholding is the use of the point spread function of the confocal microscope. In this case the size and anisotropy of the PSF has to be taken into account to avoid bias and orientation dependence, see Streekstra & Pelt (2002).

The treatment of the ER with Latranculin (LatB) may lead to morphological alterations of the ER network. However, as far as the experience and the literature are concerned, the effect of LatB on cortical ER architecture is minimal within the time frame of observation in our case (maximum 20 minutes after a 30 minute incubation in 1 μM LatB). Since we are dealing with optical z-sectioning, it is altogether impossible to obtain consistent z stacks without stopping ER movement. Therefore the use of LatB or similar inhibitor can be seen as a 'necessary evil' for the type of analysis done here.

The use of oil immersion objective lenses with water-mounted samples for the observation of the secretory pathway is widespread in the plant community and is generally preferred to water-dipping objective. In the experiments explained, the water dipping and water immersion objectives available (63x, NA0.9) produce images of far inferior quality. Therefore our method can immediately be embraced by the plant live cell imaging community. Similar approaches were used to analyse 3-D images of the cerebral micro-vascular network which involves centre lines extraction and a vessel diameters estimation (see Fouard *et al.* (2006)).

To improve the accuracy and speed of solid ER measurement all calculations have been based on associating voxels and triangles to the skeleton edge points (section 2.4.3 length, surface area, and volume calculation). All that is needed in this approach is a skeleton, the relevant isosurface and its triangulation, which can be obtained using advanced visualisation software.

This thesis has demonstrated how a mathematical entity, such as a graph, can be used to quantify the geometry and the movement of the solid ER network. We are able to quantify how many such structures exist in a certain volume at a given time, and how they are typically connected. This approach does not discuss any function of the ER itself. This is legitimate, as future work on function will now be able to speak about exact changes of quantities, and how they will affect other measured data. One function of the ER is, for example, to distribute and sort proteins, both membrane and cytosolic. Following this approach, one could measure how efficiently proteins diffuse in the lumen or on the membrane of the ER.

In one interpretation the nodes (vertices) correspond to cisternae, and the tubules to the edges (links). The number of cycles and degree distribution correspond to the connection structure of the graph and influence how a protein can go from one location to another, and how close is any part of an ER membrane to a given organelle in the cytosol. A network structure can be regarded as a road system. The degree distribution itself is biologically connected to how the ER membrane system can remodel itself, i.e. can make connections where part of the membrane fuses.

An important aspect of quantifying the solid ER is related to the effective sorting and distribution of proteins by the ER membrane system. We do not like to limit our new way of quantification to just one of these functions, as there might be several ones that can be studied with the given methods. In this thesis we refrain from discussing any particular ER function but stress that any such discussion will be more appropriate if one can do so by using quantities and their changes to measure physiological effects.

It is interesting to note that, using differential interference contrast (DIC) microscopy, Upadhyaya & Sheetz (2004) reported a diameter of $\sim 115nm$ assuming a cylindrical network (for which is there is no basis).

An anisotropic diffusion filter would be more adaptive to the underlying image structure but neither anisotropic diffusion filter nor the maximum entropy filter exist

under Amira's current version. It is possible to use Matlab scripts within Amira for such filters. The problem we were facing at the time of writing this manuscript is that Amira can only have a Matlab interface in a 32 bit machine with a Microsoft operating system. Unfortunately none of these two requirements were possible (we use a 64 bit Linux machine!). Therefore we based our analysis on literature and Amira user manual recommendations. We used a median kernel size 3 to reduce loss of data while removing unattached points from the data. All the calculations are based on associating voxels and triangles to the skeleton edge points, which makes the calculations more accurate and rotationally invariant i.e. by rotating the input data one might get the same results. All that is needed in the proposed approach is a skeleton and the relevant isosurface and its triangulation. These can be obtained using Amira or any other software. The proposed algorithm associates each voxel and surface triangle to the nearest edge vertices by using their centre of gravity.

Thresholding techniques have attracted the interest of many authors and have been classified into many types, some of which are computationally demanding and others are less accurate. The approach we adopted in this investigation is accurate, simple to implement, and computationally cheap. Using integral and square images we can analyse 196 steps in less than one hour using a single core 1.7GHz laptop computer and the quantification of the entire series (more than 190 frames) can be obtained in less then 5 minutes. We therefore consider our approach fast enough. The iterative adaptive thresholding approach presented in Chapter 8 outperforms the manual global thresholding approach proposed in Chapter 7 and other global techniques such as the minimum error global thresholding technique, proposed by Kittler & Illingworth (1986), and the Otsu global thresholding technique. We suggest making the window size in Sauvola adaptive, i.e. variable with the point location. This, to our knowledge, has not been done before and can be very easily implemented. In fact we think that it should follow a Gaussian distribution of a known variance to take into consideration the contributions of other pixels.

It is important to note that the recorded 3-D volumes are lower than the theoretical values that can be expected from an optimal confocal microscopy setup, which is normal for live-imaging conditions. This unfavourable z-ratio produces structures that are mainly smeared out in direction of the optical axis. This implies that the volume and surface measurements are dominated by the axial components (this could be better seen from a side rotated view onto the network). By abstracting into a network possibly made up of spheres connected by cylinders, volume and surface estimates could also be obtained by 2-D measurements only. At least, the 2-D results could be compared with the corresponding 3-D estimates as a control.

Assuming cylindrical and spherical structures might even lead to more reliable estimates as long as the ER is reasonably flat. Furthermore, surface and volume measurements rely not only on optical properties of the specimen but also heavily on the homogeneity of the staining.

The next biological research target, regarding the ER, would be to employ the image

analysis tools described in this thesis to deal with the more fundamental problem of how the shape and organisation of the ER are generated and maintained and how they affect the functions of the ER. A possible important application of the approach proposed is to correlate the quantification presented to other quantities measuring other biological functions such as genetic activities.

The presented studies have created bridges between computational science, confocal microscopy and biological investigations. The methodology presented in this thesis can be applied to other dynamic complex network-like structures such as microfilaments, intermediate filaments, microtubules, chromosomes, blood vessels, intestinal tracks (colons), and dendrites of neuron cells, whose data were acquired by confocal microscopy.

Proposal: The diffusion of proteins in the lumen of the ER and on its membrane have already been studied, see Sbalzarini *et al.* (2006, 2005) for instance. The movement of the ER was introduced in this thesis. What is not known is how the movement of the ER affects its function, and how to relate the outside movement of the reticulum to the transport of proteins in the ER.

Part V

Appendix

A

A.1 C++ codes

These include the codes which calculates the length, local diameter, surface area and volume of branch in a network (see accompanying DVD).

A.2 Java codes

These include the code which performs vertex tracking using feature point tracking algorithm (See accompanying DVD).

A.3 Matlab files

Image pre-processing algorithms: the mean, median, and Gaussian filters as well as the contrast limited adaptive histogram equalisation algorithms (see accompanying DVD).

A.4 TcL scripts

Isosurfaces, triangulations, distance maps, as well as skeletons were obtained using built in Amira functions (see accompanying DVD).

A.5 Bash scripts

A scripts which manages the above programs (see accompanying DVD).

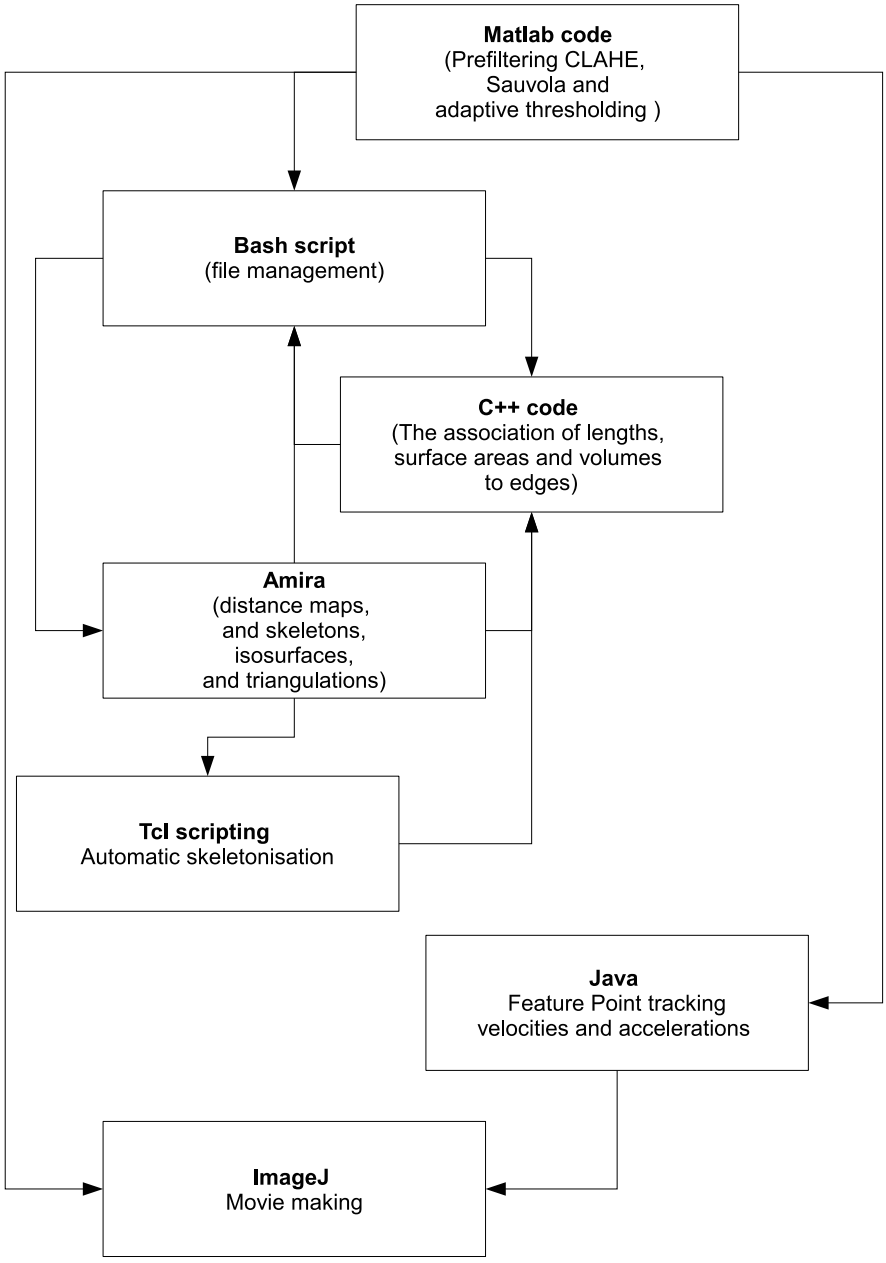

Figure A.1: A summary of the codes used in this thesis. See attached DVD for the source codes.

Bibliography

Anelli, T. & Sitia, R. (2007) Protein quality control in the early secretory pathway. *EMBO*. **27**, 315–327. 10, 16, 19

Attali, D. & Montanvert, A. (1997) Computing and simplifying 2D and 3D continuous skeletons. *Comput. Vis. Image Underst.*. **67**, 261–273. 64

Au, O. K.-C., Tai, C.-L., Chu, H.-K., Cohen-Or, D. & Lee, T.-Y. (2008) Skeleton Extraction by Mesh Contraction. *ACM Transactions on Graphics*. **27**, 44:2–44:10. 54, 66, 146

Balbás, A., Paulina nad Lorence (2004) *Gene expression review and protocols.* Humana Press. 21, 22, 23, 28

Batoko, H., Zheng, H.-Q., Hawes, C. & L., M. (2000) A Rab1 GTPase is required for transport between the endoplasmic reticulum and Golgi apparatus for normal Golgi movement in plants. *Plant Cell*. **12**, 2201–2217. 29, 109

Beenakker, C. W. J. (1999) Sub-Poissonian shot noise in nondegenerate diffusive conductors. *Phys. Rev. Lett.*. **82**, 2761–2763. 48

Bertrand, G. & Malandain, G. (1994) A new characterization of three-dimensional simple points. *Pattern Recog. Lett.*. **2**, 169175. 67, 81

BGL (2002) *The Boost Graph Library: user guide and reference manual.* Addison-Wesley Longman Publishing Co., Inc., Boston, MA, USA. 110

Blum, H. & Nagel, R. N. (1978) Shape description using weighted symmetric axis features. *Pattern Recognition*. **10**, 167 – 180. 66

Boevink, P., Martin, B., Oparka, K., Santa Cruz, S. & Hawes, C. (1999) Transport of virally expressed green fluorescent protein through the secretory pathway in tobacco leaves is inhibited by cold shock and brefeldin A. *Planta*. **208**, 392–400. 8, 20

Boevink, P., Oparka, K., Santa Cruz, S., Martin, B., Batteridge, A. & Hawes, C. (1998) Stacks on tracks: The plant Golgi apparatus traffics on an actin/ER network. *Plant Journal*. **15**, 441–447. 8, 20, 136, 166

Boevink, P., SantaCruz, S., Hawes, C., Harris, N. & Oparka, K. (1996) Virus-mediated delivery of the green fluorescent protein to the endoplasmic reticulum of plant cells. *Plant Journal*. **10**, 935–941. 8, 20

Borgefors, G. (1984) Distance transformation in arbitrary dimensions. *Computer Vision, Graphics, and Image Processing*. **27**, 321–145. 73, 77

Born, M. & Wolf, E. (1980) *Principles of Optics.* Pergamon Press, Oxford, UK. 41

Breu, H., Gil, J., Kirkpatrick, D. & Werman, M. (1995) Linear time euclidean distance transform algorithms. *IEEE Transactions on Pattern Analysis and Machine Intelligence*. **17**, 529–533. 75

Calabi, L. & Harnett, W. (1968) Shape recognition, prairie fires, convex deficiences and skeletons. *American mathematical monthly*. **75**, 335–342. 69, 115

Chen, I. & Dubnau, D. (2004) DNA uptake during bacterial transformation, *Nat Rev Micro*. **2**, 241–249. 28

Claxton, N. S., Fellers, T. J. & Davidson, M. W. (2008) Laser scanning confocal microscopy. Tech. rep.. National High Magnetic Field Laboratory. The Florida State University, Tallahassee, Florida 32310. 31, 32, 39, 40

Cooper, G. M. (2000) *The cell: a molecular approach.* Sinauer Associates, Inc.. 2nd ed. 16, 18

Cornea, N. D. & Min, P. (2007) Curve-skeleton properties, applications, and algorithms. *IEEE Transactions on Visualization and Computer Graphics*. **13**, 530–548 Member-Deborah Silver. 54, 57

Crocker, J. & Grier, D. G. (1996) Methods of digital video microscopy for colloidal studies. *Journal of Colloid and Interface Science*. **179**, 298–310. 84, 85, 86, 89, 93, 141, 142, 148, 149

Cuisenaire, O. (1999) *Distance transformations : fast algorithm and applications to medical image processing.* Ph.D. thesis. Université catholique de Louvain, Belgium. 74, 75, 81

Dalziel, S. (1993) Rayleigh-Taylor instability: experiments with image analysis. *Dynamics of Atmospheres and Oceans*. **20**, 127–153. 91, 151

Dalziel, S. B. (1992) Decay of rotating turbulence: some particle tracking experiments. *Applied Scientific Research*. **49**, 217–244. 91, 151

Danielsson, P.-E. (1980) Euclidean distance mapping. *Computer Graphics and Image Processing*. **14**, 227–248. 74

daSilva, L. L., Snapp, E. L., Denecke, J., Lippincott-Schwartz, J., Hawes, C. & Brandizzi, F. (2004) Endoplasmic reticulum export sites and Golgi bodies behave as single mobile secretory units in plant cells. *Plant Cell*. **16**, 1753–1771. 18

Denecke, J. (2007) The Endoplasmic Reticulum in Plants. In *Michalak, M. (ed.), The Endoplasmic Reticulum: Fundamentals and Role in Disease. The Biomedical & Life Sciences Collection*. Henry Stewart Talks Ltd. 16, 17, 18, 19

Dreier, L. & Rapoport, T. (2000) *in vitro* formation of the endoplasmic reticulum occurs independently of microtubules by a controlled fusion reaction. *Journal of Cell Biology*. **148**, 883–898. 20

Eggers, H. (1996) Parallel euclidean distance transformations in z^n. *Pattern Recognition Letters,*. **17**, 751–757. 75

Fawcett, D. W. (1981) *The cell.* Philadelphia. 2nd ed. 12, 18

Fol-Leymarie, F. F. (2003) *Three-dimensional shape representation via shock flows.* Ph.D. thesis. Providence, RI, USA Adviser-Kimia, Benjamin B. 54

Forero, M. G., Pennack, J., Learte, A. R. & Hidalgo, A. (2006) Correction of depth intensity attenuation in confocal images of Drosophila embryos. In *Information OpticsDNA-Based Nanoscale Integration*, edited by G. Cristóbal, B. Javidi & S. Vallmitjana. vol. 860 of *American Institute of Physics Conference Series*. 397–400. 59

Fouard, C. (2005) *Extraction de paramètres morphométriques pour l'étude du réseau micro-vasculaire cérébrals.* Ph.D. thesis. L' Université de Nice Sophia Antipolis. 65, 80, 114, 115

Fouard, C., Malandain, G., Prohaska, S. & Westerhoff, M. (2006) Blockwise processing applied to brain micro-vascular network study. *IEEE Transaction on Medical Imaging*. **25**, 1319–1328 Accepted for publication. 33, 71, 81, 111, 137, 176

Gomes, J. & Faugeras, O. D. (2000) Level sets and distance functions. *Proc. of the Europ. Conf. on Computer Vision*. **1842 of LNCS**, 588–602. 64, 65, 66

Gong, W. & Bertrand, G. (1990) A simple parallel 3D thinning algorithm. *International Conference on Pattern Recognition*. 188–190. 69

Gonzalez, R. C. & Woods, R. E. (2002) *Digital image processing.* Prentice Hall. 2nd ed. 112

Gonzalez, R. C. & Woods, R. E. (2008) *Digital image processing.* Prentice Hall. 3rd ed. 56, 58, 60, 88

Grafen, A. & Hails, R. (2002) *Modern statistics for the life sciences.* Oxford University Press. 123

Hansen, G. & Wright, M. S. (1999) Recent advances in the transformation of plants. *Trends in Plant Science*. **4**, 226 – 231. 21

Hanton, S. L., Bortolotti, L. E., Renna, L., Stefano, G. & Brandizzi, F. (2005) Crossing the divide–transport between the endoplasmic reticulum and Golgi apparatus in plants. *Traffic*. **6**, 267–277. 16, 18, 19

Hawes, C. & Satiat-Jeunemaitre, B. (2005) The plant Golgi apparatus–going with the flow. *Biochim Biophys Acta*. **744**, 466–480. 16, 18, 19

He, T., Hong, L., Chen, D. & Liang, Z. (2001) Reliable path for virtual endoscopy: ensuring complete examination of human organs. *IEEE Transactions on Visualization and Computer Graphics*. **7**, 333–342. 54

Hitchcock, F. L. (1941) The distribution of a product from several sources to numerous localities. *J. Math. Phys.*. **20**, 224. 91, 151

Ho, R. & Shao, Z. (1991) Axial resolution of confocal microscopes revisited. *OPTIK*. **88**, 147–154. 41, 44

Huang, C. T. & Mitchell, O. R. (1994) A Euclidean distance transform using grayscale morphology decomposition. *IEEE Trans. Pattern Anal. Mach. Intell.*. **16**, 443–448. 75

Irons, S., Evans, D. & Brandizzi, F. (2003) The first 238 amino acids of the human lamin B receptor are targeted to the nuclear envelope in plants. *Journal of Experimental Botany*. **54**, 943–950. 8, 20

Jonker, P. P. (2000) Morphological operations on 3D and 4D images: from shape primitive detection to skeletonization. 69

Kittler, J. & Illingworth, J. (1986) Minimum error thresholding. *Pattern Recogn.*. **19**, 41–47. 144, 177

Kong, T. Y. & Rosenfeld, A. (1989) Digital topology: Introduction and survey. *Computer Vision, Graphics, and Image Processing*. **48**, 357–393. 55, 81

Kurup, S., Runions, J., Kohler, U., Laplaze, L., Hodge, S. & Haseloff, J. (2005) Marking cell lineages in living tissues. *Plant Journal*. **42**, 444–453. 8, 20

Langhans, M., Niemes, S., Pimpl, P. . & Robinson, D. G. (2009) Oryzalin bodies: in addition to its anti-microtubule properties, the dinitroaniline herbicide oryzalin causes nodulation of the endoplasmic reticulum. *Protoplasma*. **In process**, 1615–6102. 21

Lee, C. & Chen, L. B. (1988) Dynamic behavior of endoplasmic reticulum in living cells. *Cell*. **54**, 37 – 46. 136, 155, 168

Leica, M. (2000) *True confocal scanner leica tcs sp II user manual.* Leica Microsystems CMS GmbH. RK09052000 ed. 30, 32, 36, 37, 38, 48, 52

Leica, M. (2005) *Leica TCS SP5 User Manual.* Leica Microsystems CMS GmbH. 30, 33, 48

Li, X., Woon, T. W., Tan, T. S. & Huang, Z. (2001) Decomposing polygon meshes for interactive applications. In *I3D '01: Proceedings of the 2001 symposium on Interactive 3D graphics*. 35–42. ACM, New York, NY, USA. 54

Lichtscheidl, I. K. & Hepler, P. K. (1996) *Membranes : specialized functions in plants / M. Smallwood, J.P. Knox, D.J. Bowles.* . chap. Endoplasmic reticulum in the cortex of plant cells., 383–403 Oxford, UK : Bios Scientific Publishers. 20, 108

Lodish, H., Berk, A., Kaiser, C. A., Krieger, M., Scott, M. P., Bretscher, A., Ploegh, H. & Matsudaira, P. T. (2004) *Molecular cell biology.* W.H. Freeman and Company, New York. 5th ed. 22

Lohou, C. & Bertrand, G. (2004) A 3D 12-subiteration thinning algorithm based on P-simple points. *Discrete Appl. Math.*. **139**, 171–195. 68, 69

Lohou, C. & Bertrand, G. (2005) A 3D 6-subiteration curve thinning algorithm based on P-simple points. *Discrete Appl. Math.*. **151**, 198–228. 68

Ma, C.-M. & Wan, S.-Y. (2000) Parallel thinning algorithms on 3D (18,6) binary images. *Comput. Vis. Image Underst.*. **80**, 364–378. 68

Malandain, G., Betrand, G. & Ayache, N. (1993) Topological segmentation of discrete surfaces. *Int. J. Comput. Vision*. **10**, 183–197. 81

Malandain, G. & Fernández-Vidal, S. (1998) Euclidean skeletons. *Image and Vision Computing*. **16**, 317 – 327. 69, 115

Marty, F. (1999) Plant Vacuoles. *Plant Cell*. **11**, 587–600. 28

Minsky, M. (1988) Memoir on inventing the confocal scanning microscope. *Scanning*. **10**, 128–138. 31, 32

Montanari, U. (1968) A method for obtaining skeletons using a quasi-euclidean distance. *J. ACM*. **15**, 600–624. 76

Nebenfuhr, A., Gallagher, L. A., Dunahay, T. G., Frohlick, J. A., Mazurkiewicz, A. M., Meehl, J. B. & Staehelin, L. A. (1999) Stop-and-go movements of plant Golgi stacks are mediated by the acto-myosin system. *Plant Physiol.*. **121**, 1127–1141. 136

Niblack, C. W., Gibbons, P. B. & Capson, D. W. (1992) Generating skeletons and centerlines from the distance transform. *CVGIP: Graph. Models Image Process.*. **54**, 420–437. 69, 72

Nicchitta, C. (2007) Endoplasmic reticulum, protein synthesis and translocation machinery. In *Michalak, M. (ed.), The Endoplasmic Reticulum: Fundamentals and Role in Disease. The Biomedical & Life Sciences Collection*. Henry Stewart Talks Ltd. 15

Nyquist, H. (2002) Certain topics in telegraph transmission theory. *Proceedings of the IEEE*. **90**, 280–305. 46

Oertle, T., Klinger, M., Stuermer, C. A. O. & Schwab, M. E. (2003) A reticular rhapsody: Phylogenic evolution and nomenclature of the RTN/Nogo gene family. *FASEB J.*. **17**, 1238–1247. 14

Paddock, S. (2001) Confocal laser scanning light microscopy. *Encyclopedia of Life Sciences*. 32

Palade, G. E. & Porter, K. R. (1954) Studies on the endoplasmic reticulum: i. its identification in cells in situ. *J. Exp. Med.*. **100**, 641–656. 8

Palágyi, K. & Kuba, A. (1999) Directional 3D thinning using 8 subiterations. 325–336. 68, 69

Palágyi, K., Sorantin, E., Balogh, E., Kuba, A., Halmai, C., Erdohelyi, B. & Hausegger, K. (2001) A sequential 3d thinning algorithm and its medical applications. 409–415. 68

Pawley, J. B. (1995) *Handbook of biological confocal microscopy.* Springer. 37, 38, 49

Pierson, E. S., Lichtscheidl, I. K. & Derksen, J. (1990) Structure and behaviour of organelles in living pollen tubes of lilium longiflorum. *J. Exp. Bot.*. **41**, 1461–1468. 51

Piller, H. (1977) *Microscope photometry.* SpringerVerlag, Berlin. 41

Porter, K. R., Claude, A. & Fullam, E. F. (1945) A study of tissue culture cells by electron microscopy: methods and preliminary observations. *J. Exp. Med.*. **81**, 233–246. 8

Prasad, V., Semwogerere, D. & Weeks, E. R. (2007) Confocal microscopy of colloids. *Journal of Physics: Condensed Matter*. **19**, 113102 (25pp). 32

Pudney, C. (1998) Distance-ordered homotopic thinning: a skeletonization algorithm for 3D digital images. *Comput. Vis. Image Underst.*. **72**, 404–413. 55, 57, 67, 68, 71, 72, 73, 77

Puhka, M., Vihinen, H., Joensuu, M. & Jokitalo, E. (2007) Endoplasmic reticulum remains continuous and undergoes sheet-to-tubule transformation during cell division in mammalian cells *J. Cell Biol.*. **179**, 895–909. 12

Radochová, B., Janáček, J., Schwarzerová, K., Demjénová, E., Tomori, Z., Karen, P. & Kubínová, L. (2005) Analysis of endoplasmic reticulum of tobacco cells using confocal microscopy *Image Anal Stereol*. **24**, 181–185. 166

Ragnemalm, I. (1993) The Euclidean distance transform in arbitrary dimensions. *Pattern Recogn. Lett.*. **14**, 883–888. 74

Reisen, D., Marty, F. & Leborgne-Castel, N. (2005) New insights into the tonoplast architecture of plant vacuoles and vacuolar dynamics during osmotic stress. *BMC Plant Biology*. **5**, 13. 28

Remy, E. & Thiel, E. (2000) Optimizing 3D chamfer masks with norm constraints. 39–56. 76

Reza, A. M. (2004) Realization of the contrast limited adaptive histogram equalization (clahe) for real-time image enhancement. *J. VLSI Signal Process. Syst.*. **38**, 35–44. 143

Rosenfeld, A. (1975) A characterization of parallel thinning algorithms. *Inform. Contr.*. **29**, 286–291. 69, 81

Rosenfeld, A. & Pfaltz, J. L. (1966) Sequential operations in digital picture processing. *J. ACM*. **13**, 471–494. 76, 79, 81

Runions, J., Brach, T., Kuhner, S. & Hawes, C. (2006) Photoactivation of GFP reveals protein dynamics within the endoplasmic reticulum membrane. *J. Exp. Bot.*. **57**, 43–50. 8, 20

Saito, T. & Toriwaki, J.-I. (1994) New algorithms for euclidean distance transformation of an n-dimensional digitized picture with applications. *Pattern Recognition*. **27**, 1551–1565. 71, 75

Saito, T. & Toriwaki, J. I. (1995) A sequential thinning algorithm for three dimensional digital pictures using the Euclidean distance transformation. *Proceedings, 9th Scandinavian Conference on Image Analysis (SCIA95)*. 71

Sbalzarini, I. F., Hayer, A., Helenius, A. & Koumoutsakos, P. (2006) Simulations of (an)isotropic diffusion on curved biological surfaces. *Biophys. J.*. **90**, 878–885. 178

Sbalzarini, I. F. & Koumoutsakos, P. (2005) Feature point tracking and trajectory analysis for video imaging in cell biology. *Journal of Structural Biology*. **151**, 182–195. 83, 84, 85, 86, 89, 91, 93, 140, 141, 142, 148, 149, 151

Sbalzarini, I. F., Mezzacasa, A., Helenius, A. & Koumoutsakos, P. (2005) Effects of organelle shape on fluorescence recovery after photobleaching. *Biophys. J.*. **89**, 1482–1492. 178

Schröder, M. & Kaufman, R. J. (2005a) ER stress and the unfolded protein response. *Mutation Research/Fundamental and Molecular Mechanisms of Mutagenesis*. **569**, 29 – 63 Stress Responses. 23

Schröder, M. & Kaufman, R. J. (2005b) The mammalian unfolded protein response. *Annual Review of Biochemistry*. **74**, 739–789. 15, 23

Selman, G. G. & Jurand, A. (1964) An electron microscope study of the Endoplasmic reticulum in newt notochord cells after disturbance with ultrasonic treatment and subsequent regeneration. *Cell Biology*. **20**, 175183. 11

Semwogerere, D. & Weeks, E. R. (2005) Confocal microscopy. Tech. rep.. Emory University, Atlanta, Georgia, U.S.A. 32, 33, 36, 133

Sezgin, M. & Sankur, B. (2004) Survey over image thresholding techniques and quantitative performance evaluation. *Journal of Electronic Imaging*. **13**, 146–168. 144

Shafait, F., Keysers, D. & Breuel, T. M. (2008) Efficient implementation of local adaptive thresholding techniques using integral images. In *Society of Photo-Optical Instrumentation Engineers (SPIE) Conference Series*. vol. 6815 of *Society of Photo-Optical Instrumentation Engineers (SPIE) Conference Series*. 63, 143

Sheppard, C. & Török, P. (1997) Effects of specimen refractive index on confocal imaging. *J. Microsc.* **185**, 366–74. 133

Shibata, Y., Voeltz, G. & Rapoport, T. (2006) Rough sheets and smooth tubules. *Cell*. **126**, 435–439. 11, 20

Shih, F.-C. & Mitchell, O. (1992) A mathematical morphology approach to euclidean distance transformation. *IEEE Transactions on Image Processing*. **1**, 197–204. 75

Sitia, R. (2007) The Endoplasmic reticulum as a most efficient antibody factory. In *Michalak, M. (ed.), The Endoplasmic Reticulum: Fundamentals and Role in Disease. The Biomedical & Life Sciences Collection*. Henry Stewart Talks Ltd. 15

Sparkes, I., Runions, J., Kearns, A. & Hawes, C. (2006) Rapid, transient expression of fluorescent fusion proteins in tobacco plants and generation of stably transformed plants. *Nat. Protocols*. **1**, 2019–2189. 21

Staehelin, L. A. (1997) The plant ER: a dynamic organelle composed of a large number of discrete functional domains. *The Plant Journal*. **11**, 1151–1165. 10, 12, 15, 20, 28, 108

Staehelin, L. A. & Kang, B.-H. (2008) Nanoscale architecture of Endoplasmic reticulum export sites and of Golgi membranes as determined by electron tomography. *Plant Physiol.*. **147**, 1454–1468. 7, 13

Stelzer, E. H. (2001) Confocal microscopy. *Encyclopedia of Life Sciences*. 34

Stephenson, J. L. M. & Hawes, C. R. (2005) Stereology and stereometry of endoplasmic reticulum during differentiation in the maize root cap. *Protoplasma*. **131**, 32–46. 21

Streekstra, G. & Pelt, v. (2002) Analysis of tubular structures in three-dimensional confocal images. *Network*. **13**, 381–95. 175

Sundar, H., Silver, D., Gagvani, N. & Dickinson, S. (2003) Skeleton based shape matching and retrieval. In *SMI '03: Proceedings of the Shape Modeling International 2003*. 290. IEEE Computer Society, Washington, DC, USA. 54

Taylor, N. J. & Fauquet, C. M. (2002) Microparticle bombardment as a tool in plant science and agricultural biotechnology. *DNA and Cell Biology*. **21**, 963–977. 21

Tsao, Y. & Fu, K. (1981) A parallel thinning algorithm for 3-D pictures. *Computer Graphics and Image Processing*. **17**, 315 – 331. 69

Tsien, R. Y. (1998) The green fluorescent protein. *Annual Review of Biochemistry*. **67**, 509–544. 8

Upadhyaya, A. & Sheetz, M. (2004) Tension in Tubulovesicular Networks of Golgi and Endoplasmic Reticulum Membranes. *Biophysical Journal*. **86**, 2923–2928. 176

Veratti, E. (1902) Richerche sulle fine struttura della fibra muscolara striata. *Memoire Inst. Cl. Sci. Mat.*. **19**, 87–133. 8

Verkhratsky, A. (2007) Physiology and pathophysiology of the calcium store in the endoplasmic reticulum of neurones. In *Michalak, M. (ed.), The Endoplasmic Reticulum: Fundamentals and Role in Disease*. The Biomedical & Life Sciences Collection, Henry Stewart Talks Ltd. 13

Verwer, B. (1991) *Distance transforms : metrics, algorithms and applications.* Ph.D. thesis. Technische Universiteit. 81

Vincent, L. (1991) Efficient computation of various types of skeletons. In *SPIE*, edited by SPIE. vol. 1445. 297–311. 71

Vitale, A., Ceriotti, A. & Denecke, J. (1993) The role of the Endoplasmic Reticulum in protein synthesis, modification and intracellular transport *J. Exp. Bot.*. **44**, 1417–1444. 108

Vitale, A. & Denecke, J. (1999) The endoplasmic reticulum gateway of the secretory pathway. *Plant Cell*. **11**, 615–628. 15, 18, 108

Voeltz, G. & Prinz, W. (2007) Sheets, ribbons and tubules - how organelles get their shape. *Nat Rev Mol Cell Bio*. **8**, 258–64. 8, 14, 15, 23, 152

Voeltz, G., Rolls, M. & Rapoport, T. (2002) Structural organization of the endoplasmic reticulum. *EMBO Rep.*. **3**, 944–50. 9, 10, 12, 14, 15, 23, 45

Voeltz, G. K., Prinz, W. A., Shibata, Y., Rist, J. M. & Rapoport, T. A. (2006) A class of membrane proteins shaping the tubular endoplasmic reticulum. *Cell*. **124**, 573 – 586. 13, 14, 30, 51

Wilhelm, S., Gröbler, B., Gluch, M. & Heinz, H. (2003) *Confocal laser scanning microscopy.* Carl Zeiss Jena GmbH. 45-0029 ed. 31, 35, 38, 40, 41, 44, 48, 51, 59

Wiseman, R. L., Powers, E. T., Buxbaum, J. N., Kelly, J. W. & Balch, W. E. (200) An adaptable standard for protein export from the endoplasmic reticulum. *Cell*. **131**, 809 –821. 19

Wu, F.-C., Ma, W.-C., Liang, R.-H., Chen, B.-Y. & Ouhyoung, M. (2006) Domain connected graph: the skeleton of a closed 3D shape for animation. *Vis. Comput.*. **22**, 117–135. 54

Yamada, A., Ishii, N. & Takahashi, K. (1990) Direction and speed of actin filaments moving along thick filaments isolated from molluscan smooth muscle. *J Biochem*. **108**, 341–343. 168

Yamada, H. (1984) Complete euclidean distance transformation by parallel operation. *Proc. Seventh Int'l Conf. Pattern Recognition*. **1**, 69–71. 74

Yilmaz, A., Javed, O. & Shah, M. (2006) Object tracking: a survey *ACM Comput. Surv.*. **38**, 13. 85

Young, I. (1996) Quantitative microscopy. *Engineering in Medicine and Biology Magazine, IEEE*. **15**, 59–66. 41, 48

Zheng, H. Q. & Staehelin, L. A. (2001) Nodal endoplasmic reticulum, a specialized form of endoplasmic reticulum found in gravity-sensing root tip columella cells. *Plant Physiol.*. **125**, 252–265. 166

Zhou, Y., Kaufman, A. & Toga, A. W. (1998) 3D skeleton and centerline generation based on an approximate minimum distance field. *International Journal of Visual Computer*. **14**, 303–314. 69, 115

Zuse, I. (2006) *Amira Reference's Guide 4.1* Konrad-Zuse-Zentrum fur Informationstechnik. Berlin, Germany. 31, 59, 111, 140

Index